Sediment Suspension in Surf Zones on Eroding and Equilibrium Beaches

by

Michael A. Giovannozzi

and

Nobuhisa Kobayashi

RESEARCH REPORT NO. CACR-01-05

October, 2001

Center for Applied Coastal Research
Ocean Engineering Laboratory
University of Delaware
Newark, DE 19716

ACKNOWLEDGMENTS

This work was supported by the National Science Foundation under Grant OCE-9901471 and by the National Oceanic and Atmospheric Administration Office of Sea Grant, Department of Commerce, under Grant No. NA85AA-D-SG033 (Project SG R/OE -29). Bradley D. Johnson and Yuki Tega are thanked for their contributions to the experiments conducted in this study.

TABLE OF CONTENTS

LIST OF FIGURES

LIST OF TABLES

ABSTRACT

A laboratory experiment was conducted in a wave flume to observe and measure sand suspension events under shoaling waves on a rippled bed and under breaking waves and bores on an equilibrium terraced beach consisting of fine sand. The same irregular waves were generated for 37 tests to measure the three-dimensional velocities and concentrations at several elevations above the local bed at five cross-shore locations. The measured alongshore velocity is shown to about 20% of the cross-shore velocity and an effective proxy for detecting three-dimensional vortices and turbulence near the rippled bed and inside the surf zone. The spectra of the alongshore velocities inside the surf zone were dominated by low frequency components associated with intermittent irregular wave breaking. The measured sand concentrations were dominated by intermittent suspension events accompanied by large fluctuating alongshore velocities. Large shoaling waves with large onshore velocities caused intermittently high sand concentrations above the rippled bed. Intermittent suspension events also occurred under the steep fronts of breaking waves with large fluid accelerations. Strong plunging breakers occurring intermittently caused very intense suspension events lasting for at least several seconds. Moderate suspension events were also observed under uprushing bores. The time-averaged sand fluxes on the equilibrium beach calculated from the measured time series were relatively small and not accurate enough to explain the equilibrium profile.

The time-averaged, cross-shore variation of suspended sediment concentration was predicted by combining the time-averaged, depth-integrated suspended

sediment model based on the sediment suspension and settling rates with the non-linear time-averaged irregular wave model CSHORE. Beach profile evolution tests were conducted to calibrate CSHORE and estimate the suspension rates which were found to be much larger than the rates of the bottom elevation change. Equilibrium profile tests were also conducted to verify CSHORE for its capability in predicting the cross-shore variations of the statistics of the free surface elevation and cross-shore velocity from outside the surf zone to the inner surf zone. The sediment model combined with the calibrated CSHORE is shown to be capable, at least qualitatively, of predicting the cross-shore variation of the measured suspended sediment concentration above the equilibrium profile.

Chapter 1

INTRODUCTION

The majority of the world's shoreline is suffering from erosion. Beach erosion will become more serious if the mean sea-level rise accelerates due to the greenhouse effect. However, the cross-shore sediment transport processes in surf zones on beaches are not understood quantitatively. No existing models can predict the long-term shoreline changes resulting from beach erosion during storms and beach recovery between storms as reviewed by Kobayashi and Johnson (2001).

Suspended sand concentrations measured on natural beaches have been found to be characterized by intermittent intense events that are not well correlated with the local free surface elevation and horizontal velocity as reviewed by Cox and Kobayashi (2000). The quantitative understanding and prediction of intermittent high sand concentrations are essential for predicting the cross-shore and longshore sediment transport rates in the surf zone on beaches.

The following study is an attempt to quantify the sediment suspension events that occur under irregular breaking waves in the nearshore environment. In light of the complexities associated with the nearshore processes, this study is limited to the cross-shore processes under the assumption of alongshore uniformity and normally incident waves. An equilibrium profile experiment was conducted to examine the intermittent suspension events at five cross-shore locations in a wave tank. The sand suspension events were measured and observed under shoaling waves on a rippled bed and under breaking waves and bores on a terraced beach.

Chapter 2 describes the equilibrium profile experiment and includes descriptions of the laboratory setup, experimental procedures, gauge locations and calibration methods, and measurements of the equilibrium profile. It also includes a concise report of the free surface, velocity and concentration statistics.

In Chapter 3 a relatively simple and computationally efficient time-averaged wave model CSHORE is calibrated with a series of tests conducted on an evolving sand beach. This wave model, based on the time-averaged shallow-water continuity, momentum, and energy equations with nonlinear correction terms, is capable of predicting the root-mean-square wave height, wave setup and free surface skewness from outside the surf zone to the inner swash zone. The model can be combined with linear progressive long-wave theory to predict the return current and the standard deviation of the cross-shore velocity. An attempt is made to extend the wave model to predict the cross-shore variations of the time-averaged sediment suspension rate, cross-shore sediment transport rate and bottom elevation change by coupling it with a time-averaged, depth-integrated continuity equation for suspended sediment.

Chapter 3 also gives a comparison between the model and the equilibrium profile tests described in Chapter 2. The time-averaged model was shown to be capable of predicting both the free surface statistics and the return current from outside the surf zone to the inner surf zone. The model is also capable, at least qualitatively, of predicting suspended sediment concentrations.

Both Chapters 2 and 3 are self contained and include individual introductions and conclusions. The summary of Chapter 2 has been submitted for publication by Kobayashi *et al.* (2001), whereas Chapter 3 is based on the conference paper by Giovannozzi *et al.* (2001). Chapter 4 gives an overall summary of the results from Chapters 2 and 3.

Chapter 2

INTERMITTENT INTENSE SAND SUSPENSION UNDER IRREGULAR SHOALING AND BREAKING WAVES

2.1 Introduction

Quantitative understanding of nearshore sand suspension processes is important for the prediction of cross-shore and longshore transport rates. The instantaneous concentration of suspended sand on natural beaches measured using optic and acoustic sensors indicated intermittent temporal variations in which the instantaneous concentration was intermittently much larger than the mean concentration [e.g., Downing *et al.* (1981); Hanes and Huntley (1986); Beach and Sternberg (1988), Beach and Sternberg (1992); Hanes (1991); Conley and Inman (1992); Jaffe and Sallenger (1992); Hay and Bowen (1994); Jaffe and Rubin (1996); Foster *et al.* (1996); Puleo *et al.* (2000)]. Possible mechanisms suggested for the intermittent concentration variations are bed forms, large waves in a wave group, vortices and turbulence generated by breaking waves and bores, wave-induced boundary ventilation, and coherent motions in the turbulent boundary layer.

The instantaneous concentration of suspended sand measured on natural beaches is difficult to interpret partly because of the lack of visual observations of sand suspension events and partly because of the temporal and alongshore variations of incident waves, water level, bathymetry and bottom sediments. It is easier to visually observe sand suspension events from the glass window of a wave flume,

although no proven similitude exists for sediment transport on natural beaches and laboratory beaches. Nadaoka *et al.* (1988) observed obliquely descending vortices generated by regular spilling waves to cause sand suspension in their laboratory experiment. Zhang and Sunamura (1994) observed both horizontal and oblique vortices generated by plunging and spilling waves. However, it is difficult to detect vortices from the measured fluid velocities even in laboratory experiments because oscillatory wave velocities are generally dominant inside the surf zone [e.g, Guza and Thornton (1980)]. Cox and Kobayashi (2000) identified intense intermittent coherent motions from the instantaneous horizontal and vertical turbulent velocities measured under regular spilling waves where the turbulent velocities were defined using phase averaging. The phase averaging is applicable only to regular waves and no proven method is available to obtain the instantaneous turbulent velocities for irregular waves. A new approach is required to detect the vortices and turbulence that cause sediment suspension under irregular waves.

An irregular wave experiment was conducted in a wave flume to observe and examine different mechanisms of sand suspension under shoaling, breaking, and broken waves under the assumptions of alongshore uniformity and normally incident waves. The three-dimensional velocities and sand concentrations were measured at 37 locations from outside the surf zone to the inner surf zone on an equilibrium beach. The measured alongshore (cross-flume) horizontal velocities are used to estimate the intensity and duration of the three-dimensional vortices and turbulence. The observed suspension mechanisms include sand suspension from the rippled bed under large shoaling waves in a wave group, intense suspension events under strong plunging breakers that occurred intermittently and moderate suspension events under bores. These sand suspension events tend to occur during the intervals of large alongshore velocity fluctuations. Relatedly, all the spectra of the measured alongshore velocities and concentrations are dominated by low frequency components.

2.2 Experiment

2.2.1 Experimental Setup

The experiments were conducted in a wave tank that was 30 m long, 2.4 m wide and 1.5 m high with a constant still-water depth of 90.0 cm as shown in Figure 2.1. A plywood beach with a 1:30 slope was constructed in the tank. Then a dividing wall was constructed along the centerline of the tank to reduce the volume of sand required for the experiment. A rear wall was also added to support the upper berm area of the beach. A fine sand beach was built with an initial slope of 1:12 in the 115-cm wide flume. Repeatable irregular waves, based on the TMA spectrum with significant wave height, $H_{mo} = 16$ cm, and the spectral peak period, $T_p = 4.8$ s, were generated with a piston-type wave paddle. A rock slope was located at the other end of the tank to absorb waves.

The sand beach was exposed to the specified incident irregular waves generated in a burst of 900 s to reduce the seiche in the wave tank. The sand beach became quasi-equilibrium with the bottom change less than 1 cm/hr after the exposure to the wave action for more than 50 hours. Beach profiles were measured along three cross-shore transects using a vernier pointer in the swash zone and an ultrasonic depth gauge in deeper water.

The equilibrium beach profile is depicted in Figure 2.7. The slopes of the foreshore, terrace, and offshore zone are approximately 1:6, 1:25 and 1:10, respectively. The shape of this equilibrium profile is similar to terraced profiles at Duck, North Carolina [e.g. Thornton *et al.* (1996); Gallagher *et al.* (1998)] but the slopes are considerably steeper. A similar experiment conducted by Orzech and Kobayashi (1998) with the spectral peak period $T_p = 1.6$ and 2.8 s resulted in similar profiles except for a small bar at the seaward end of the terrace. This indicates the limitations of these small-scale experiments in the wave flume of limited length using the fine sands whose diameters are comparable with those of natural beach sands.

No proven similitude exists for sediment transport on beaches, but this small scale experiment may be considered to correspond to a natural beach with fairly course sediment.

After the equilibrium beach profile was established, 37 tests were conducted where each test employed the same irregular waves lasting 900 s. Eight capacitance wave gauges were placed as shown in Figure 2.1 to measure the temporal variations of the free surface elevations. The offshore wave gauges were used to ensure the repeatability of the incident and reflected waves. The nearshore wave gauges A–E were placed at the cross-shore locations of the velocity and concentration measurements as shown in Figure 2.2. The vertical coordinate Z_b of the bottom profile is taken to be positive upward with $Z_b = 0$ at the still water level (SWL). Two acoustic-Doppler velocimeters (ADV) were used to measure the temporal variations of the fluid velocities at two locations simultaneously. A fiber optic sediment monitor (FOBS-7) with two sensors was used to measure the suspended sediment concentrations at two locations simultaneously. The sampling rate was 20 Hz for the free surface, fluid velocities and suspended sediment concentrations. The velocities and concentrations were measured at the elevations of 1, 2, ..., n cm above the local bottom where n = 20, 7, 4, 3 and 3 at A, B, C, D and E, respectively. The cross-shore and vertical locations of the velocity and concentration measurements are identified using the letters A to E followed by the numerical 1-n in Figure 2.2. For each of the 37 tests, the velocity and concentration measurements were made at each of these 37 locations.

Figure 2.3 depicts the alongshore locations of the sampling volumes of the velocity and concentration measurements relative to the center line of the 115-cm wide flume. The wave gauge was placed 22.5 cm laterally from the center line when the velocities and concentrations were measured at the same cross-shore location. The wave crests were visually observed to be uniform alongshore.

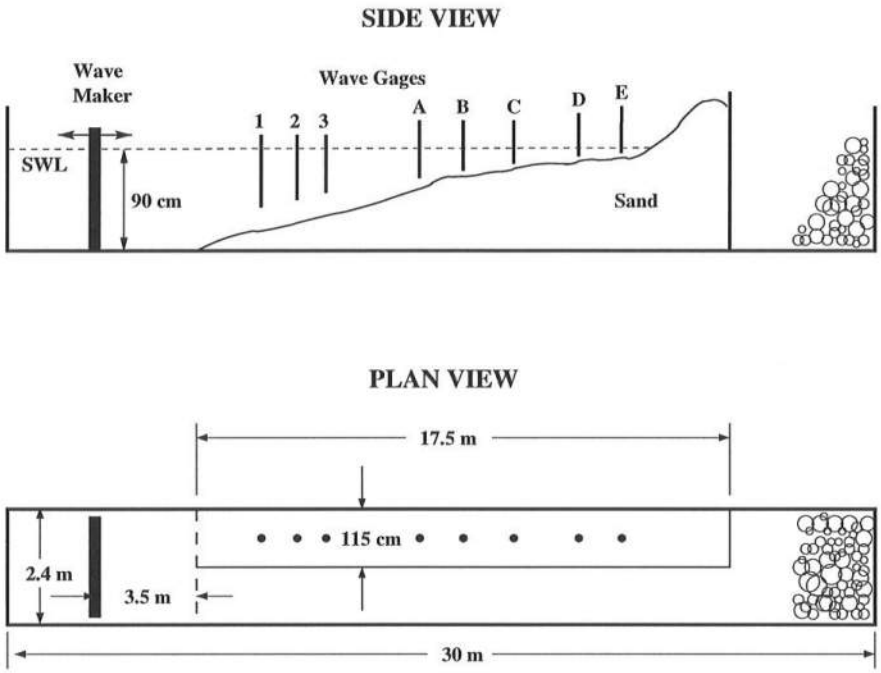

Figure 2.1: Experimental Setup

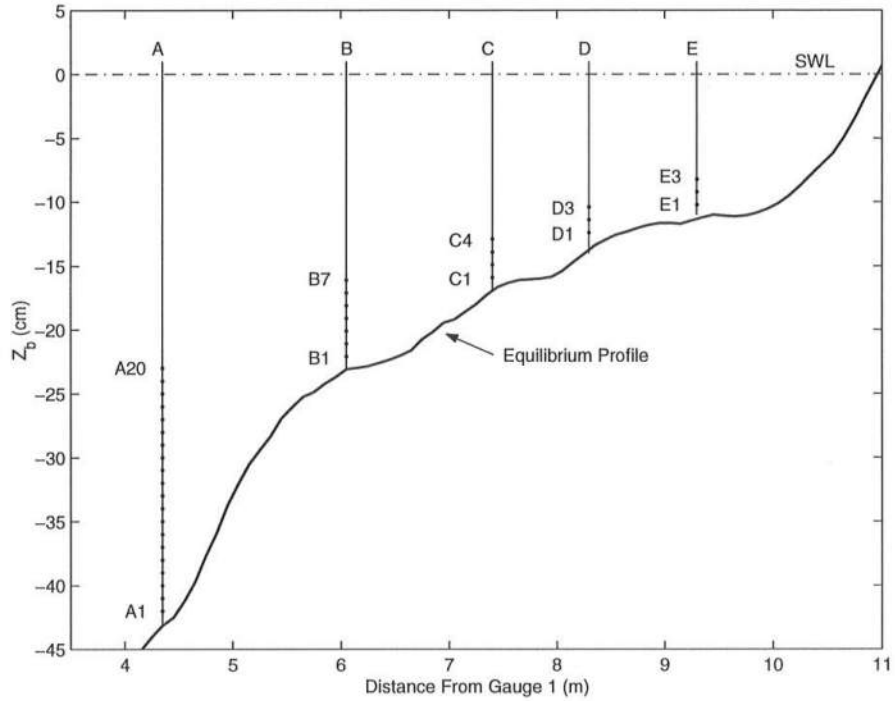

Figure 2.2: Test Locations

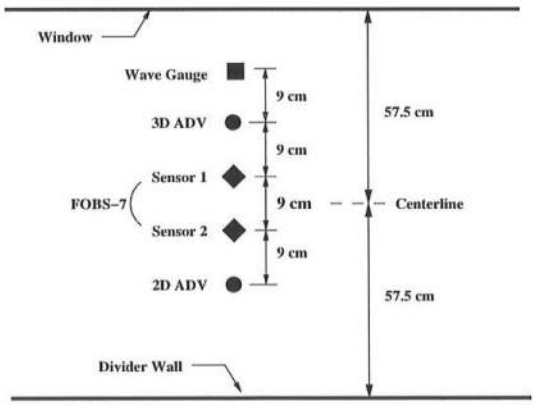

Figure 2.3: Alongshore Gauge Positions

2.2.2 Sand Characteristics

The sand beach was constructed of approximately 9 tons of fine quarry sand. Several tests were conducted to determine the basic characteristics of this sand. These tests measured the sand density, specific gravity, porosity, grain size distribution and fall velocity. The sand density was found from the ratio of the sand mass to the sand volume. Sand volume was determined by placing a known mass of sand in a graduated cylinder with a known volume of water. The amount of water displaced gave the volume of the sand. The specific gravity of the sand is defined as $s = \rho_s/\rho_w$, where ρ_w = density of pure water and ρ_s = density of sand. The moisture content of the sand was found to be insignificant as the average value was 0.44%. The porosity n_p was then found using the measured dry sand mass and volume together with the specific gravity. The average specific gravity was determined to be $s = 2.6$ and the porosity was found to be $n_p = 0.4$.

The sediment grain size distribution was measured using a sieve test procedure consisting of nine different sizes of sieves. The results of this test are shown graphically in Figure 2.4 and are summarized in Table 2.1. The relative steepness of the curve in Figure 2.4 indicates that the sand is of fairly uniform size. The mean grain size d_{50} was found to be 0.18 mm.

The sediment fall velocity was determined experimentally by dropping several sand grains from each size group into a clear glass cylinder filled with water. The motion of the grains was visually timed for a distance of one meter. For each size group, ten falls were recorded and then averaged to obtain a mean fall velocity for each group. This mean velocity was then multiplied by a weighting factor proportional to each size group's percent of the total mass. The mean fall velocity obtained from the weighted averages was found to be $w_f = 2.02$ cm/s. The sand size groups of 2.0 mm and 0.85 mm were omitted because the grain size was relatively large and only a few percent contributions from these two groups were present in

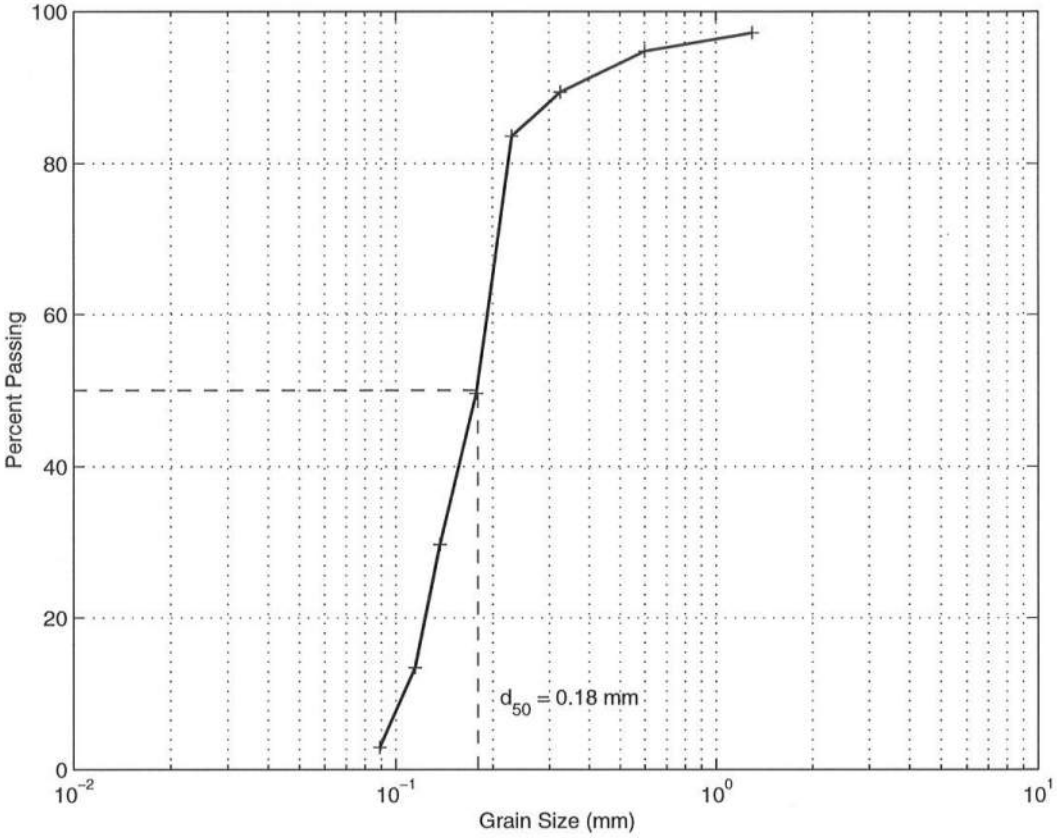

Figure 2.4: Sand Grain Size Distribution

Table 2.1: Summary of Sieve Test

Sieve Size (mm)	Geometric Mean Diameter (mm)	Mass (g)	Percent of M_{total}	Percent Passing
2.0	–	4.8	0.98	99.0
0.850	1.30	8.9	1.81	97.2
0.425	0.601	11.7	2.38	94.8
0.250	0.326	26.7	5.44	89.4
0.212	0.230	28.4	5.79	83.6
0.150	0.178	167.0	34.03	49.6
0.125	0.137	97.3	19.82	29.7
0.106	0.115	80.4	16.38	13.4
0.075	0.089	51.2	10.43	2.9
(Pan)	–	14.4	2.90	0.0
TOTALS		490.8	100	-

the whole sample. The results of the fall velocity test are summarized in Table 2.2. The fall velocity of $w_f = 2.0$ cm/s is used in the following.

2.2.3 Measurement of Beach Profiles

Detailed profile measurements of the beach were taken using a Panametrics 22DLHP ultrasonic depth gauge in deep water and a manual pointer with a vernier scale in the shallow swash zone. Profiles were taken directly before and immediately after the 37 tests on the equilibrium bottom to ensure that the profiles did not change more than 1 cm/hr.

Profiles were taken along three cross-shore transects to ensure that there were little longshore variations of the beach. The center transect was taken along the centerline of the experimental beach area and the other two were taken 23.5 cm on either side of the center transect. Each transect included 106 measurement points spaced at 10 cm, with an overlap of 2 points at the transition from the ultrasonic depth gage readings and the manual pointer readings. The longshore

Table 2.2: Fall Velocity Measurement Results

Sieve Size (mm)	Percent of M_{total}	Measured(cm/s) w_f (cm/s)
0.425	2.45	8.85
0.250	5.60	4.17
0.212	5.95	2.82
0.150	35.0	2.18
0.125	20.4	1.57
0.106	16.9	1.22
0.075	10.7	0.851
(Pan)	3.0	0.672
avg w_f		2.02 cm/s

variations were generally very small, especially in the swash zone were the beach became almost planar. Fairly uniform, two-dimensional ripples (< 1 cm in height) formed in the longshore direction slightly offshore of the breaker zone on the terrace and three-dimensional ripples were present further offshore. These ripples, which were observed to shift their position slightly during testing, account for the small variations in the three transects shown in Figures 2.5 and 2.6. The cross-shore distance in these figures corresponds to the shoreward distance from the coordinate origin at the location of wave gauge 1, as shown in Figure 2.1.

Representative profiles for each set were obtained by averaging the three transects and then smoothing the averaged transect with a three-point smoothing routine. Figure 2.7 shows the smoothed average profiles taken before and after the 37 tests. The small profile shifts that occurred during the 37 tests lasting 9.25 hr of wave action are represented by the differences between these two lines. Figure 2.8 shows that the erosion (negative) and accretion (positive) that occurred during the entire testing duration was, for the most part, less than 1 cm. The corresponding rate of elevation change was less than 0.1 cm/hr. Such an insignificant change confirms

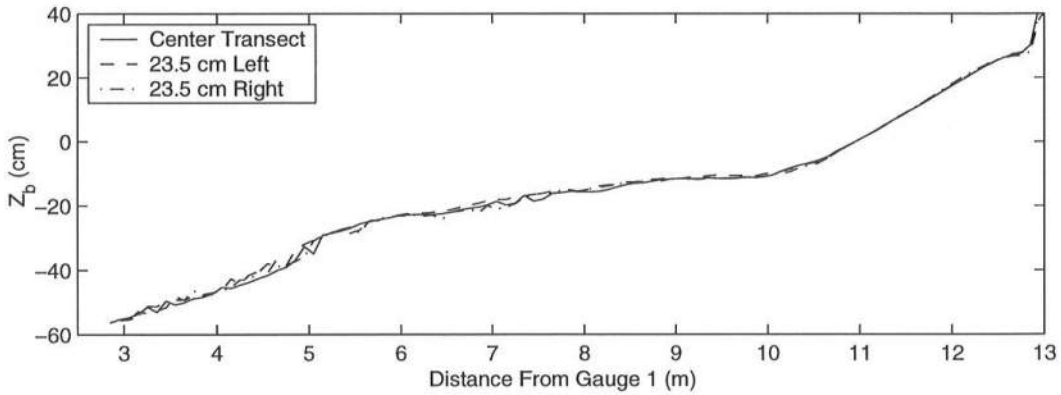

Figure 2.5: Unsmoothed Profiles at Three Transects (Pre-Test)

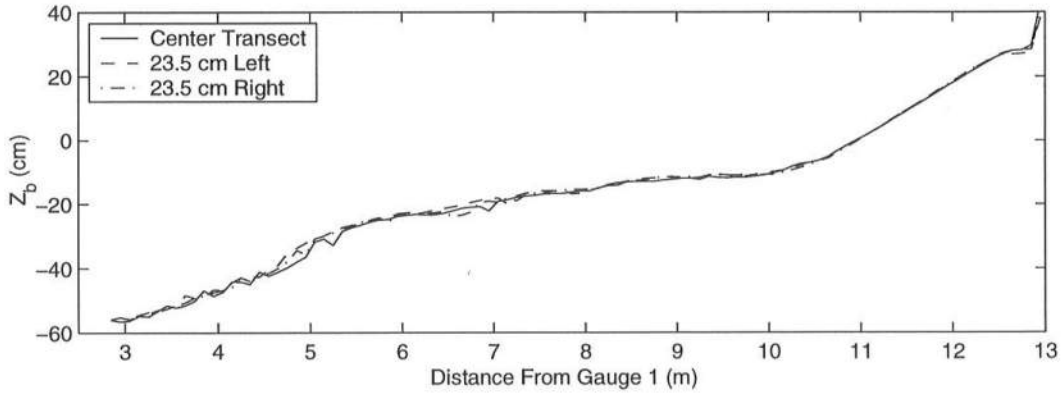

Figure 2.6: Unsmoothed Profiles at Three Transects (Post-Test)

that the profile was essentially in equilibrium. Erosion was slightly higher offshore in the vicinity of the three-dimensional ripples but no velocity or concentration data was taken in this region.

2.2.4 Wave Gauges

The cross-shore locations of the eight capacitance wave gages used to measure the temporal variations of the free surface elevations are shown in Figure 2.1. Wave gages 1, 2 and 3 were located offshore and used to separate the incident and reflected waves in order to ensure the repeatability of the irregular waves. The horizontal coordinate x in this chapter is taken to be positive shoreward with $x = 0$ at the location of wave gauge 1. For all 37 tests wave gauges 2 and 3 were located at $x =$ 0.85 and 1.85 m, respectively. The nearshore gauges were placed at the cross-shore locations of the velocity and concentration measurements as shown in Figure 2.2. Table 2.3 gives the cross-shore location x and the still water depth d for each wave gage.

Table 2.3: Wave Gauge Locations and Water Depths

Gauge	1	2	3	A	B	C	D	E
x (m)	0	0.85	1.85	4.35	6.05	7.40	8.30	9.30
d (cm)	80.0	73.5	64.3	43.1	23.1	16.9	13.4	11.2

Multiple wave gauge calibrations were conducted to ensure the repeatability and reliability of the wave gauges. Each calibration was performed after n runs were completed at each test location where $n = 20$, 7, 4, 3 and 3 for line A, B, C, D and E, respectively. Calibrations were conducted by raising the level of water in the tank 20 cm and then gradually draining the tank while recording gauge voltage readings for every 2 cm change in the water surface. This was done until the water level was 20 cm below the still water level, totaling 21 different voltage readings for each

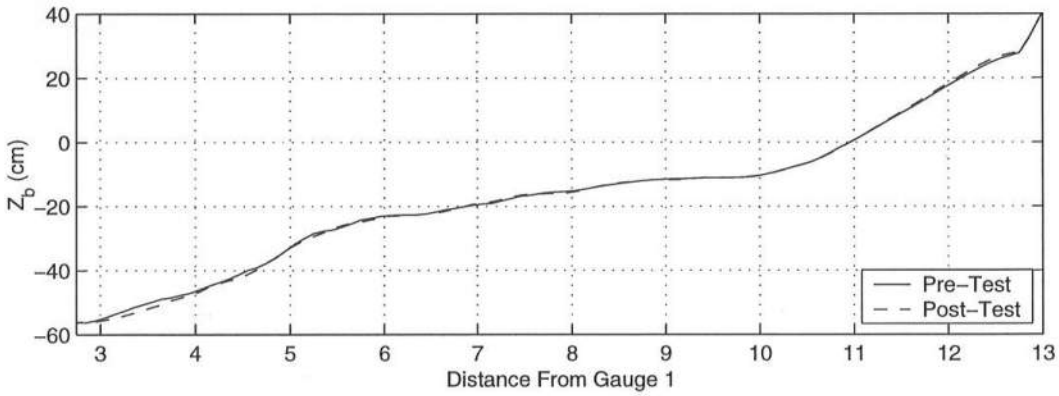

Figure 2.7: Equilibrium Profiles

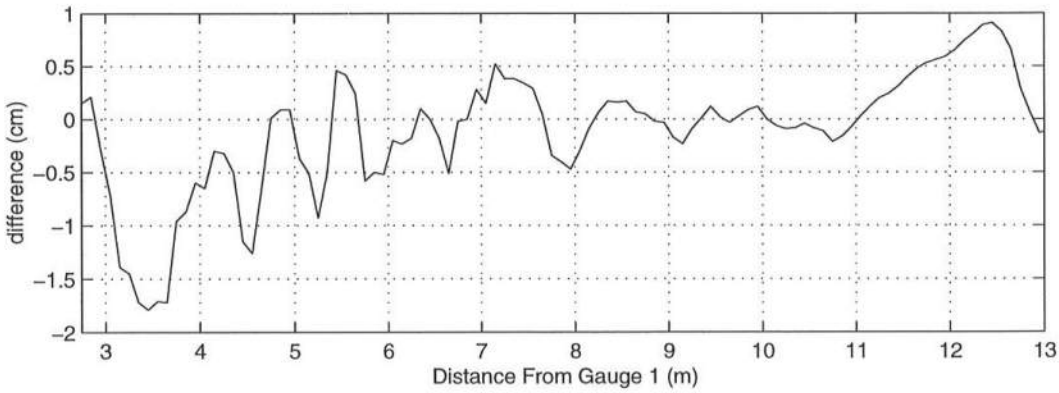

Figure 2.8: Difference Between Equilibrium Profiles

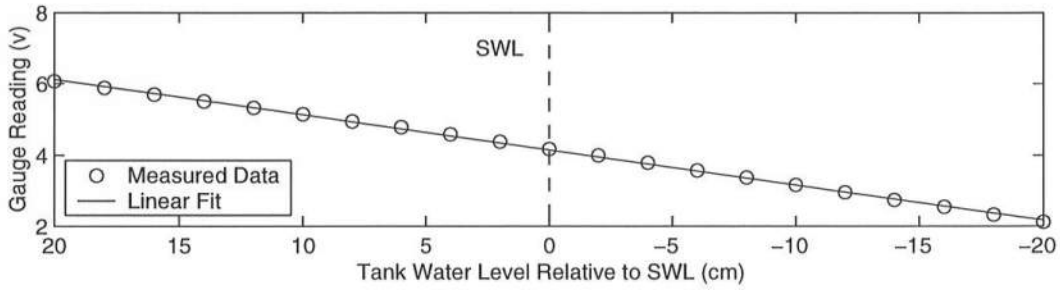

Figure 2.9: Wave Gauge Calibration, Gauge 1, After Test B7

wave gauge except for wave gauges at C–E limited by the bottom elevation. The calibration data followed a linear relation as shown for wave gauge 1 in Figure 2.9. A conversion factor was obtained from the best fit slope of all the data points. This slope is shown as the solid line in Figure 2.9. The vertical dashed line represents the elevation of the still water level during the wave tests. Calibration curves proved to be linear for all other wave gauges and were very repeatable.

2.2.5 Acoustic Doppler Velocimeters

A micro acoustic-Doppler velocimeter (ADV) with a 3D down-looking probe measured the cross-shore, alongshore and vertical velocities denoted as u_1, v_1 and w, respectively, at a distance of 5 cm from the probe tip. Another ADV with a 2D side-looking probe measured the cross-shore and alongshore velocities denoted as u_2 and v_2, respectively, at a distance of 5 cm from the probe tip. The sampling volume was approximately 0.1 cm^3 for both ADVs. The cross-shore and vertical locations of the sampling volumes of the ADVs are shown in Figure 2.2. The alongshore locations of the sampling volumes of the ADVs are shown in Figure 2.3. The sampling volumes were positioned at 37 different locations for the 37 tests. For each of the five cross-shore locations, the ADV sampling volumes were positioned at elevations 1, 2, ..., n cm above the local bottom where n = 20, 7, 4, 3 and 3 at lines A, B, C, D

and E, respectively. The highest elevation n cm above the local bottom at A–E in Figure 2.2 was imposed by the emergence of the 3D ADV probe in air.

In order to facilitate gauge setup, the ADVs were fixed to adjustable mounts that could be raised or lowered at 1 cm increments. Since the profile was in equilibrium, it was only necessary to find the exact location the first elevation at 1 cm above the local bottom. The elevations of the ADV sampling volumes were carefully measured with a tape measure to within $\pm$ 1 mm. The elevation of the 3D down-looking ADV could be confirmed with the ADV software supplied by its manufacturer and was correct to within $\pm$ 0.5 mm. The 2D ADV had a side-looking probe and its elevation was measured starting from the probe touching the local bottom.

The ADV software was used to convert the ADV voltage output into the corresponding velocity. Hence, calibration of the ADVs was not required. However, the measured velocities correspond to the velocities of the particulate matters in the sampling volume. Consequently, an additional test was conducted to examine the sensitivity of the ADVs measurement in the presence of falling sand grains in quiet water. When the sand particles passed through the sampling volume, the vertical velocity became slightly negative, indicating that the ADV measured the velocity of the sand particles in quiet water. However, it is unclear whether in the presence of waves the ADV measures the sand velocity or the water velocity with very fine particulate matters.

Velocity measurements lasting 60 s at a sampling rate of 20 Hz in the absence of waves in the flume indicated noise on the order of 1 cm/s or less for the horizontal velocities and on the order of 0.2 cm/s or less for the vertical velocities as shown in Figure 2.10. These velocities are regarded as the lower limits of the accurate velocity measurements.

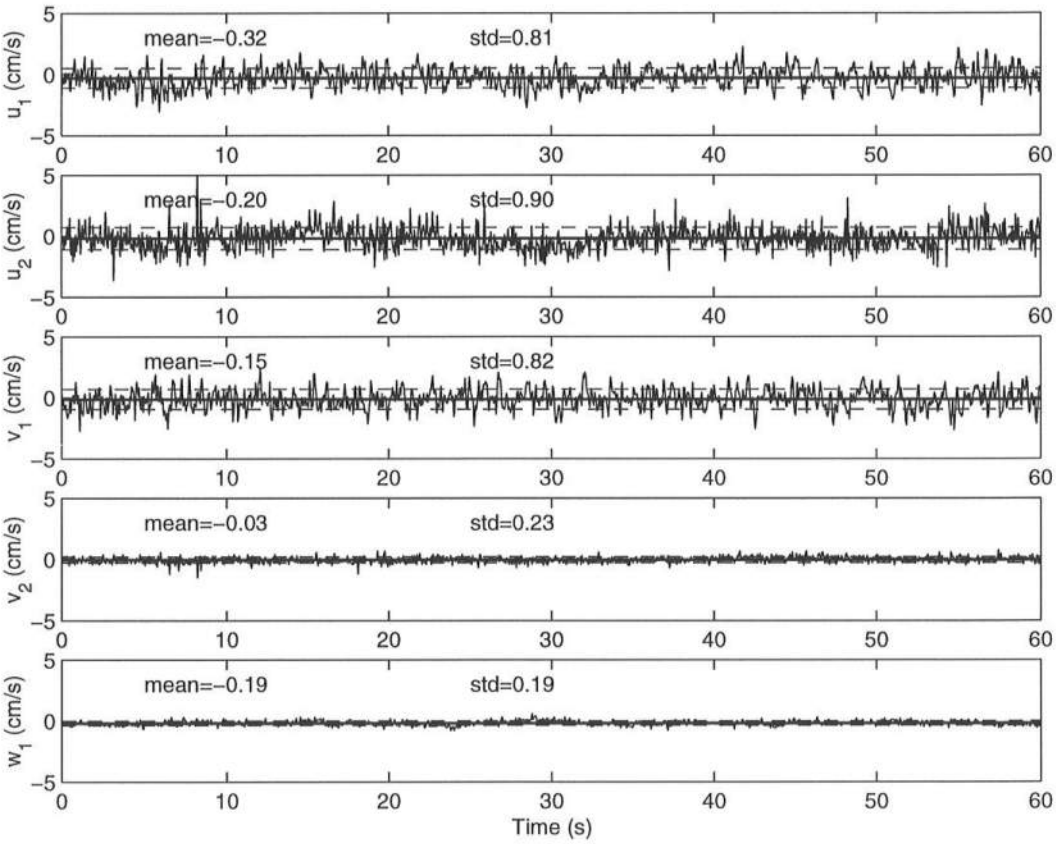

Figure 2.10: ADV Noise in Still Water

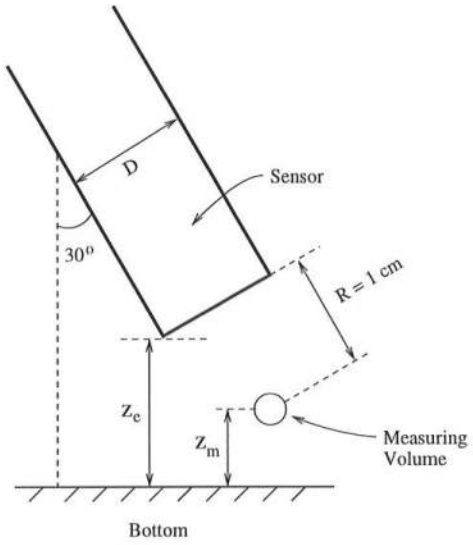

Figure 2.11: FOBS Sensor

2.2.6 Fiber Optic Sediment Monitor

A Fiber Optic Sediment Monitor (FOBS-7) with two sensors was used to measure suspended sediment concentrations C_1 and C_2 at the two alongshore locations indicated in Figure 2.3. The FOBS-7 is a laboratory version of OBS-3 sensors used for concentration measurements on natural beaches [e.g. Downing *et al.* (1981)]. The sediment monitor measures particle concentration by detecting infrared radiation (IR) backscattered from particles. The measurement area of the sensors is confined to the volume where the transmit and receive beams intersect. This sampling volume is approximately 10 mm^3 and is located at a distance of approximately 1.0 cm from the sensor tip as shown in Figure 2.11.

The vertical distance Z_m of the sampling volume above the local bottom was determined by raising the sensor at intervals of 0.2 cm and reading the corresponding voltage in the absence of waves. The voltage decreased rapidly when the sampling volume emerged above the bed as shown in Figure 2.12 where Z_e is the measured

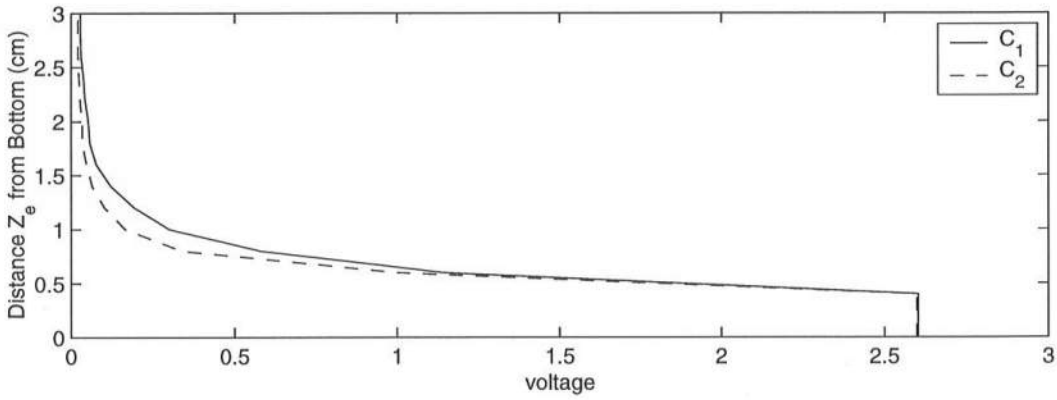

Figure 2.12: Voltage Decay With Distance Z_e From Bottom

elevation of the sensor edge above the local bottom. The voltage was practically zero at $Z_e = 1.6$ cm above the bed.

The cross-shore and vertical locations of the sampling volumes of the two sediment sensors were identical to that of the ADVs as shown in Figure 2.2. The alongshore locations of the sampling volumes are shown in Figure 2.3. A total of 37 locations were sampled for the 37 tests. The sensors were mounted on vertically adjustable rods, similar to those of the ADVs, that could be raised or lowered by 1 cm increments. Therefore, it was only necessary to find the exact position of the sampling volumes for the first elevation at 1 cm above the local bottom. The sensors were mounted at an angle of 30^o from the vertical as shown in Figure 2.11. Using simple geometric relationships, the elevation Z_m of the sampling volume was found to be $Z_m = (Z_e - R\cos\theta + D/2\sin\theta)$, where R is the distance from the sensor tip to the sampling volume shown above to be 1 cm, the diameter of the sensor D is 1 cm, and $\theta = 30^o$. Thus, the sampling volume elevation of $Z_m = 1$ cm corresponds to $Z_e = 1.6$ cm. As a result, $Z_e = 0.6$ cm was regarded to correspond to $Z_m = 0$ cm on the local bottom.

The relationship between voltage and sand concentration for each sensor was

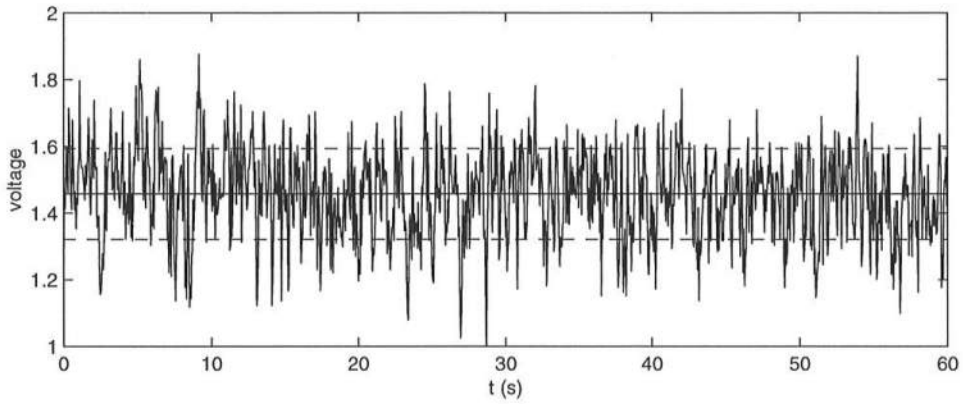

Figure 2.13: FOBS Time Series Used for Calibration, Sensor 1, $Z_m = 7$ cm, $C = 16$ g/L

obtained by measuring the times series of the voltage sampled at a rate of 20 Hz for 60 s for known sand concentrations in a well-mixed blender. The time-averaged voltage was used to establish the calibration relationship, whereas the fluctuating voltage was used to assess the error or uncertainty of this relationship which was about 20% due to the variability caused by the small sampling volume of 10 mm.[3] Figure 2.13 shows a sample calibration time series for sensor 1 with a concentration of $C = 16$ g/L sampled at an elevation $Z_m = 7$ cm above the bottom of the blender. The solid horizontal line represents the time-averaged value of the temporal variation of the voltage and the horizontal dashed lines represent $\pm$ one standard deviation.

To ensure there was no stratification in the blending apparatus, time series were recorded for elevations 7, 8 and 9 cm above the bottom of the blender. Figure 2.14 shows the time-averaged voltages denoted by the circle for sensor 1 for concentration of $C = 0$, 4, 8, 12, 16, 20, 24 and 28 g/L for elevations $Z_m = 7$, 8 and 9 cm. The solid lines in this figure represent the vertically averaged voltage and the dashed lines represent $\pm$ one standard deviation of the combined times series for $Z_m = 7$, 8 and 9 cm. The vertically averaged values listed in Figure 2.14 were

then plotted versus concentration in Figures 2.15 and 2.16 before and after the 37 tests. In these figures the solid line represents a cubic spline fit to the data and the squares represent ± one standard deviation.

Calibration tests were also conducted to examine the influence of air bubbles on the FOBS readings. High blending speeds produced vortices and air bubbles which did effect FOBS readings. However, with a variable transformer, an adequate blending speed could be obtained that formed practically no bubbles while still maintaining a uniform mixture. The bubble formation in the presence of breaking waves may have some effect on the FOBS readings but their presence in the small sampling volume of 10 mm^3 may be very short.

Calibrations of the FOBS meter were conducted before and after the 37 tests with no significant deviation as shown in Figures 2.15 and 2.16 for sensor 1. The dots represent the time-averaged, vertically averaged voltages for each known concentration. The squares represent the mean ± one standard deviation. The solid lines are a cubic spline fit to the data. The data in Figures 2.15 and 2.16 were averaged to obtain the final calibration curve shown in Figure 2.17. In this figure the axes were reversed in order to illustrate the error of the instrument in grams per liter of sand concentration for a given voltage. This figure indicates that at low concentrations the error is on the order of 1 g/L and can be as high as 5 g/L for higher concentrations. In summary, the error or uncertainty of the calibration curve is about 20% mostly because the small sampling volume of 10 $mm.^3$

2.2.7 Experimental Procedures

The calibrated wave gauges, ADVs and FOBS sediment monitor were all attached to a 16 channel National Instruments data acquisition board to allow synchronous data collection for each test. All data was sampled at a sampling rate of 20 Hz for the duration of 900 s. The three offshore wave gages were used to ensure

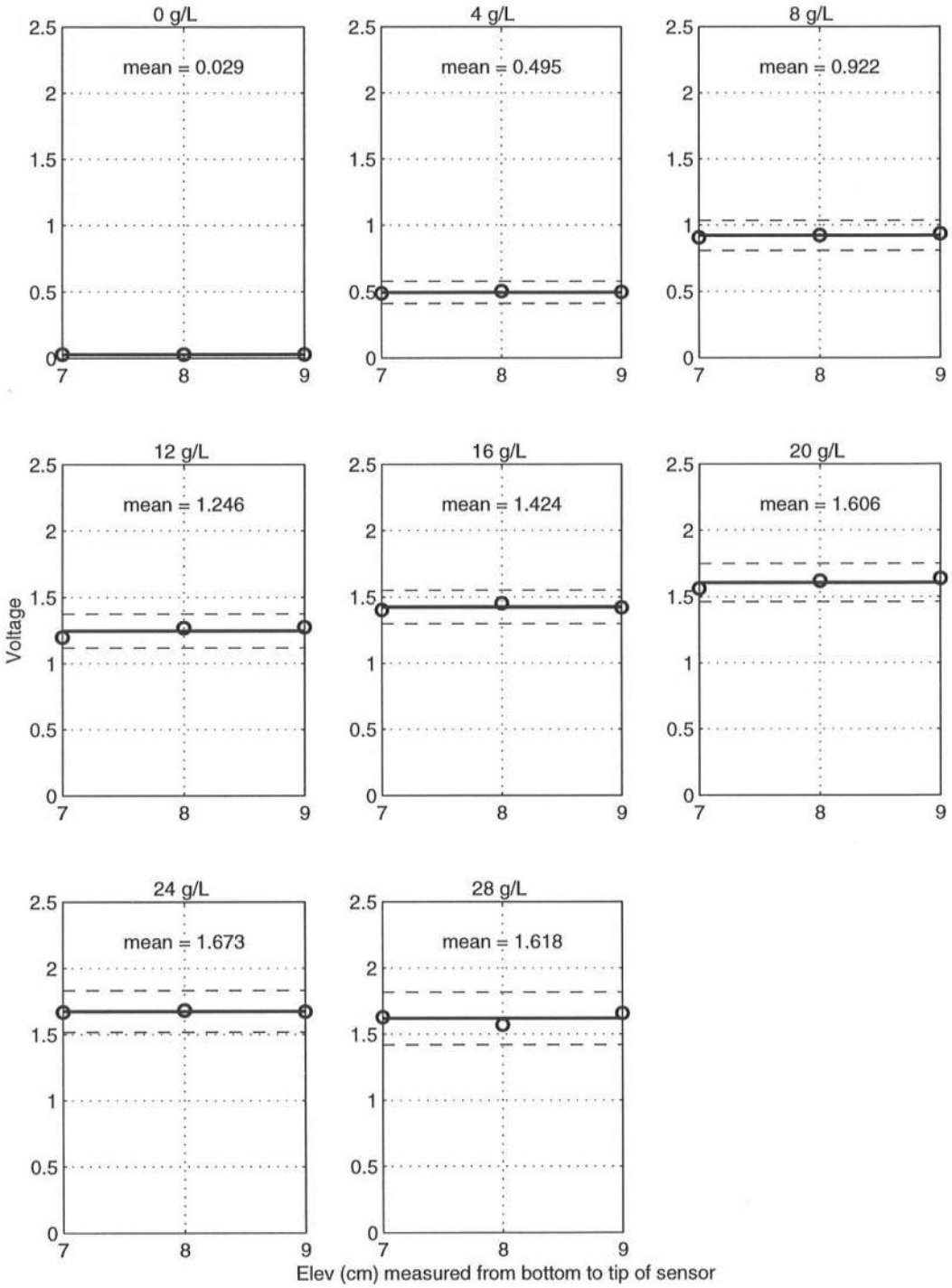

Figure 2.14: Time-Averaged Voltages at Elevations 7, 8 and 9 cm for $C = 0$, 4, 8, 12, 16, 20, 24 and 28 g/L

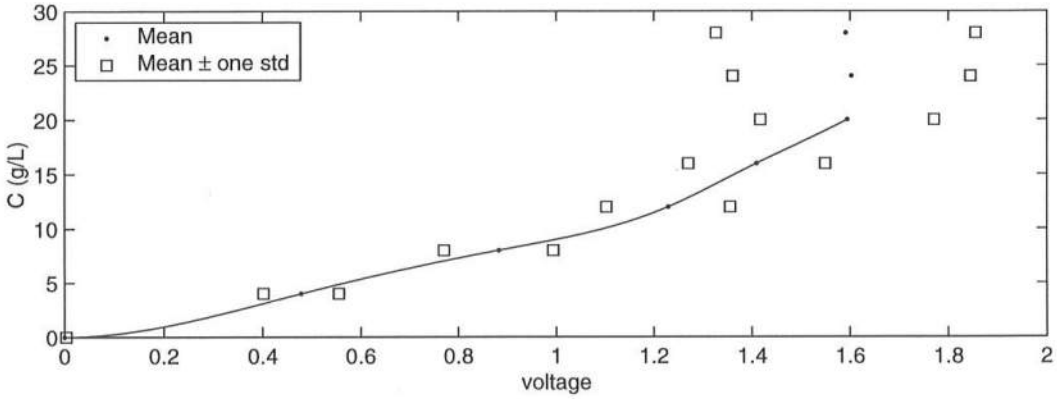

Figure 2.15: FOBS Calibration Curve for Sensor 1 (Pre-Test)

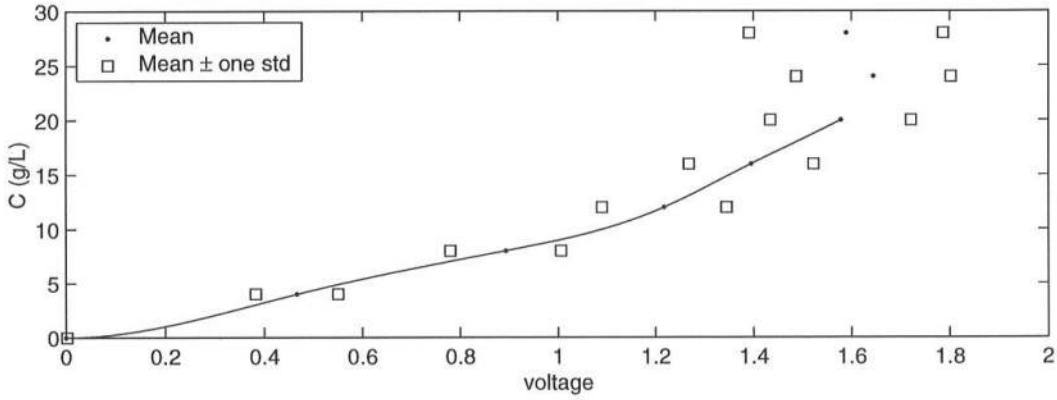

Figure 2.16: FOBS Calibration Curve for Sensor 1 (Post-Test)

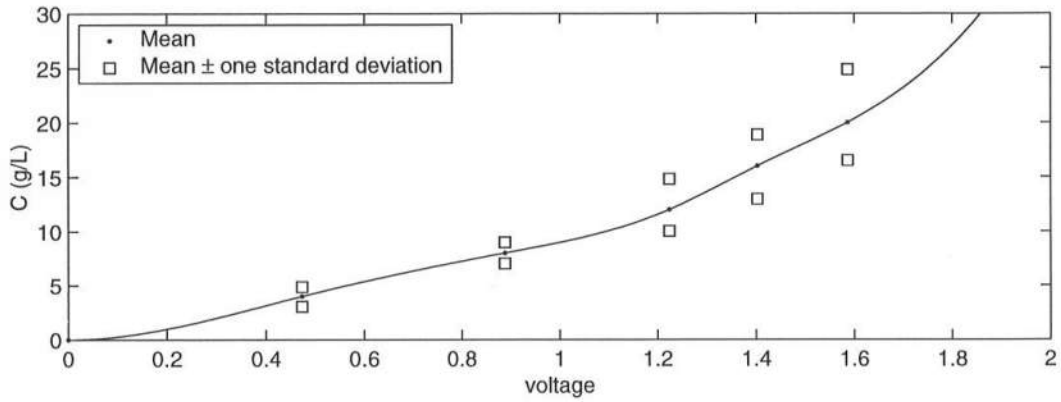

Figure 2.17: Combined FOBS Calibration Curve for Sensor 1

the repeatability of the generated waves. The five onshore wave gauges were co-located with the ADVs and FOBS sensors at locations A, B, C, D and E as shown in Figure 2.2. The ADVs and FOBS sensors were repositioned 37 times for the 37 tests as shown in Figure 2.2. The same burst of irregular waves lasting 900 s was repeated for each of the 37 tests. The bottom profile was measured immediately before and after the 37 tests to ensure that no significant profile changes occurred. In summary, the time series of u_1, u_2, v_1, v_2, w, C_1 and C_2 as well as the time series of the free surface elevations η above SWL at the eight wave gauges were measured for 900 s for each of the 37 tests. The sampling rate for all the time series was 20 Hz. The initial transition of 60 s starting from no wave action at time $t = 0$ was removed from each time series for the subsequent statistical and spectral analyses.

2.2.8 Incident and Reflected Waves

The repeatability of the generated waves was checked by separating the incident and reflected waves for each of the 37 tests. The separated incident and reflected wave spectra at the location of wave gauge 1 were plotted together for all

37 runs, as shown in Figure 2.18 where the spectra were smoothed using band averaging with 16 degrees of freedom. The plotted spectra for the incident and reflected waves were almost identical, proving the repeatability of the tests. Table 2.4 lists the average values of the incident wave spectral peak period T_p, the incident spectral significant wave height H_{mo} and the spectral reflection coefficient R for the spectra shown in Figure 2.18.

Table 2.4: Incident Wave Characteristics

T_p (s)	H_{mo} (cm)	R
4.8	15.4	0.33

Table 2.5 lists the spectral significant wave height H_{mo} and the root-mean-square wave height $H_{rms} = \sqrt{8}\sigma_\eta$ with σ_η = standard deviation of the free surface elevation η at gauges 1, 2 and 3 for each of the 37 tests to indicate the degree of repeatability of the wave heights within about 1%.

Table 2.6 lists the mean and skewness of the measured free surface elevation η at gauges 1, 2 and 3 for each of the 37 tests to confirm the repeatability of the measured time series of η at these gauges.

2.3 Overview of Data

2.3.1 Free Surface Elevations

The irregular waves did not break at gauge A, were breaking frequently at gauge B, broke intensely sometimes at gauge C and D, and became bores at gauge E. The times series of the free surface elevation η at the eight wave gauges were repeatable within approximately 1% differences for the 37 tests. The statistics of η

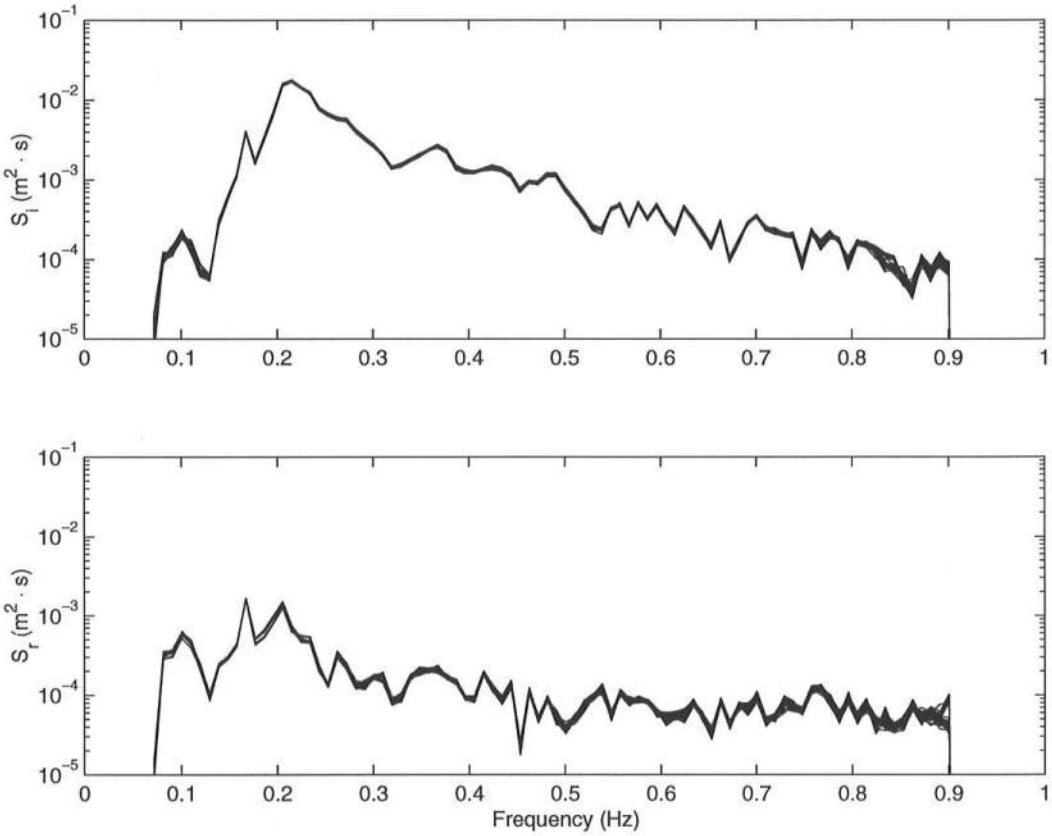

Figure 2.18: Frequency Spectra for Reflected and Incident Waves for 37 Tests

Table 2.5: H_{mo} and H_{rms} for 37 Tests

Test	Gauge 1		Gauge 2		Gauge 3	
	H_{mo} (cm)	H_{rms} (cm)	H_{mo} (cm)	H_{rms} (cm)	H_{mo} (cm)	H_{rms} (cm)
A1	16.4	11.6	16.1	11.4	15.7	11.1
A2	16.4	11.6	16.1	11.4	15.7	11.1
A3	16.4	11.6	16.2	11.4	15.7	11.1
A4	16.4	11.6	16.2	11.4	15.7	11.1
A5	16.5	11.7	16.2	11.5	15.7	11.1
A6	16.5	11.6	16.2	11.4	15.7	11.1
A7	16.5	11.6	16.2	11.4	15.7	11.1
A8	16.5	11.6	16.2	11.4	15.7	11.1
A9	16.5	11.6	16.2	11.4	15.7	11.1
A10	16.5	11.7	16.2	11.4	15.7	11.1
A11	16.4	11.6	16.2	11.4	15.7	11.1
A12	16.5	11.6	16.2	11.4	15.7	11.1
A13	16.5	11.6	16.2	11.4	15.7	11.1
A14	16.5	11.6	16.2	11.4	15.7	11.1
A15	16.5	11.7	16.2	11.4	15.7	11.1
A16	16.5	11.7	16.2	11.4	15.7	11.1
A17	16.5	11.6	16.2	11.4	15.7	11.1
A18	16.5	11.7	16.2	11.4	15.8	11.2
A19	16.4	11.6	16.1	11.4	15.7	11.1
A20	16.4	11.6	16.1	11.4	15.7	11.1

Table 2.5: Continued

Test	Gauge 1		Gauge 2		Gauge 3	
	H_{mo} (cm)	H_{rms} (cm)	H_{mo} (cm)	H_{rms} (cm)	H_{mo} (cm)	H_{rms} (cm)
B1	16.0	11.3	15.9	11.2	15.8	11.2
B2	16.0	11.3	15.9	11.3	15.8	11.2
B3	16.0	11.3	15.9	11.3	15.8	11.2
B4	16.1	11.4	16.0	11.3	15.8	11.2
B5	16.0	11.3	15.9	11.3	15.8	11.2
B6	16.0	11.3	16.0	11.3	15.8	11.2
B7	16.0	11.3	15.9	11.3	15.8	11.2
C1	15.9	11.3	15.8	11.1	15.3	10.8
C2	16.1	11.4	15.9	11.3	15.5	11.0
C3	16.1	11.4	16.0	11.3	15.5	11.0
C4	16.1	11.4	16.0	11.3	15.5	11.0
D1	16.5	11.7	15.7	11.1	15.4	10.9
D2	16.2	11.4	15.7	11.1	15.4	10.9
D3	16.1	11.4	15.7	11.1	15.4	10.9
E1	16.4	11.4	16.1	11.4	15.9	11.2
E2	16.4	11.6	16.1	11.4	15.9	11.2
E3	16.4	11.6	16.1	11.4	15.9	11.2
AVG	16.3	11.5	16.1	11.3	15.7	11.1

Table 2.6: $\overline{\eta}$ and *skew* for 37 Tests

Test	Gauge 1		Gauge 2		Gauge 3	
	$\overline{\eta}$ (cm)	*skew*	$\overline{\eta}$ (cm)	*skew*	$\overline{\eta}$ (cm)	*skew*
A1	-0.1	0.17	-0.2	0.21	-0.2	0.17
A2	-0.1	0.18	-0.2	0.18	-0.2	0.18
A3	-0.1	0.18	-0.2	0.22	-0.2	0.18
A4	-0.1	0.17	-0.1	0.22	-0.2	0.19
A5	-0.1	0.18	-0.2	0.22	-0.2	0.19
A6	-0.1	0.17	-0.2	0.22	-0.2	0.18
A7	-0.1	0.18	-0.1	0.22	-0.2	0.19
A8	-0.1	0.18	-0.2	0.22	-0.2	0.19
A9	-0.1	0.18	-0.1	0.22	-0.2	0.19
A10	-0.1	0.18	-0.1	0.22	-0.2	0.19
A11	-0.1	0.18	-0.2	0.22	-0.2	0.19
A12	-0.1	0.18	-0.2	0.22	-0.2	0.19
A13	-0.1	0.18	-0.1	0.22	-0.2	0.19
A14	-0.1	0.18	-0.2	0.22	-0.2	0.20
A15	-0.1	0.19	-0.1	0.22	-0.2	0.19
A16	-0.1	0.19	-0.1	0.22	-0.2	0.19
A17	-0.1	0.18	-0.2	0.22	-0.3	0.19
A18	-0.1	0.18	-0.2	0.21	-0.2	0.19
A19	-0.2	0.18	-0.2	0.22	-0.2	0.18
A20	-0.1	0.18	-0.1	0.21	-0.2	0.19

Table 2.6: Continued

Test	Gauge 1		Gauge 2		Gauge 3	
	$\overline{\eta}$ (cm)	*skew*	$\overline{\eta}$ (cm)	*skew*	$\overline{\eta}$ (cm)	*skew*
B1	-0.1	0.16	-0.1	0.17	-0.1	0.19
B2	-0.1	0.16	-0.1	0.17	-0.1	0.19
B3	-0.1	0.16	-0.1	0.18	-0.2	0.19
B4	-0.1	0.17	-0.1	0.18	-0.1	0.19
B5	-0.1	0.16	-0.2	0.18	-0.2	0.19
B6	-0.1	0.16	-0.2	0.19	-0.1	0.19
B7	-0.1	0.16	-0.1	0.18	-0.2	0.19
C1	-0.1	0.19	-0.2	0.20	-0.2	0.17
C2	-0.1	0.18	-0.1	0.21	-0.2	0.18
C3	-0.1	0.19	-0.2	0.22	-0.2	0.18
C4	-0.1	0.18	-0.1	0.22	-0.2	0.19
D1	-0.1	0.18	-0.1	0.21	-0.2	0.19
D2	-0.1	0.18	-0.1	0.21	-0.2	0.19
D3	-0.1	0.19	-0.1	0.22	-0.2	0.19
E1	-0.1	0.19	-0.1	0.21	-0.2	0.19
E2	-0.1	0.19	-0.2	0.22	-0.2	0.18
E3	-0.1	0.19	-0.1	0.22	-0.1	0.19
AVG	-0.1	0.18	-0.1	0.21	-0.2	0.19

at these gauges are listed in Table 2.7 where x is the landward distance from wave gauge 1, d is the still water depth, $\overline{\eta}$ is the mean of η with the overbar denoting time averaging, $H_{\rm rms}$ is the root-mean-square wave height defined as $H_{\rm rms}=\sqrt{8}\sigma_\eta$ using the standard deviation σ_η of η and skew is the skewness of η. The mean $\overline{\eta}$ decreased to -0.5 cm (set-down) at gauge B and increased to 0.8 cm (setup) at gauge E. The wave height H_{rms} increased to 13.1 cm at gauge A, decreased to 10.6 cm at gauge C and increased slightly at gauge D before the decrease at gauge E, possibly due to the transition from breaking waves to bores at gauge D. The skewness tended to increase landward.

Figure 2.19 shows the free surface frequency spectra $S\eta$ at gauges A–E where all spectra were computed using band averaging with 16 degrees of freedom. The spectra plotted in this figure correspond to the free surface elevations measured simultaneously with the velocities and concentrations at the same cross-shore location to facilitate the comparisons of different spectra. Consequently, the number of the plotted spectra at each gauge is the same as the number of points along the vertical line at the gauge location in Figure 2.2. The spectral peak at the frequency $f_p = 0.21$ Hz decreased landward and the low frequency components increased landward. This can be seen in Figure 2.20 where the mean spectral values for each gauge location are plotted together from gauge A to C and from gauge C to E.

2.3.2 Cross-Shore Velocities

The horizontal velocities u_1 and u_2 measured by the 3D ADV and the 2D ADV, respectively, varied little vertically at lines A–E in Figure 2.2. The waves landward of line A were essentially in shallow water. The ratio between the linear wavelength L_p for $T_p = 4.8$ s and the mean water depth $h = (d + \overline{\eta})$ was 23 at line A as shown in Table 2.8 for the gauge locations A–E. The only exception was the time series of u_1 for test A1 (1 cm above the bottom at line A) which was reduced for extended intervals possibly by shifting ripples.

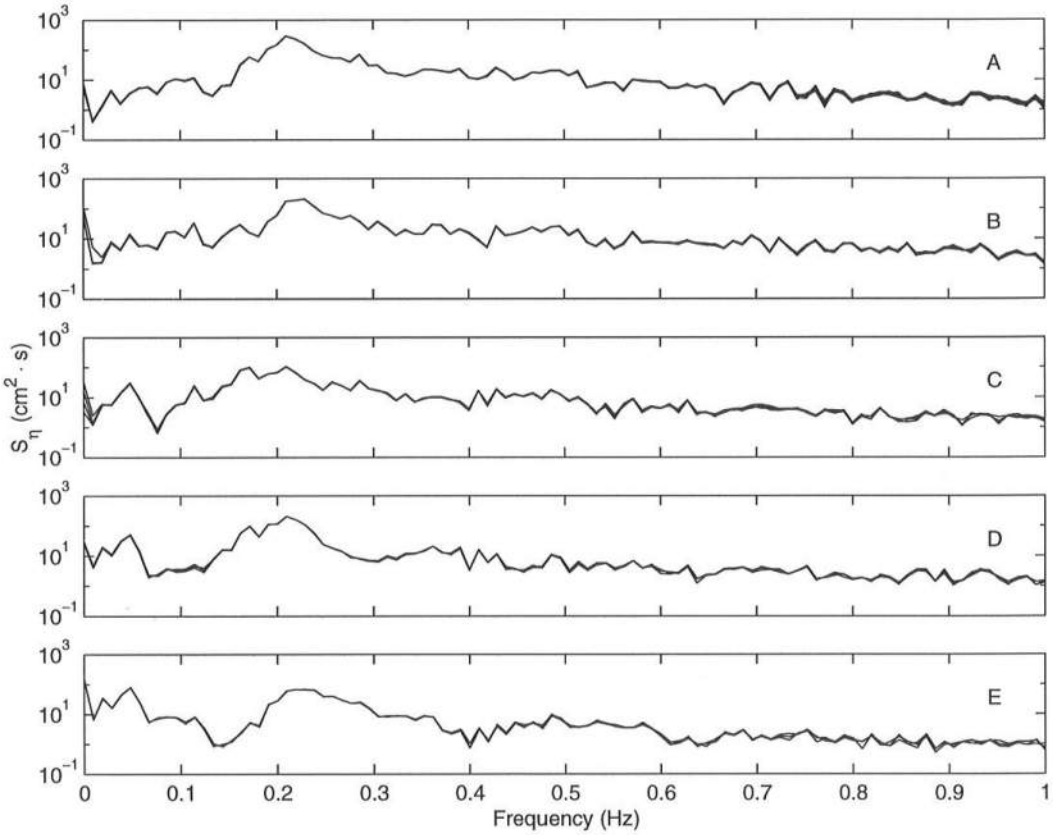

Figure 2.19: Free Surface Frequency Spectra

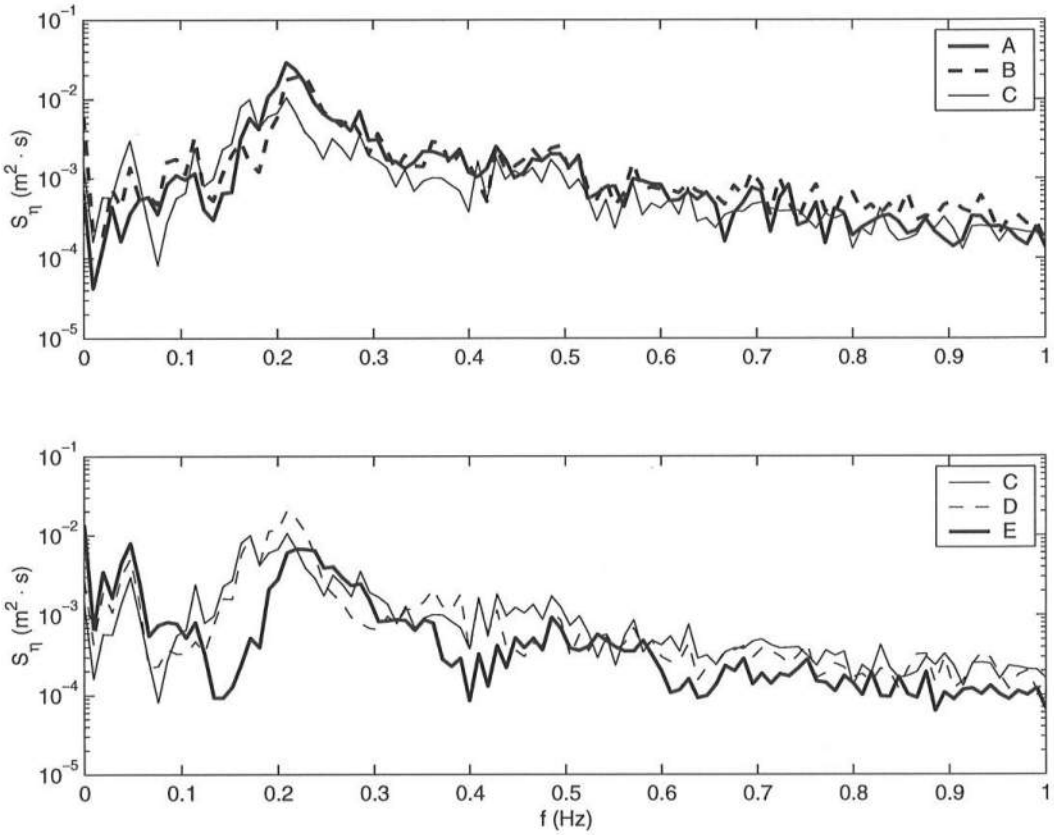

Figure 2.20: Comparisons of Free Surface Frequency Spectra

Table 2.7: Free Surface Elevation Statistics

Wave Gauge	x (m)	d (cm)	$\overline{\eta}$ (cm)	H_{rms} (cm)	*skew*
1	0	80.0	-0.1	11.5	0.18
2	0.85	73.5	-0.1	11.3	0.21
3	1.85	64.3	-0.2	11.1	0.19
A	4.35	43.1	-0.2	13.1	0.30
B	6.05	23.1	-0.5	13.0	0.48
C	7.40	16.9	-0.2	10.6	0.31
D	8.30	13.4	0.3	11.4	0.52
E	9.30	11.2	0.8	8.9	0.91

Table 2.8: Linear Wavelength and Period

Wave Gauge	d (cm)	h (cm)	T_p (s)	L_p (m)	L_p/h
A	43.1	42.9	4.8	9.72	22.7
B	23.1	22.6	4.7	7.00	31.0
C	16.9	16.7	5.8	7.42	44.4
D	13.4	13.7	4.8	5.56	40.6
E	11.2	12.0	20.0	21.70	180.8

The ripple migration was not measured in this experiment for lack of a high resolution profiler such as that used by Crawford and Hay (2001). Three-dimensional ripples were present in the vicinity and seaward of line A in Figure 2.2. The height and cross-shore wavelength of these ripples were approximately 2 cm and 11 cm, respectively. The ripples became more two-dimensional and their heights decreased landward. No ripples were visible landward of line B.

The ripples observed in this experiment are compared with those created in the large oscillating water tunnel experiment by Ribberink and Al-Salem (1994). The mobility number Ψ and the Shields parameter θ' based on the grain roughness

are calculated in the same way as their calculations except that the significant amplitude U_s of the near-bed horizontal velocity is estimated simply as $U_s = 2\sigma_u$ [e.g., Crawford and Hay (2001)] with σ_u being the standard deviation of the measured u_2 at 1 cm above the bottom. At line A, $U_s = 32$ cm/s, $T_p = 4.8$ s, $\Psi = 37$ and $\theta' = 0.18$. These values are similar to their experiment 17 in series B for which three-dimensional ripples were created and their height and length were 1.4 cm and 11 cm, respectively. Consequently, these ripples are similar to the ripples at line A. On the other hand, for line B–E, $\Psi = 85$-120 and $\theta' = 0.32$-0.42 in the transition between rippled and plane beds [Ribberink and Al-Salem (1994); Crawford and Hay (2001)] in the absence of frequent wave breaking.

Table 2.9 lists the vertically averaged values of the mean, standard deviation and skewness of u_1 and u_2 at lines A–E shown in Figure 2.2. The differences between the listed values of u_1 and u_2 may indicate the errors of the cross-shore velocity measurements, although u_1 and u_2 were measured at the different alongshore locations using the different sensors as shown in Figure 2.3. The measured time series of u_1 and u_2 were essentially in phase and indistinguishable visually apart from small high-frequency fluctuations related to vortices and turbulence. The cross-shore velocity u is taken to be positive landward and the mean current $\overline{u}$ is undertow. The vertical variations of the mean, standard deviation and skewness of u were relatively small and comparable with the differences for u_1 and u_2 in Table 2.9. The standard deviation σ_u did not decrease at line C unlike $H_{rms} = \sqrt{8}\sigma_\eta$ in Table 2.7, indicating potential energy loss before the kinetic energy loss due to wave breaking. The skewness of u was negative at line B for an unknown reason and at line E possible due to the effect of down-rush from the swash zone which was noticeable visually. The skewness of u was smaller than the skewness of η at the same line as noticed in the previous experiment by Kobayashi *et al.* (1998).

Figure 2.21 shows the spectra S_u of u at lines A–E corresponding to the

Table 2.9: Statistics of Cross-Shore Velocities

	Mean (cm/s)		σ_u (cm/s)		*skew*	
Line	u_1	u_2	u_1	u_2	u_1	u_2
A	-2.0	-1.9	18.4	17.6	0.26	0.26
B	-6.3	-6.9	27.8	30.4	-0.34	-0.34
C	-6.7	-6.9	27.3	30.4	0.18	0.28
D	-7.0	-7.3	23.2	26.0	0.07	0.31
E	-5.5	-4.8	25.5	27.0	-0.35	-0.31

spectra S_η shown in Figure 2.19. The spectra for both u_1 and u_2 are plotted in Figure 2.21. The single curve below the other 39 curves at line A corresponds to the spectrum for u_1 for test A1 discussed above. The segments of S_η and S_u corresponding to wind wave frequencies at the same line in Figures 2.19 and 2.21 may be related using linear progressive wave theory [Guza and Thornton (1980)]. In the shallow water landward of line A, linear long wave theory yields:

$$\begin{aligned} u_t &= \eta_t (g/h)^{0.5}, \\ S_u &= S_\eta (g/h) \end{aligned} \tag{2.1}$$

where $u_t = (u\text{-}\overline{u})$, $\eta_t = (\eta\text{-}\overline{\eta})$, the subscript t denotes the time-varying components, g is the gravitational acceleration and h is the mean water depth. The spectra S_u and S_η at the same line with the measured h are related linearly according to (2.1). The six spectra of S_u at line D deviated significantly from this linear relationship in the frequency range 0.1-0.3 Hz possible because line D was the transition from breaking waves to bores.

2.3.3 Alongshore Velocities

The time series of the alongshore velocities v_1 and v_2 measured by the 3D ADV and 2D ADV fluctuated rapidly and appeared to be noises. In the fixed-bed experiment by Kobayashi *et al.* (1998), the intermittent high fluctuations of the

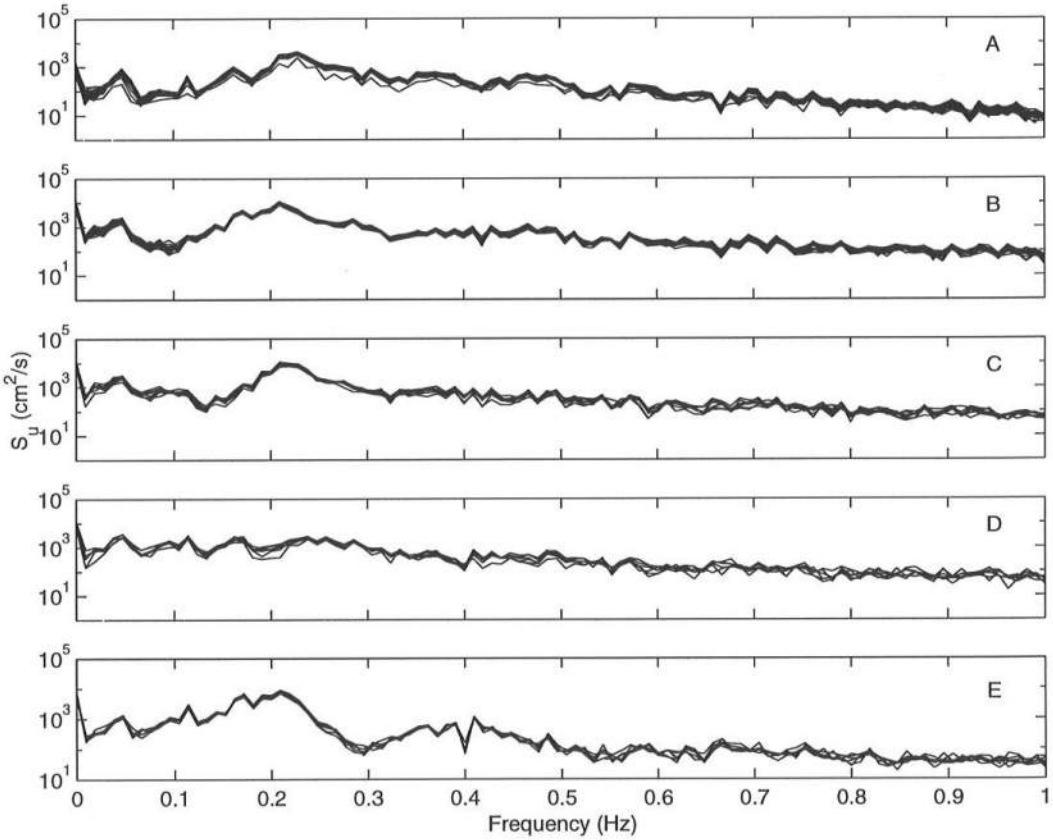

Figure 2.21: Horizontal Velocity Frequency Spectra

measured alongshore velocity v did not appear to be related to the time series of the corresponding η and u which were dominated by the oscillatory wave motions. The measurements of the sand concentration C in this experiment allow us to compare the time series of v and C.

Table 2.10 lists the vertically averaged values of the mean, standard deviation and skewness of v_1 and v_2 at lines A–E shown in Figure 2.2. The mean $\overline{v}_1$ and $\overline{v}_2$ were practically zero in light of the measurement errors on the order of 1 cm/s or less. No flux boundary conditions on the side walls require zero mean in the absence of a secondary circulation in the plane normal to the cross-shore coordinate x. The standard deviation σ_v for both v_1 and v_2 varied little vertically except for tests A3–A5 for which the values of σ_v were approximately twice the average values of σ_v at line A listed in Table 2.10. The region at a distance of 3-5 cm above the bed was observed to be influenced be vortices ejected from the ripples at line A. The skewness was relatively small where the skewness is zero for Gaussian noises. The measured time series were indeed affected by noises but the measured values of σ_v for both v_1 and v_2 at line B–E inside the surf zone were definitely larger than the noise level and about 20% of σ_u listed in Table 2.9.

Table 2.10: Statistics of Alongshore Velocities

	Mean (cm/s)		σ_v (cm/s)		*skew*	
Line	v_1	v_2	v_1	v_2	v_1	v_2
A	-0.08	0.21	2.2	1.7	0.09	0.12
B	0.04	0.07	4.6	3.1	0.02	0.69
C	-0.05	0.29	6.0	5.3	0.20	-0.32
D	-0.40	-0.29	6.9	6.2	0.03	-0.05
E	0.06	0.24	5.9	4.8	0.21	-0.04

The spectrum S_v of the alongshore velocity is normalized as $S_v^* = S_v/\sigma_v^2$ using the values of σ_v corresponding to the specific time series of v to account for

the difference of σ_v for v_1 and v_2. Figure 2.22 shows the normalized spectra S_v^* for both v_1 and v_2 at lines A–E. The peaks of S_v^* in the vicinity of the peak frequency $f_p = 0.21$ Hz for S_η at line A may be related to the ejection of vortices from the ripples where the shoaling waves at line A were nonlinear and the vortex ejection may not have occurred twice per wave. The peaks of S_v^* near the frequency 0.21 Hz disappeared in the surf zone. The spectra S_v^* in the surf zone increased with the decrease of the frequency and were dominated by the components with frequencies less than about 0.1 Hz. These components are not low frequency waves because the flume width was 115 cm and no cross-flume waves were observed. The low frequency components of v are related to the intermittent intense fluctuations of v. These components may also be present in the spectra S_u but are difficult to detect because the cross-shore velocity u is dominated by the wave motions.

2.3.4 Vertical Velocities

The vertical velocity measured by the 3D ADV consisted of the wave and turbulent components. To detect the wave component at least qualitatively, use may be made of the following relationships obtained using linear long wave theory [e.g., Dean and Dalrymple (1984)]:

$$\begin{aligned} w_t &= \frac{z+d}{h}\left(\frac{h}{g}\right)^{0.5}\frac{\partial u_t}{\partial t}, \\ w_t &= -\frac{z+d}{h}(gh)^{0.5}\frac{\partial \eta_t}{\partial x} \end{aligned} \tag{2.2}$$

where $w_t = (w - \overline{w})$, z is the vertical coordinate with $z = 0$ at SWL, d is the still water depth, h is the mean water depth given by $h = (d + \overline{\eta})$ including the wave setup $\overline{\eta}$ and t is time. The vertical velocity w of linear long waves increases linearly upward with $w = 0$ at $z = -d$ and is proportional positively to the fluid acceleration and negatively to the free surface slope. Elgar *et al.* (1988, 2001) discussed the importance of skewed fluid accelerations associated with steep front faces for cross-shore sediment transport. Kobayashi and Johnson (2001) predicted

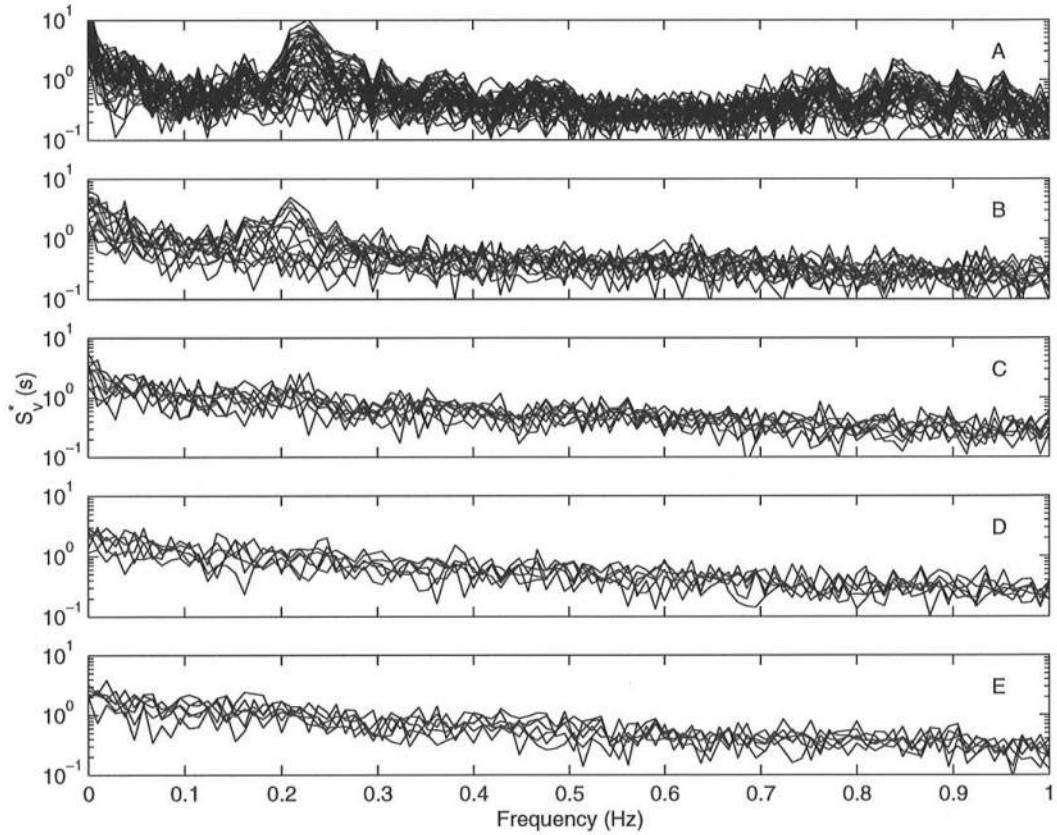

Figure 2.22: Normalized Alongshore Velocity Frequency Spectra

intense sediment suspension near the steep wave fronts numerically. The measured vertical velocity may hence be regarded as a proxy for the fluid acceleration and free surface slope.

Table 2.11 lists the vertically averaged values of the mean, standard deviation and skewness of w at lines A–E. The mean $\overline{w}$ varied little vertically except at line A where $\overline{w}$ was about -0.5 cm/s at a distance 1-5 cm above the bottom and approached zero above the region affected by vortices ejected from the ripples. The mean $\overline{w}$ was approximately -0.9 cm/s at lines B–E. The measured vertical velocity was the vertical velocity of the particulate matters in the sampling volume of 0.1 cm^3 with the estimated errors on the order of 0.2 cm/s or less. The measured fall velocity w_f of sand particles in quiet water was 2.0 cm/s. The measured vertical velocity w seems to correspond to the fluid velocity in the region of very small sand concentrations and an intermediate velocity between the fluid and sand velocities in the region of high sand concentrations. It is also possible that the turbulent shear flow may have reduced the sand fall velocity in light of the two-phase flow analysis by Kobayashi and Seo (1985) for steady uniform flow. On the other hand, the standard deviation σ_w increased upward at all lines A–E due to the upward increase of the wave-induced vertical velocity as implied by (2.2). However, σ_w was about 2 cm/s at 1 cm above the bottom and did not approach zero due to the turbulent vertical velocity. The skewness of w also increased upward except at line E where the skewness was about -1.0 possibly due to the effect of down-rush from the swash zone.

Figure 2.23 shows the normalized spectra $S_w^* = S_w/\sigma_w^2$ for w at lines A–E where the spectrum S_w and σ_w were obtained from the same time series of w. The peaks of S_w^* near the frequency 0.21 Hz corresponding to the peaks of S_η in Figure 2.19 are mostly related to the wave motions. The spectral components related to vortices and turbulence are not very apparent unlike S_v^* shown in Figure 2.22 where the alongshore velocity v does not contain any wave motion. The reason for

the increase of S_w^* in the very low frequency less than 0.01 Hz is not clear but may be related to intermittent high sand concentrations where clouds of sand particles were observed to be intermittently advected seaward from inside the surf zone.

Table 2.11: Statistics of Vertical Velocities

Line	$\overline{w}$ (cm/s)	σ_w (cm/s)	*skew*
A	-0.28	2.2	0.85
B	-0.91	2.7	2.24
C	-0.94	2.9	0.44
D	-0.81	3.3	0.22
E	-0.84	3.2	-1.00

2.3.5 Sand Concentrations

The sand concentrations C_1 and C_2 were measured by sensors 1 and 2 separated 9 cm alongshore as shown in Figure 2.3. Table 2.12 lists the vertically averaged values of the mean, standard deviation and skewness of C_1 and C_2 at lines A–E where the sand concentration is expressed in terms of the sand mass in grams divided by the mixture volume in liters. The differences in the standard deviation σ_C and skewness of C_1 and C_2 are related to the time-varying components of C_1 and C_2 with estimated errors of about 20%. The mean concentration $\overline{C}$ and σ_C for both C_1 and C_2 decreased upward rapidly at line A outside the surf zone and slowly at lines B–E inside the surf zone. The values of $\overline{C}$ and σ_C were on the same order of magnitude at all locations. At line A, $\overline{C}$ and σ_C were about 3 g/L in the region affected by the ripples, less than 1 g/L at 5 cm from the bottom and 0.2 g/L at 20 cm from the bottom. At lines B–E, $\overline{C}$ and σ_C were consistent with the visually observed intensity of wave breaking which was the maximum at line C and reduced

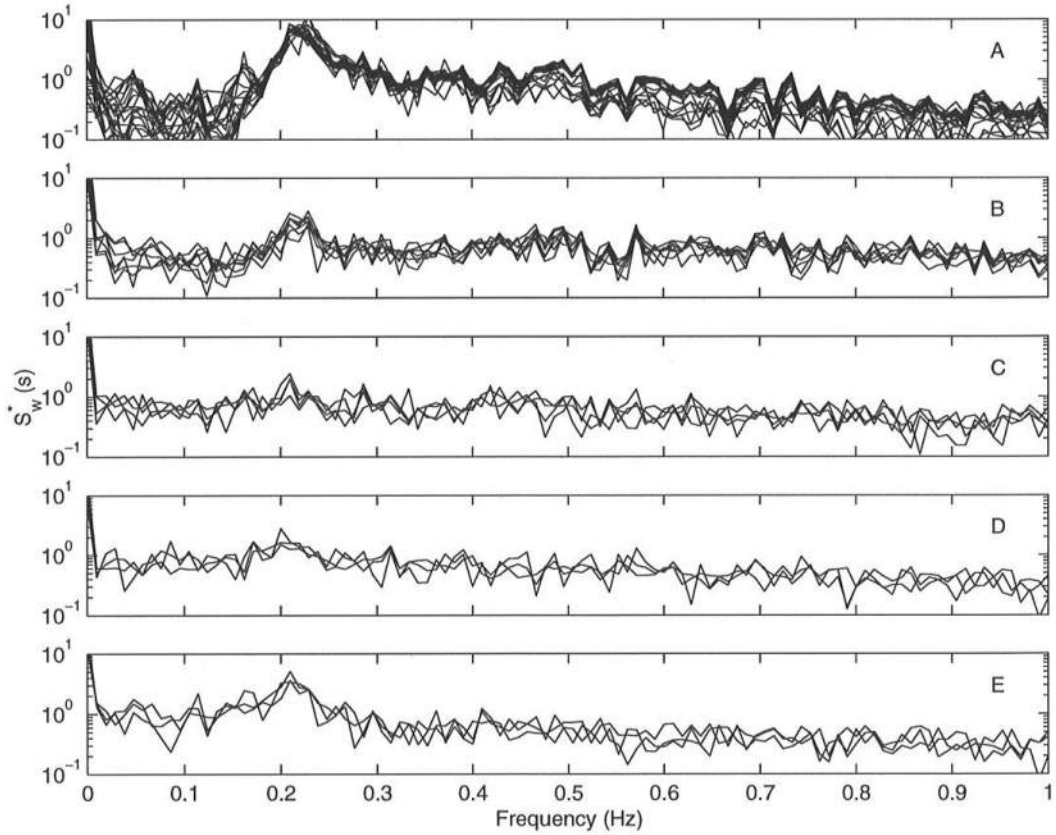

Figure 2.23: Normalized Vertical Velocity Frequency Spectra

noticeably under bores at line A. On the other hand, the skewness for C_1 and C_2 was large due to intermittent high concentrations.

Figure 2.24 shows the normalized spectra $S_C^* = S_C/\sigma_C^2$ for both C_1 and C_2 at lines A–E where the spectrum S_C and σ_C were obtained from the same concentration measurement. The normalized spectra S_C^* were dominated by the low frequency components in the frequency range less than about 0.1 Hz. The secondary peak of S_C^* near 0.21 Hz was detectable at lines A–C. The spectra S_C^* increased with the decrease of the frequency f for $f < 0.1$ Hz more rapidly than the spectra S_v^* shown in Figure 2.22. This suggests that the sand concentration C responds to vortices and turbulence in more amplified manners than the alongshore velocity v.

Table 2.12: Statistics of Sand Concentrations

	Mean (g/L)		σ_C (g/L)		*skew*	
Line	C_1	C_2	C_1	C_2	C_1	C_2
A	0.7	0.9	1.1	1.7	9.2	11.0
B	2.8	2.8	4.7	5.2	5.2	4.6
C	4.7	4.6	4.9	6.7	2.1	4.8
D	3.1	3.4	3.9	6.1	3.1	6.2
E	1.6	1.4	2.5	2.6	4.7	7.8

2.4 Sand Suspension Events

The time series of all the measured quantities were examined to identify intermittent suspension events and infer possible mechanisms for such events qualitatively. These events were repeatable for the same irregular waves and not random. The time series lasting a duration of 900 s were obtained for each line A–E. For simplicity, the times series of the cross-shore velocities u_1 and u_2, which were in phase as shown in Figure 2.25 for test B2, were averaged to obtain the times series of $u = (u_1 + u_2)/2$ for each test. Likewise, the times series of the concentrations C_1 and

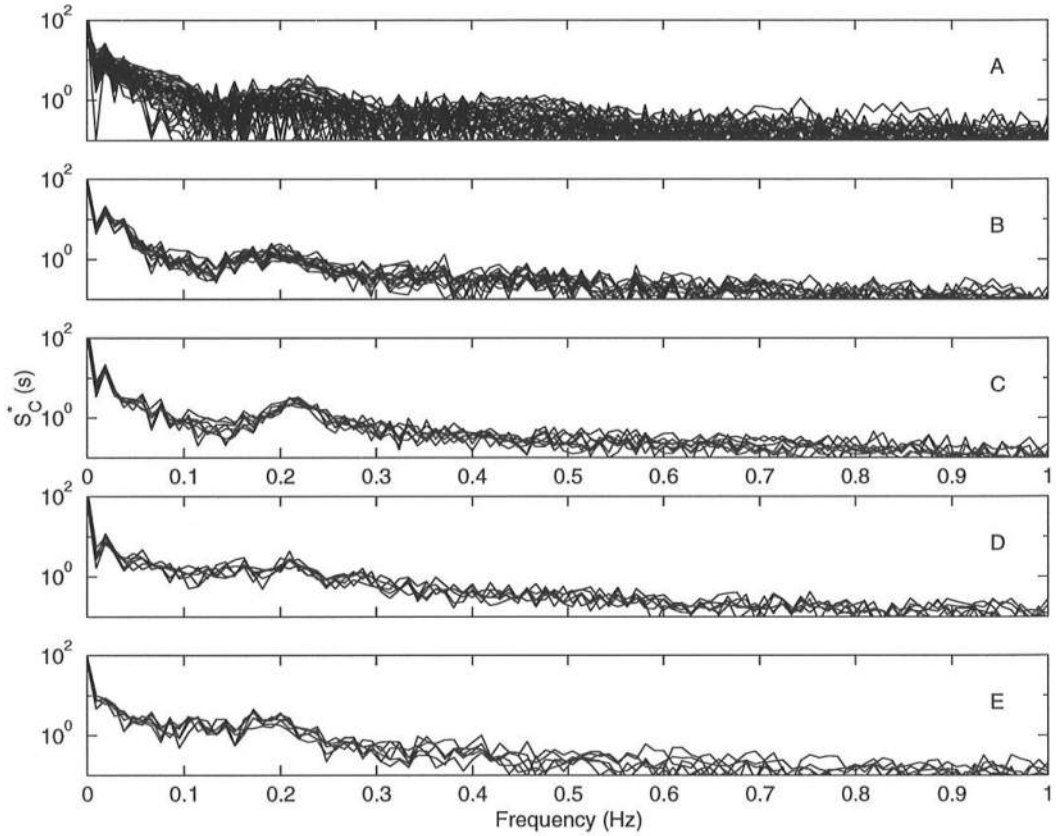

Figure 2.24: Normalized Suspended Sediment Concentration Frequency Spectra

C_2 were averaged to obtain the time series of $C = (C_1 + C_2)/2$. The concentrations C_1 and C_2 were not always in phase, but intermittent high concentration events occurred simultaneously in both time series as shown in Figure 2.25. Figure 2.25 also illustrates that the time series of the alongshore velocities v_1 and v_2 fluctuated rapidly and their phase relationship appeared to be random. Therefore, the time series of the absolute alongshore velocity $|v| = [(v_1^2 + v_2^2)/2]^{0.5}$ was used to represent the magnitude of the alongshore velocity. The time series of the free surface elevation η and the vertical velocity w from the same test were plotted without any averaging.

The time series of η, u, $|v|$, w and C during the time t = 600-660 s for each of the 37 tests are plotted in the following subsections as Figures 2.26, 2.27, 2.28, 2.29 and 2.30 for lines A, B, C, D and E, respectively. The physical interpretation of the measured concentrations inside the surf zone is difficult because the sand particles were observed to be suspended higher in the water column almost instantaneously and advected horizontally during their slow settling downward as assumed in the numerical model by Kobayashi and Johnson (2001). Table 2.13 gives a concise report of the visual observations made of wave breaking and sediment suspension events at each of the locations A–E. In the breaker type column, P denotes a plunging breaker, S denotes a spilling breaker and SP denotes an intermediate breaker between plunging and spilling breakers. In these observations it was found that the suspension events did not always coincide with local breaking waves. This occurred more frequently at lines D and E where most of the sediment suspension events were advected from further offshore or created by the turbulent bores resulting from the waves that broke further offshore.

Table 2.13: Record of Breaking Waves and Suspension Events at Locations A–E

A			B			C			D			E		
Wave Brk		Susp	Wave Brk		Susp	Wave Brk		Susp	Wave Brk		Susp	Wave Brk		Susp
t (s)	type	t (s)	t (s)	type	t (s)	t (s)	type	t (s)	t (s)	type	t (s)	t (s)	type	t (s)
no breakers					28			25			25			26
					33	68	P		61	S				91
					68			69	64	S		98	S	
					92	89	SP				65	139	S	
		300			97	93	P				69	149	S	
		352	101	S				94	114	S				245
		560			103	141	S		129	S				268
					151	157	SP		137	SP		286	S	
					195	161	P				158			288
					204	165	P				183			310
					208			166			197			349
					247	181	SP		220	SP				369
			274	S	274	195	P				246			377
					289			196	260	S				407
			293	P	293	200	P				267			455
			302	SP	302	204	P				291			463
			341	P		209	P		301	S				503
					342	236	S				340	536	S	
			346	SP	346	244	SP		348	S		543	S	
					370			247	376	S				546
			376	SP		252	S				403			576
			408	S	408	265	SP		453	S				606
					412	270	SP				462			665
			413	S				273	475	S		674	S	
			455	P	455	290	P				508	684	SP	
					463	317	S		521	S		700	S	
			467	P		324	S		531	S		705	SP	
					468	338	P	338	539	S				727
					486	342	P		544	SP		766	SP	
			493	SP		351	SP		560	P		809	S	
					494	366	P				569	818	S	
			566	P		379	P		578	P		873	S	
					567	385	SP		610	S				
					573	400	S		615	SP				
					581	404	P		621	S				
					584			409	627	P				
			594	SP				417	631	SP				
					595	418	S		635	S				
					600	422	SP				643			
			601	SP		426	S		660	S				
			603	P	603	437	S		664	S				
					639	464	P		681	S				
			640	P		479	S				710			
			711	SP	711	486	SP		724	S				
			718	SP				488	738	S				

Table 2.13: Continued

A			B			C			D			E		
Wave Brk		Susp	Wave Brk		Susp	Wave Brk		Susp	Wave Brk		Susp	Wave Brk		Susp
t (s)	type	t (s)	t (s)	type	t (s)	t (s)	type	t (s)	t (s)	type	t (s)	t (s)	type	t (s)
					719	506	SP		749	S				
			740	SP	740	512	S		754	S				
			780	SP		553	SP		758	S				
			783	P	783			554	762	S				
			838	S	838	557	S				771			
			893	SP		563	S		776	SP				
					894	568	P	568	796	SP				
						573	P		799	S				
						582	SP				817			
						584	SP		824	S				
						590	P		826	S				
						615	SP				830			
						640	P		834	S				
								641	845	SP				
						645	P		859	S				
						655	SP		883	S				
						667	S				887			
						675	S							
						687	SP							
						707	P							
								708						
						716	P							
						731	SP							
						736	S							
						745	SP							
						769	SP							
								770						
						790	SP							
						803	S							
								815						
						819	S							
						828	P							
								831						
						843	SP							
						847	S							
						862	S							
						872	SP							
								873						
						889	SP							
								890						
						899	S							

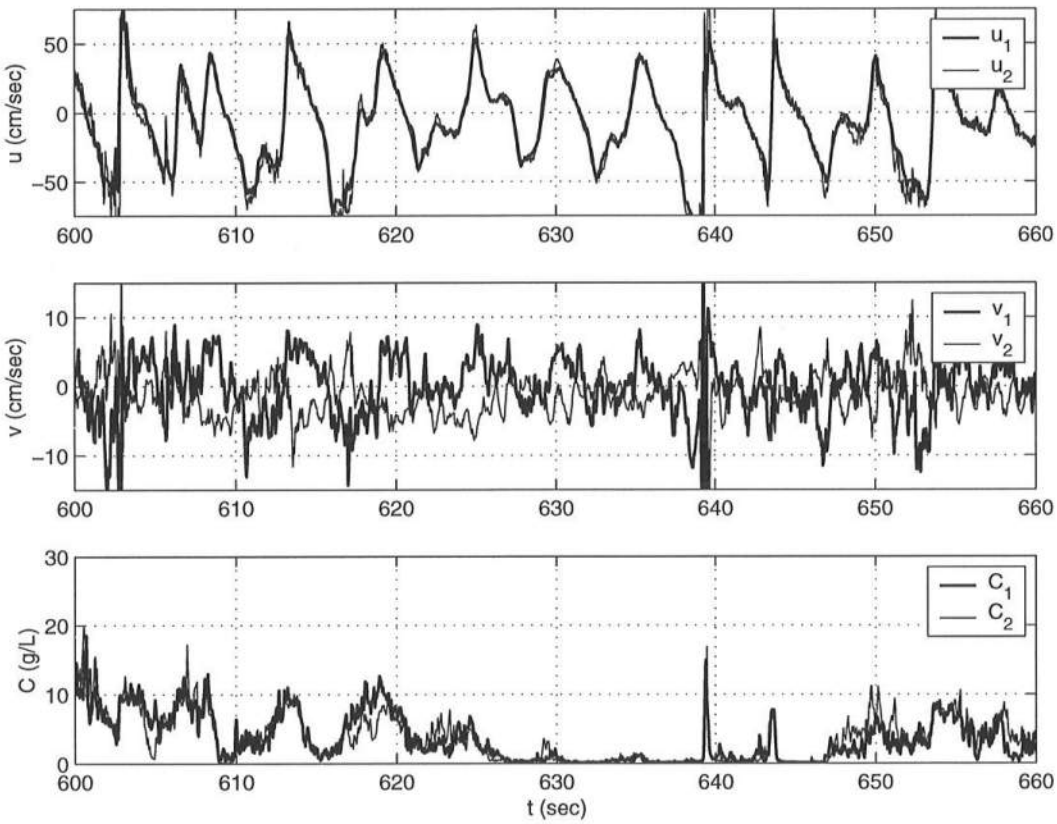

Figure 2.25: Measured Time Series of u_1, u_2, v_1, v_2, C_1 and C_2 for test B2

2.4.1 Line A

Figure 2.26 for Tests A1–A20 shows the times series of the free surface elevation η and the horizontal velocity u of the shoaling irregular waves. The time series of the concentration C indicates several suspension events. Two intense suspension events occurred under the large crest in a wave group with the large onshore velocity. This type of sand suspension was also observed on a natural beach by Hanes (1991). The time series of $|v|$ indicates that these suspension events occur during turbulent events with $|v|$ exceeding approximately 5 cm/s for less than 1 s. The vertical velocity w does not show any clear correlation with C.

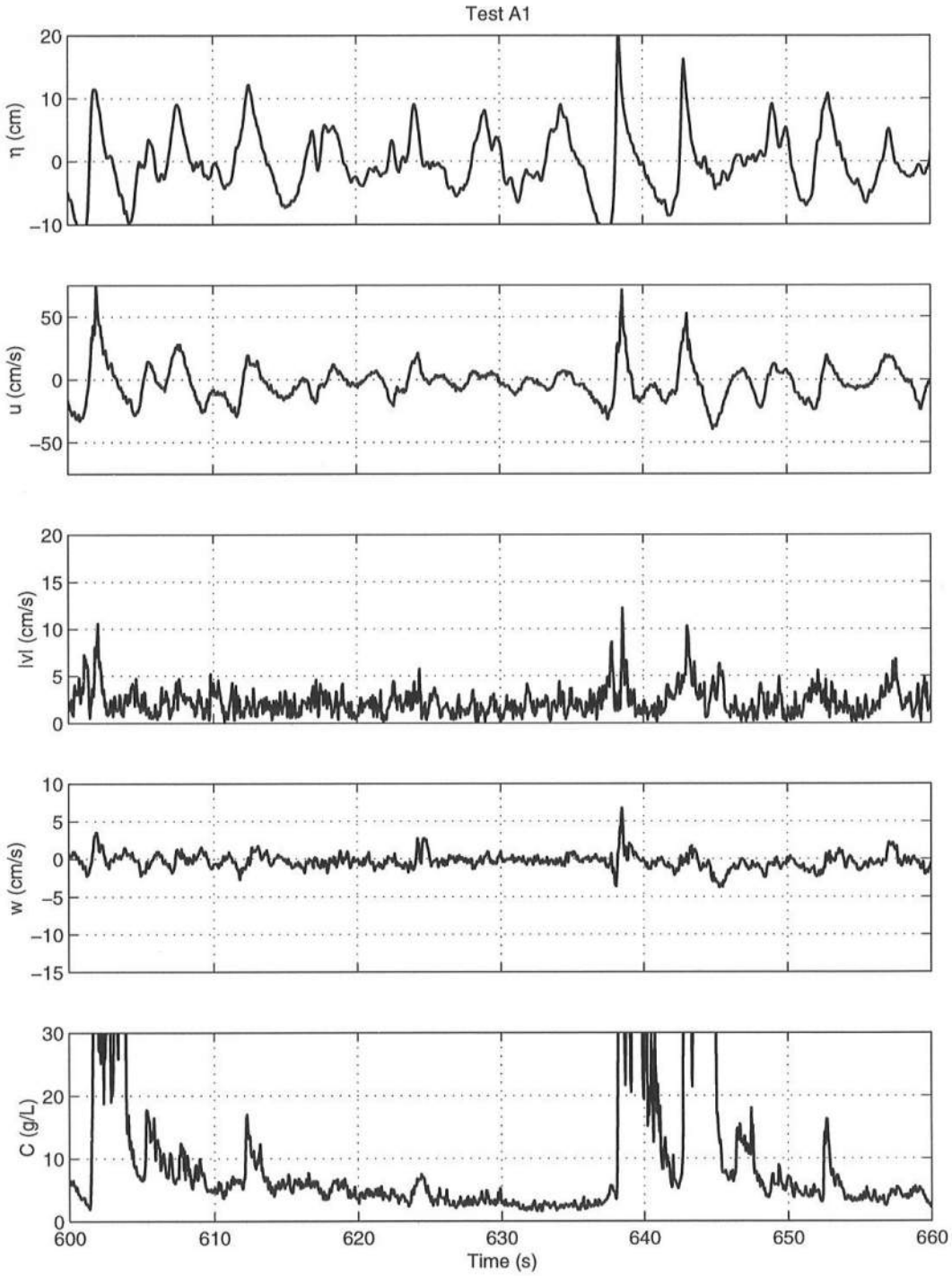

Figure 2.26: Measured Time Series of η, u, $|v|$, w and C for Tests A1–A20

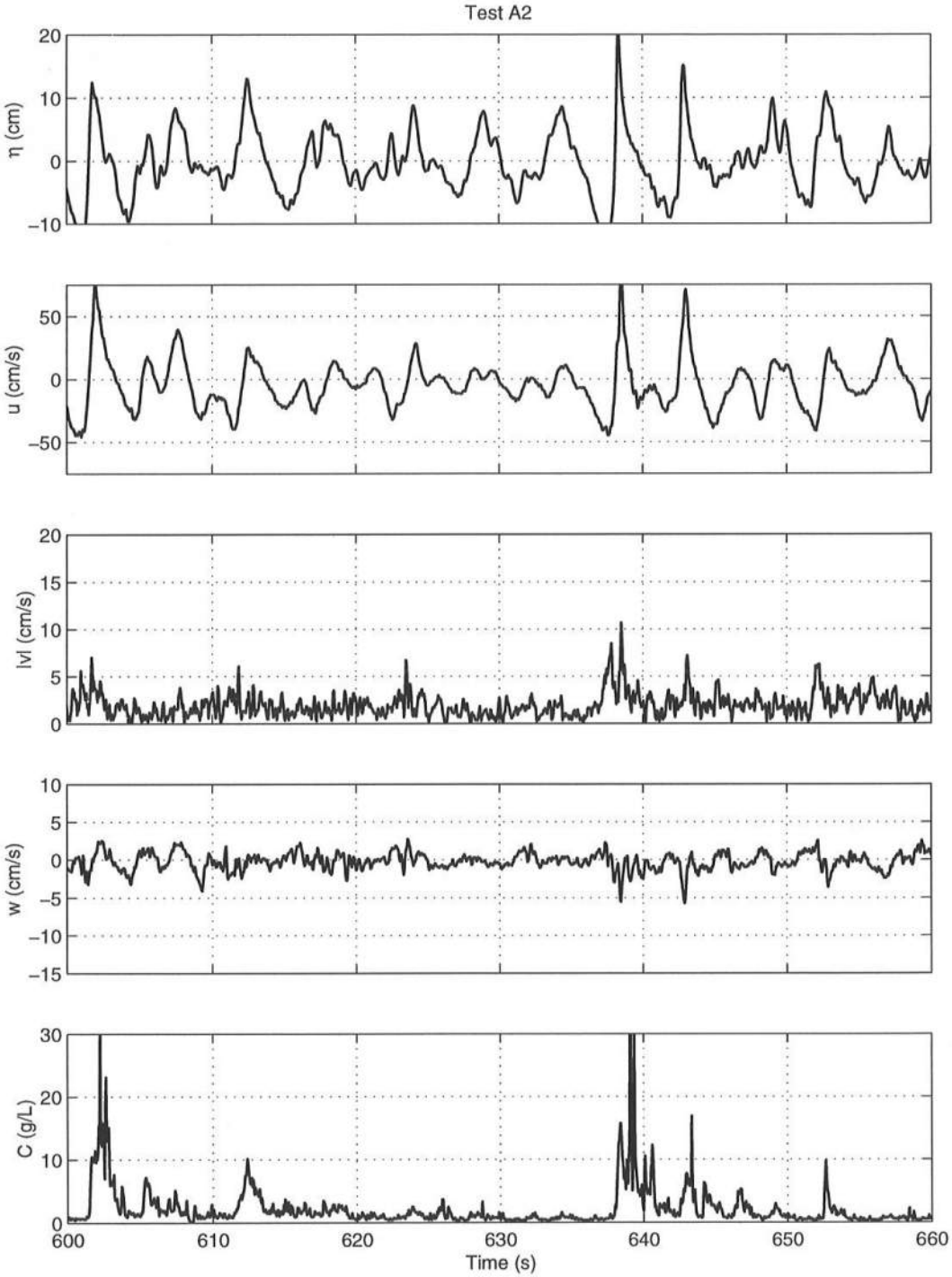

Figure 2.26: Continued

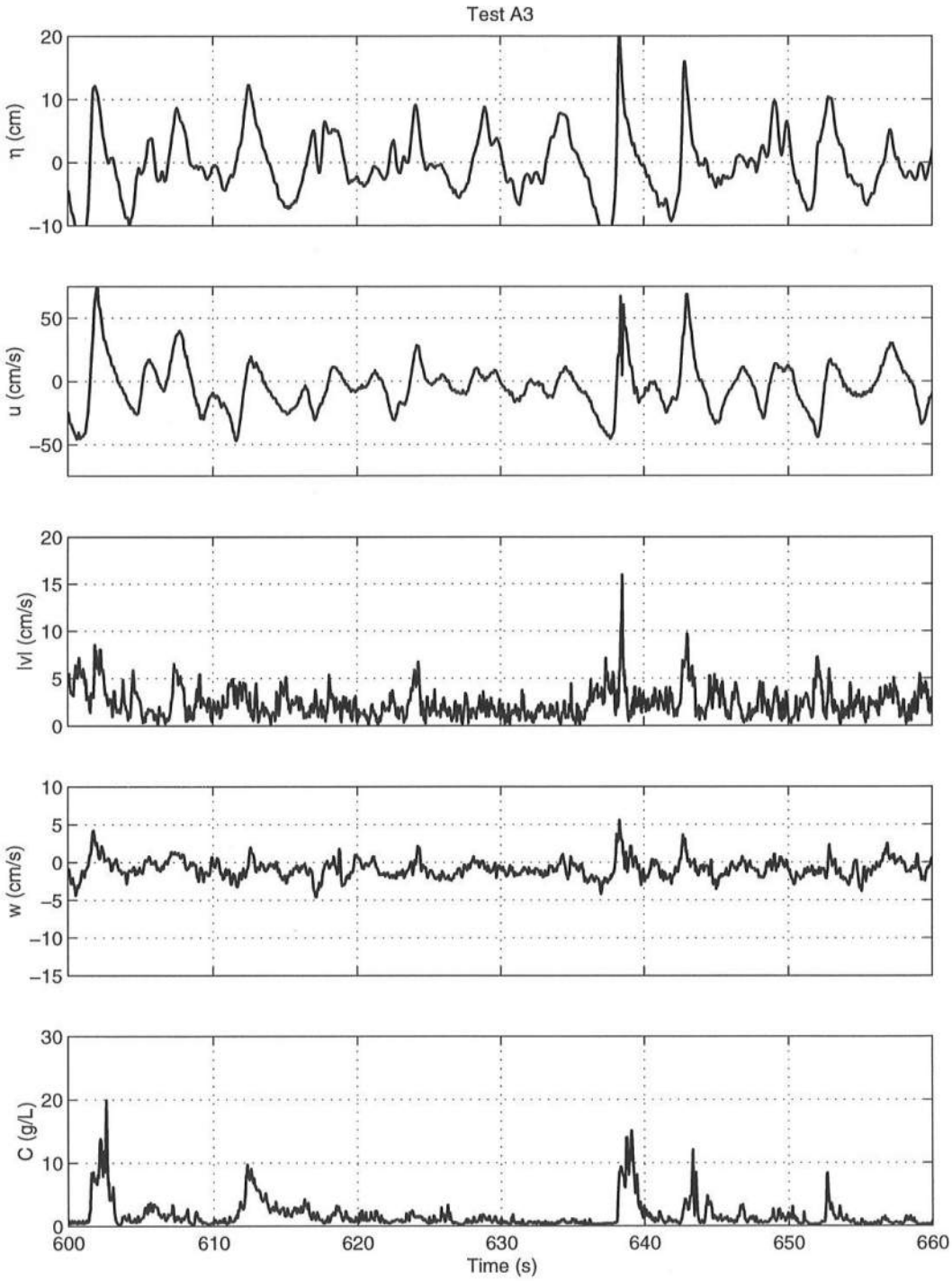

Figure 2.26: Continued

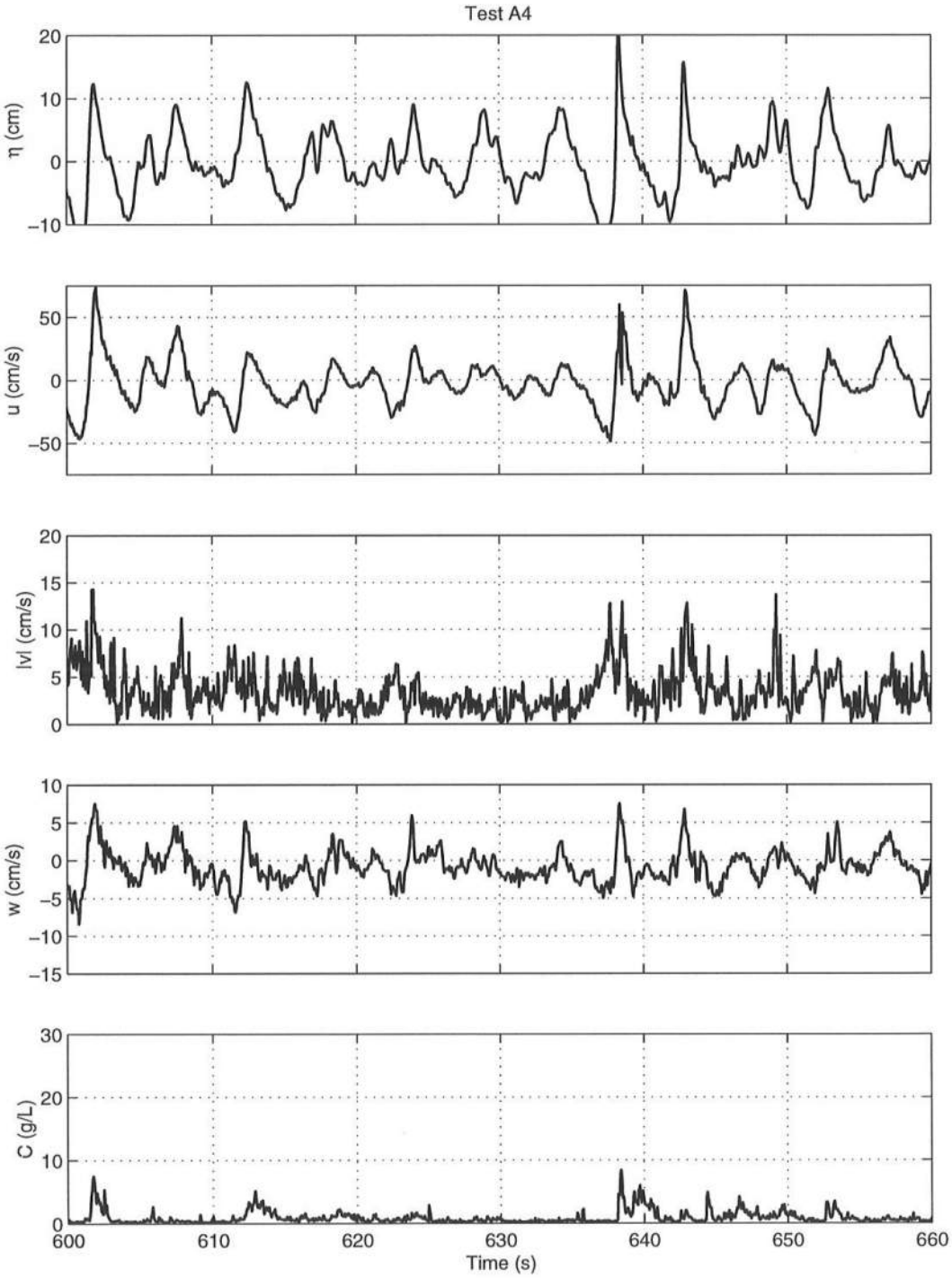

Figure 2.26: Continued

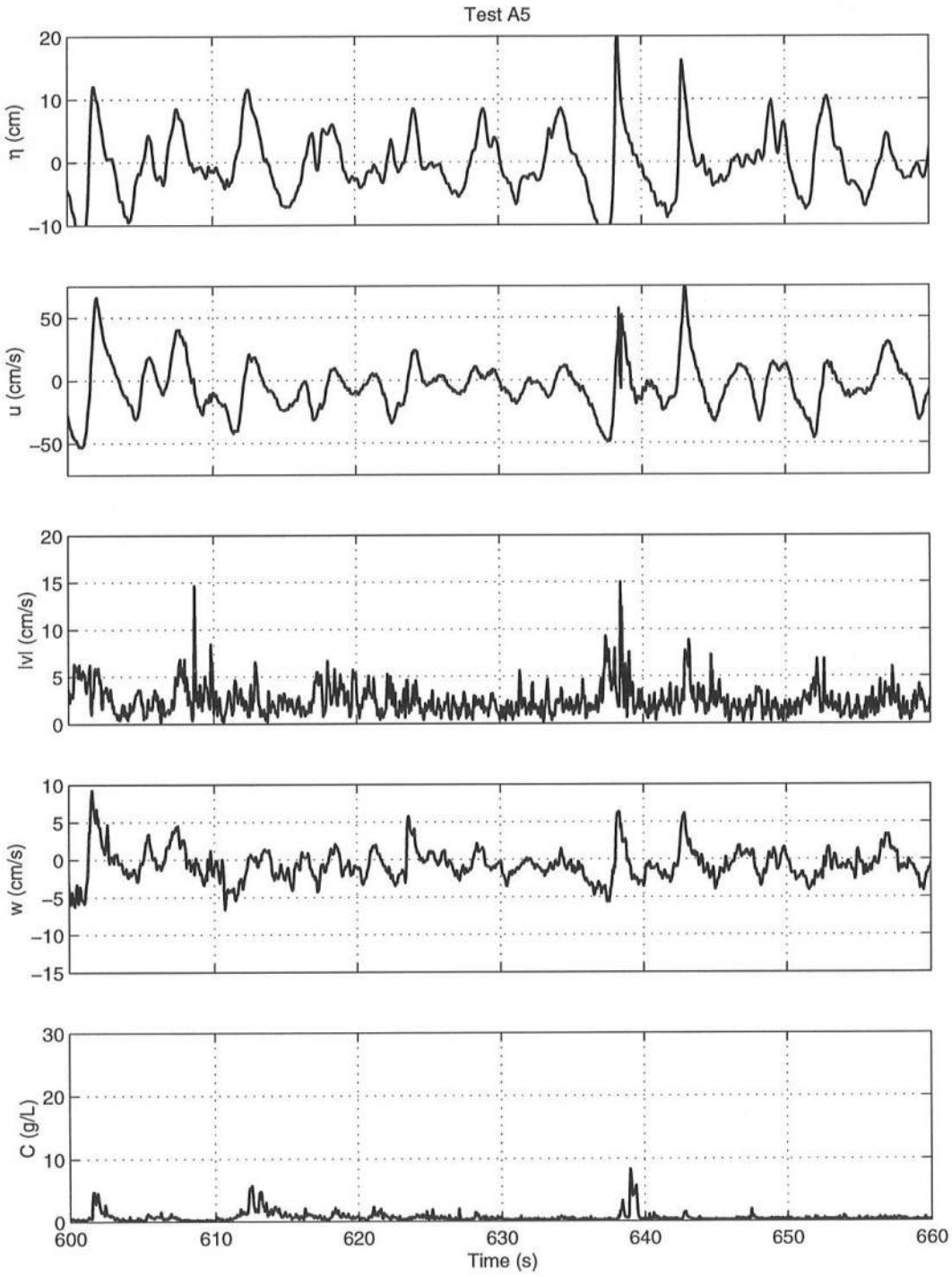

Figure 2.26: Continued

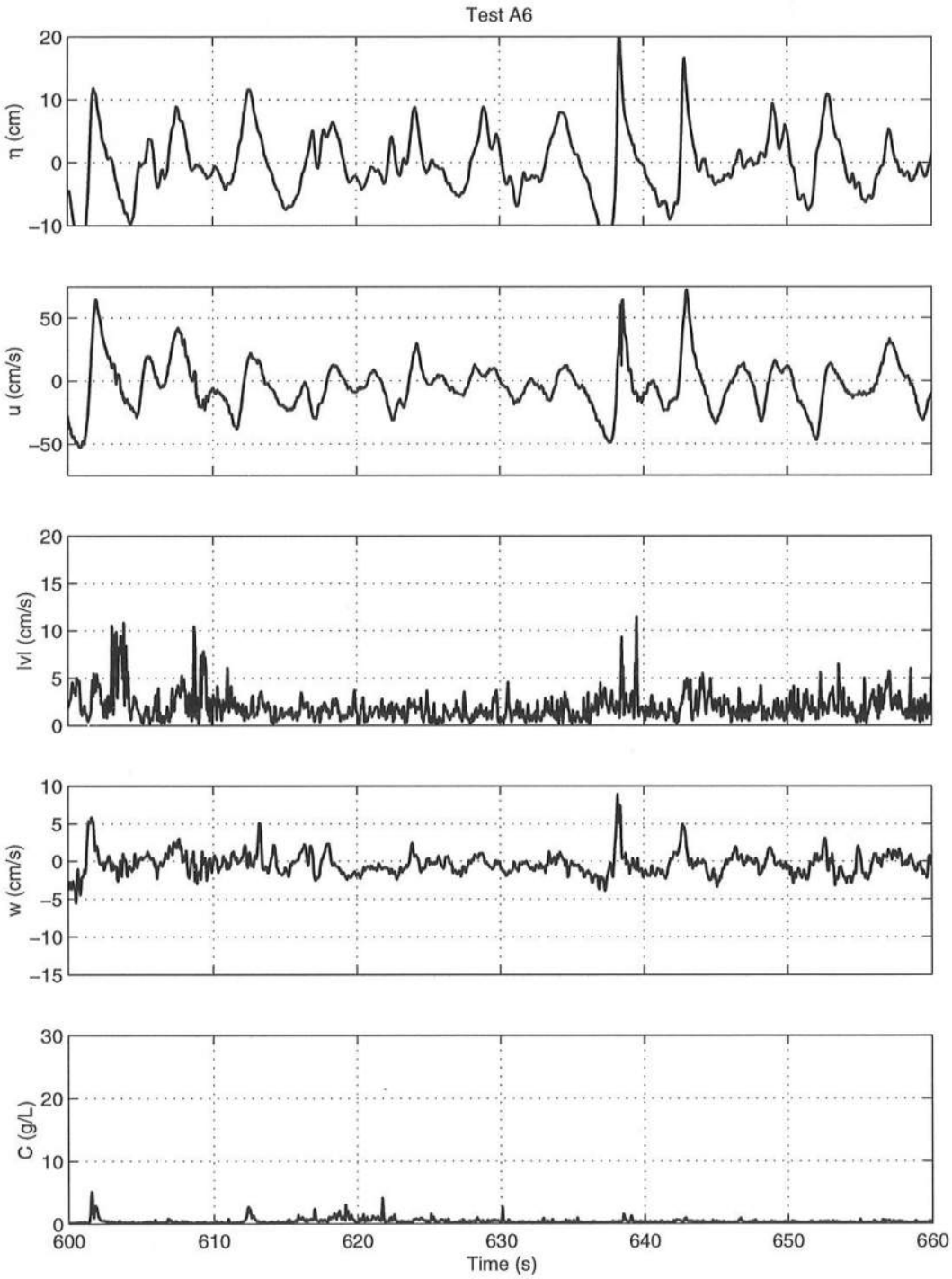

Figure 2.26: Continued

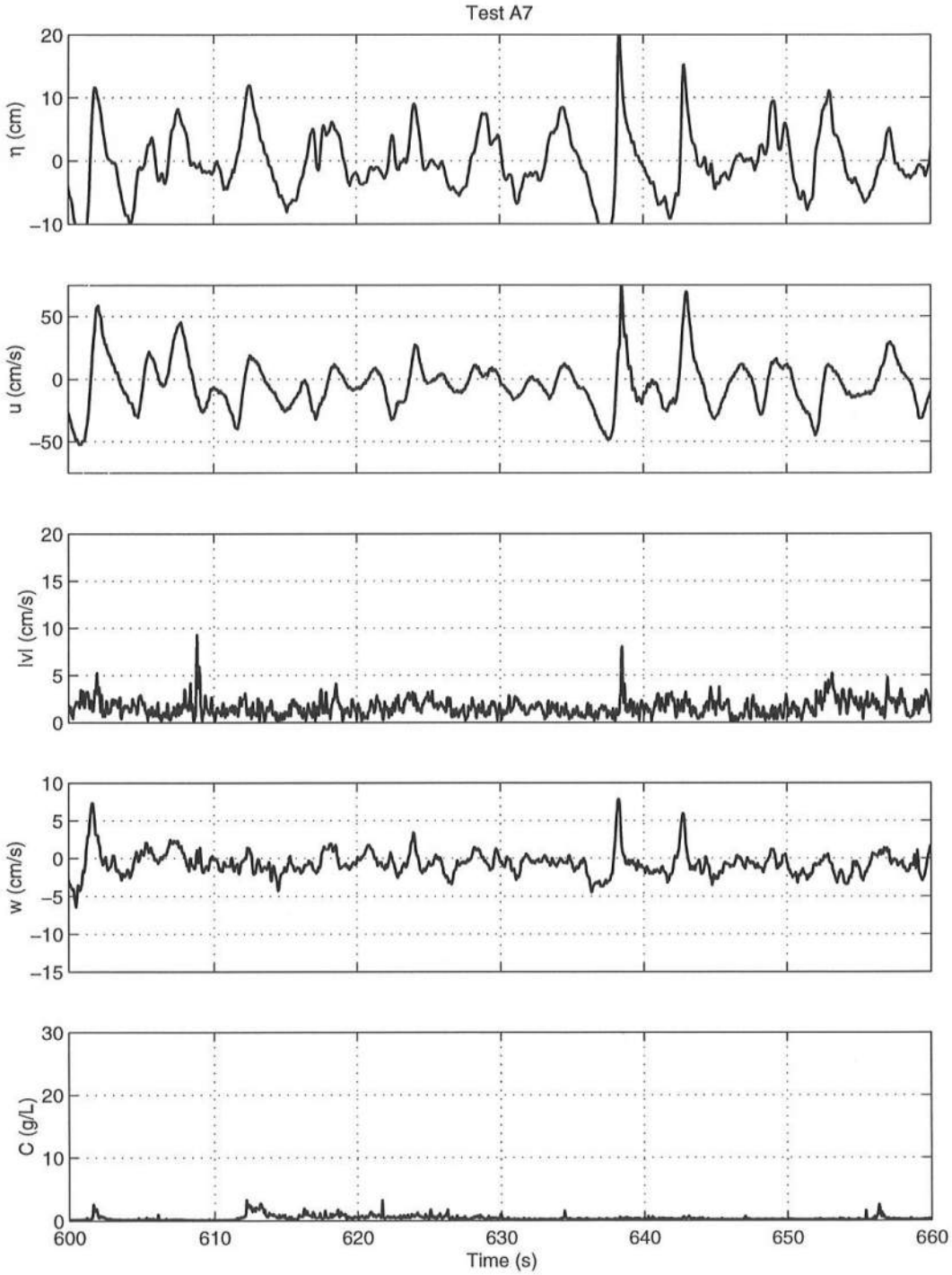

Figure 2.26: Continued

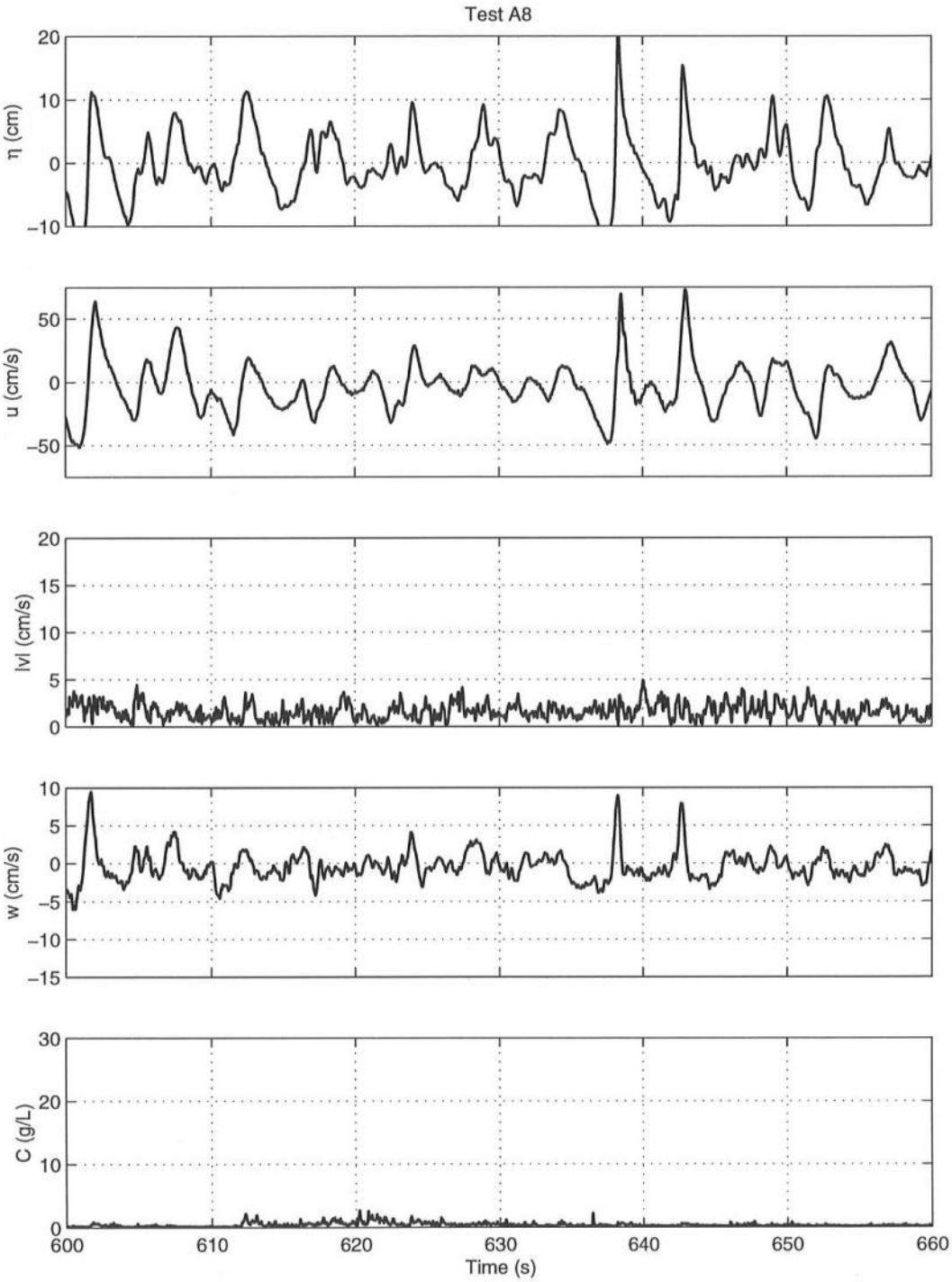

Figure 2.26: Continued

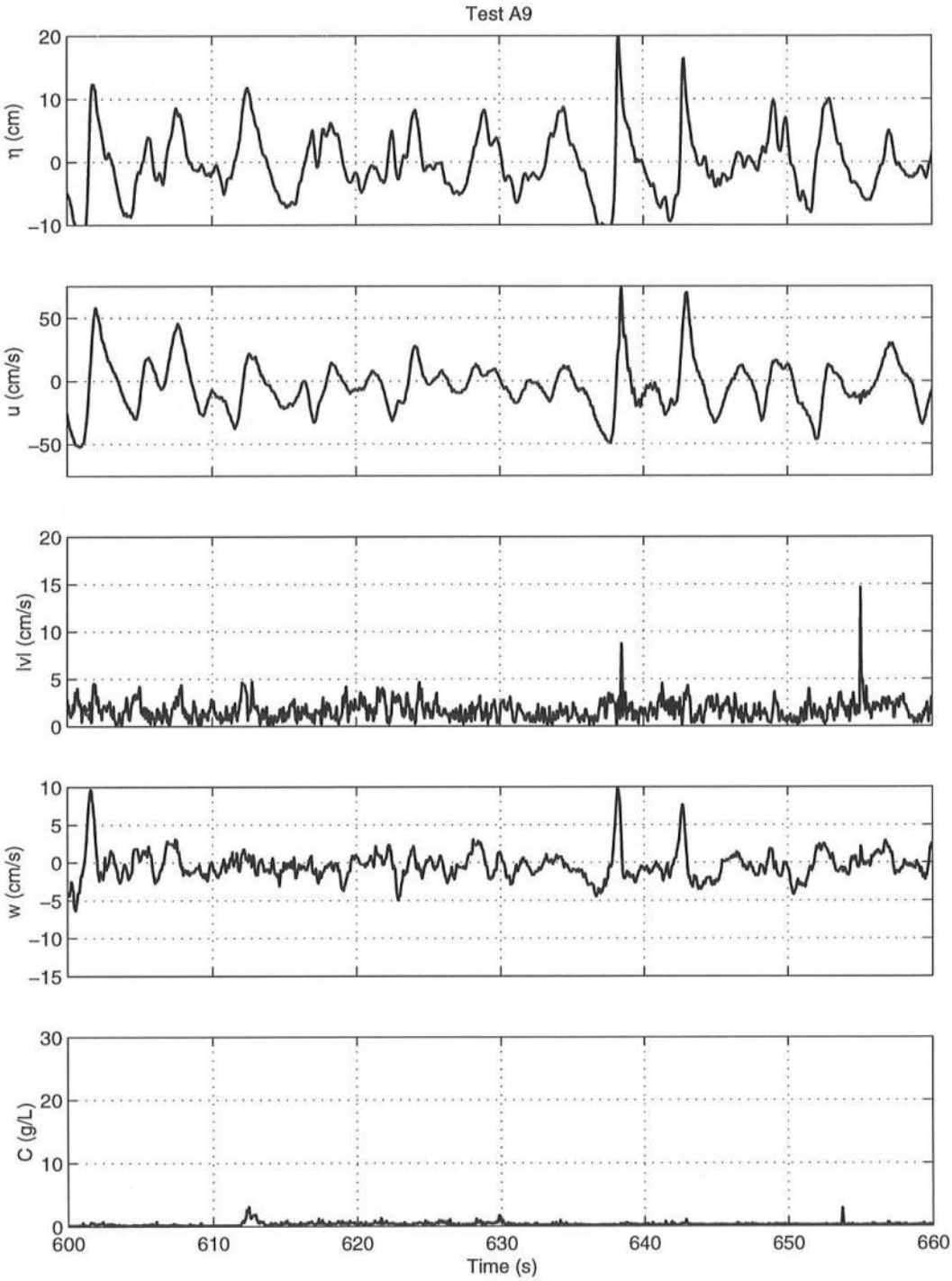

Figure 2.26: Continued

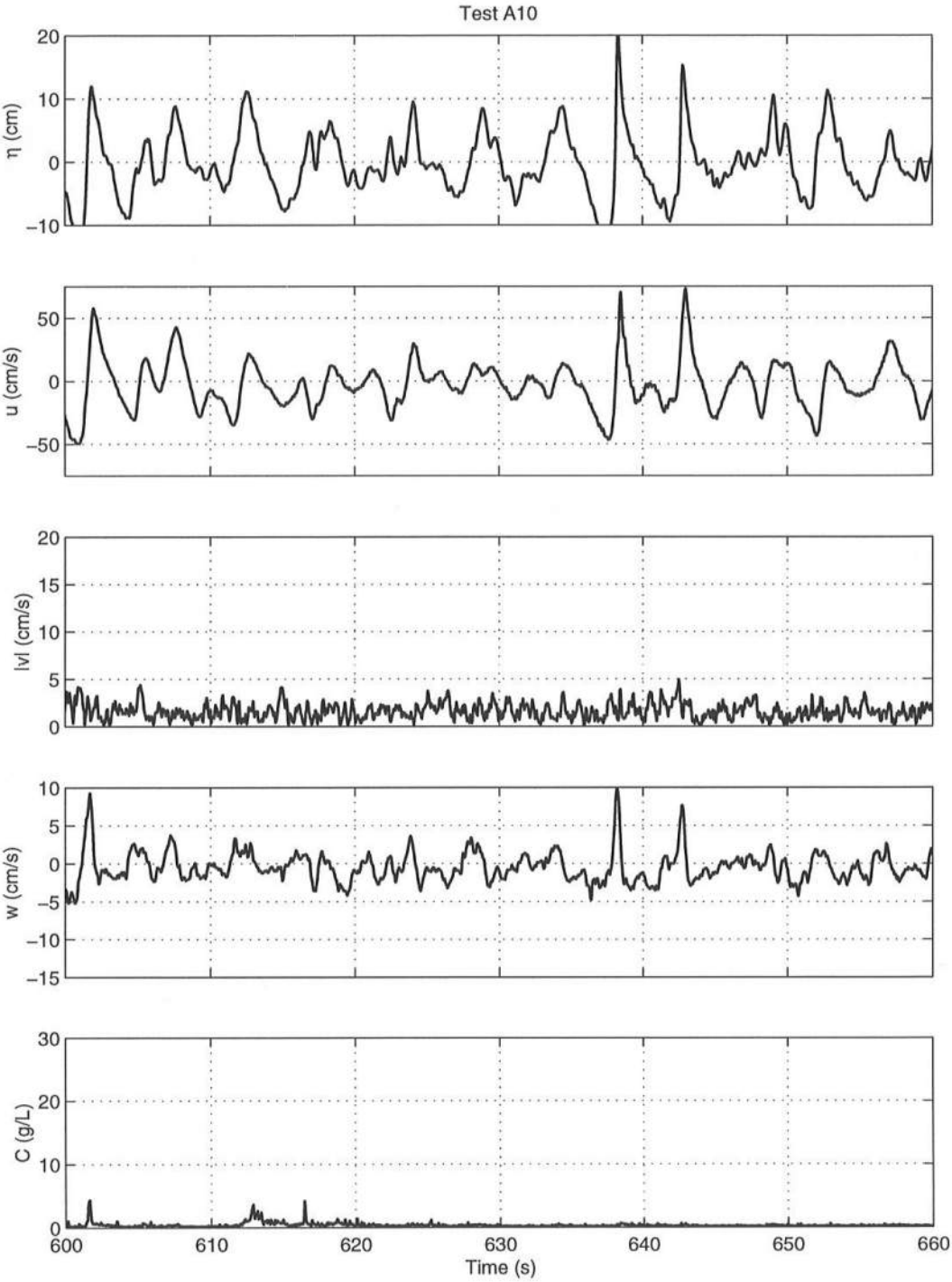

Figure 2.26: Continued

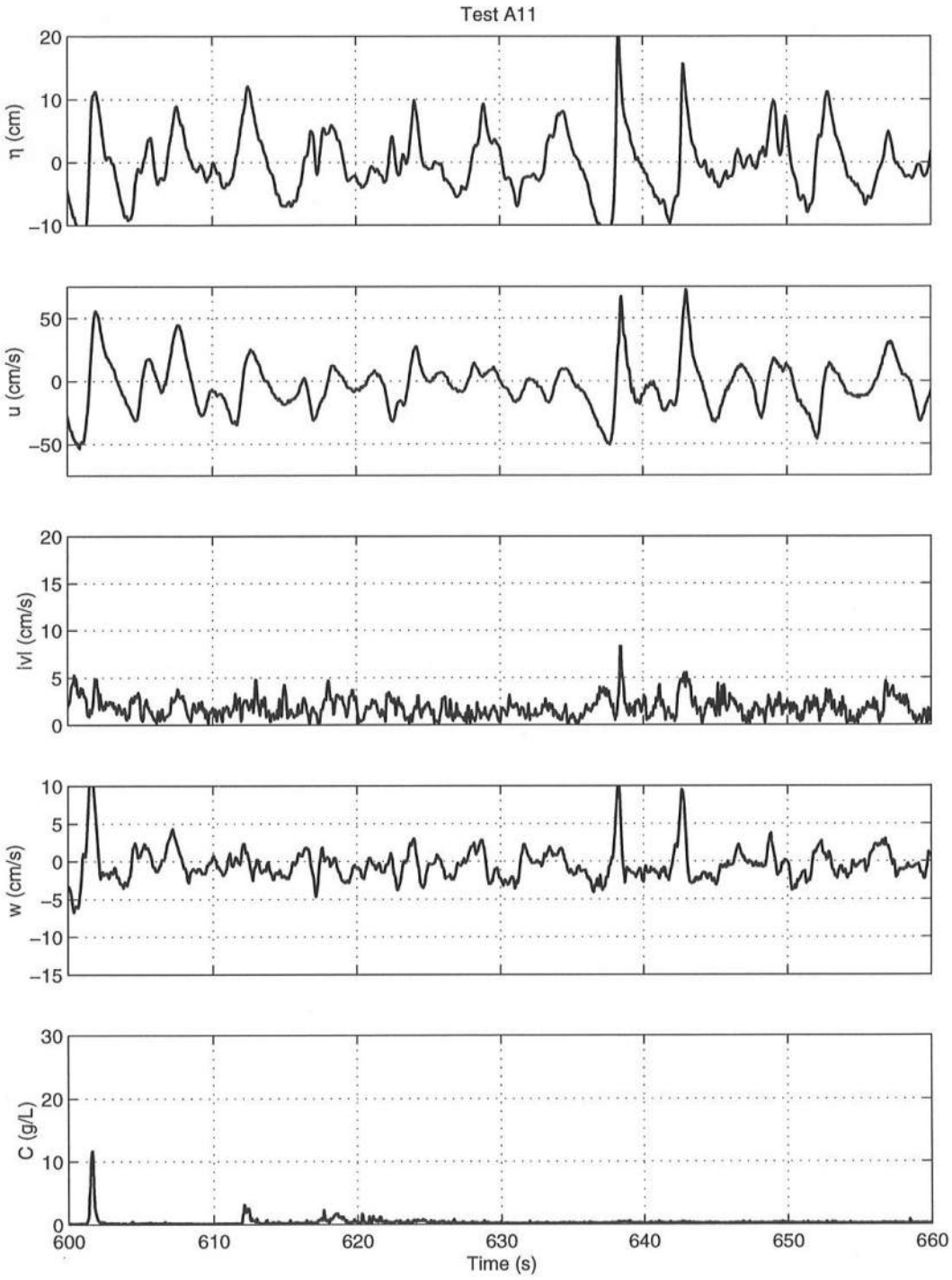

Figure 2.26: Continued

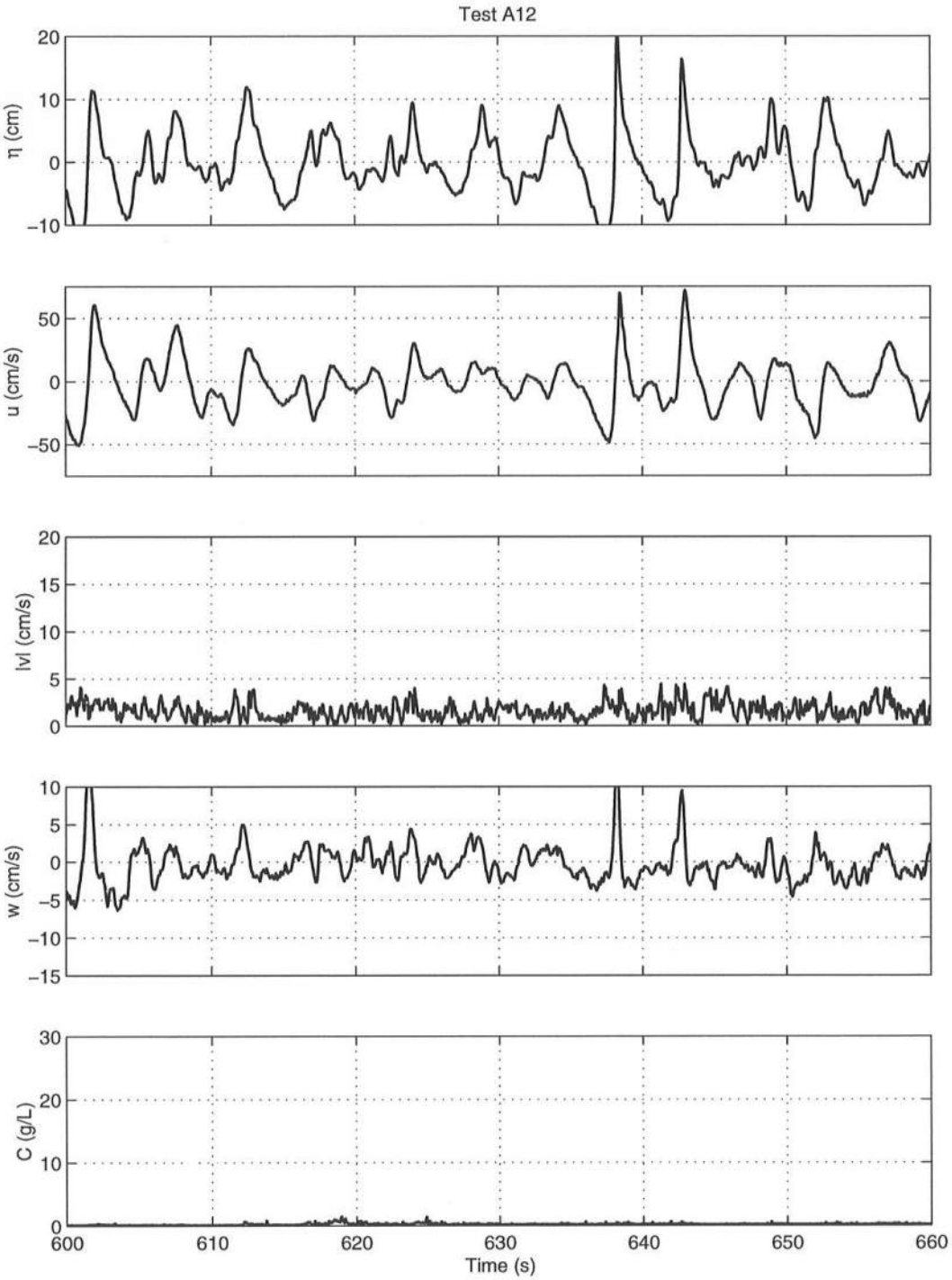

Figure 2.26: Continued

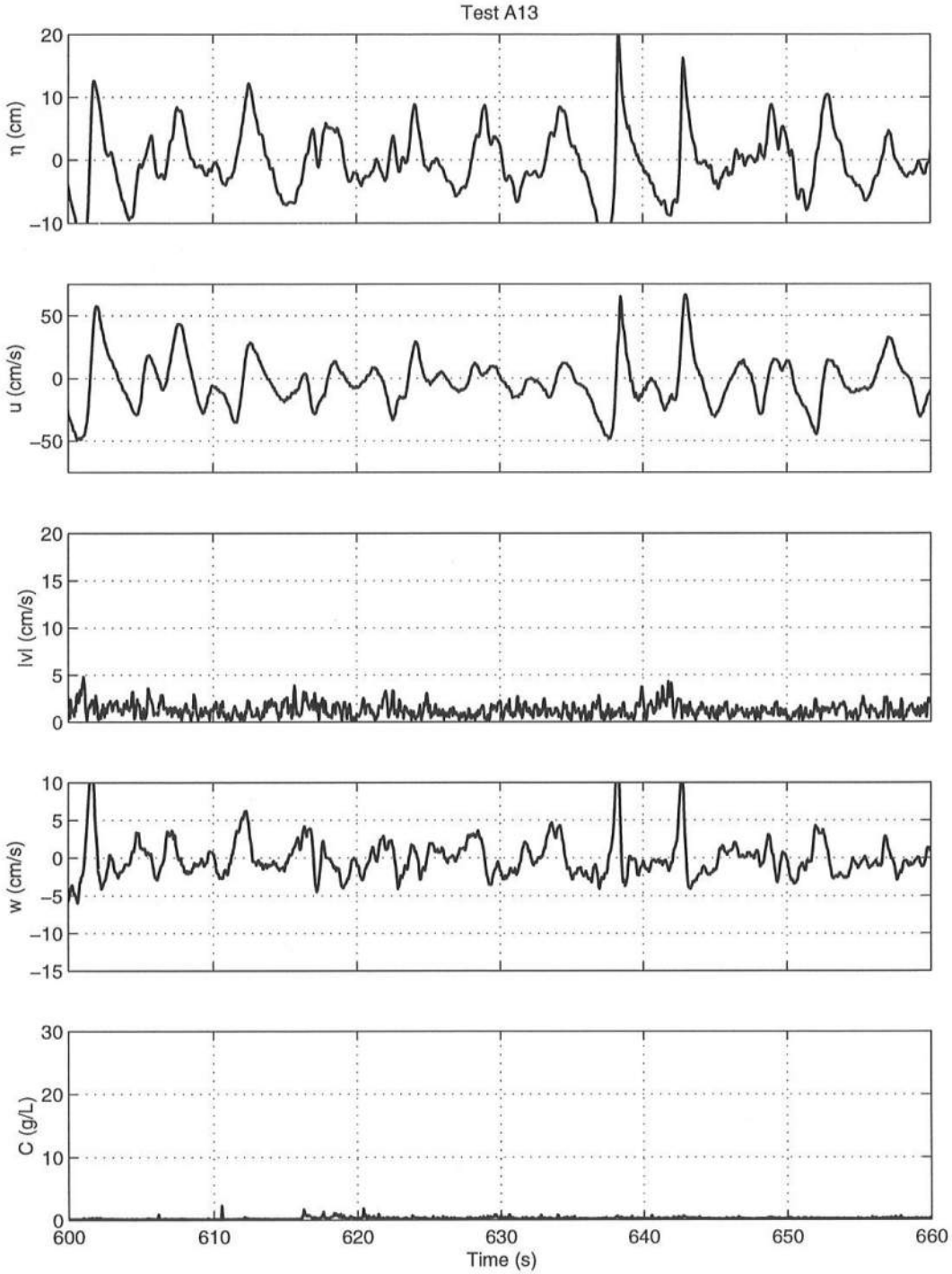

Figure 2.26: Continued

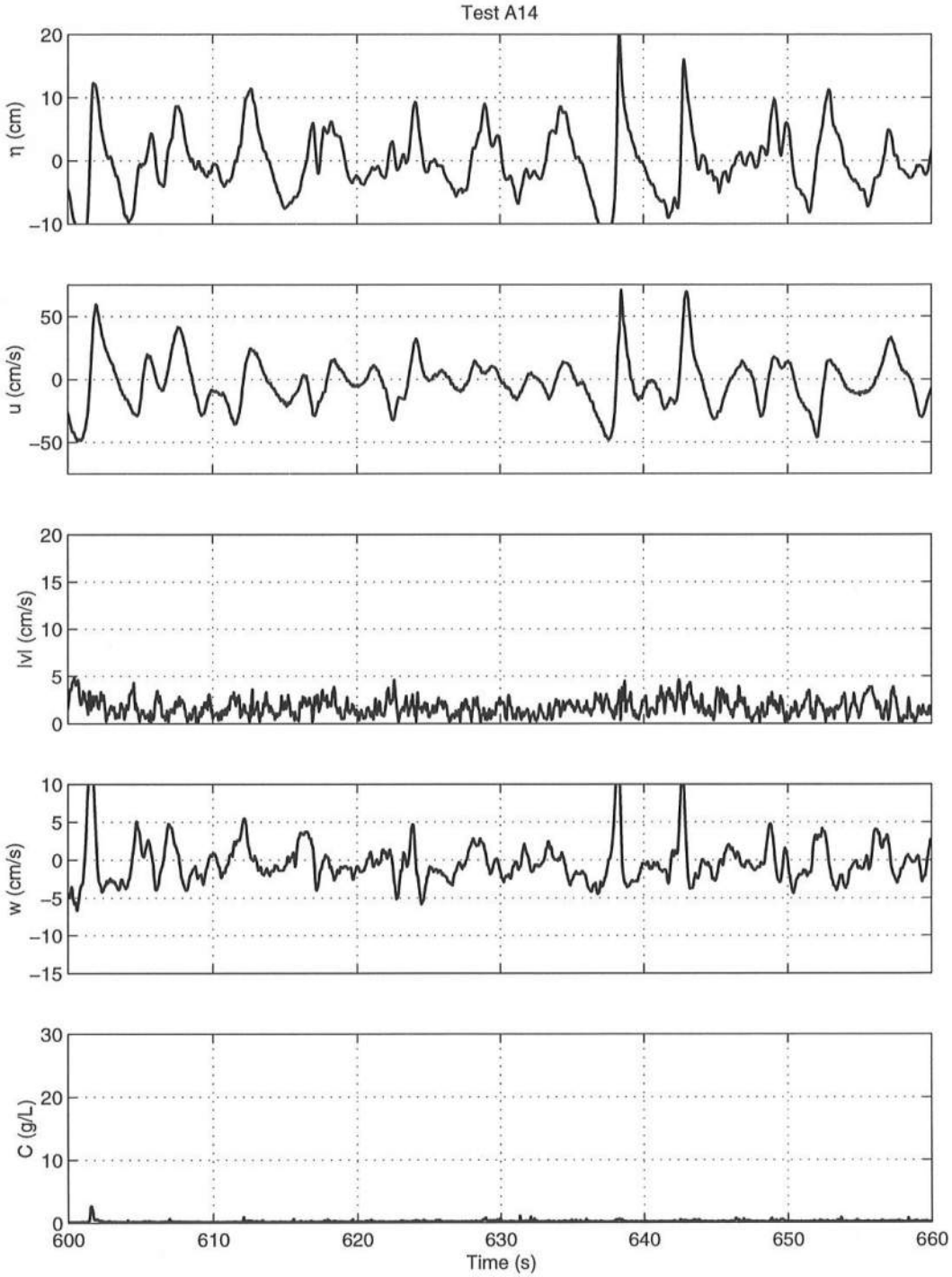

Figure 2.26: Continued

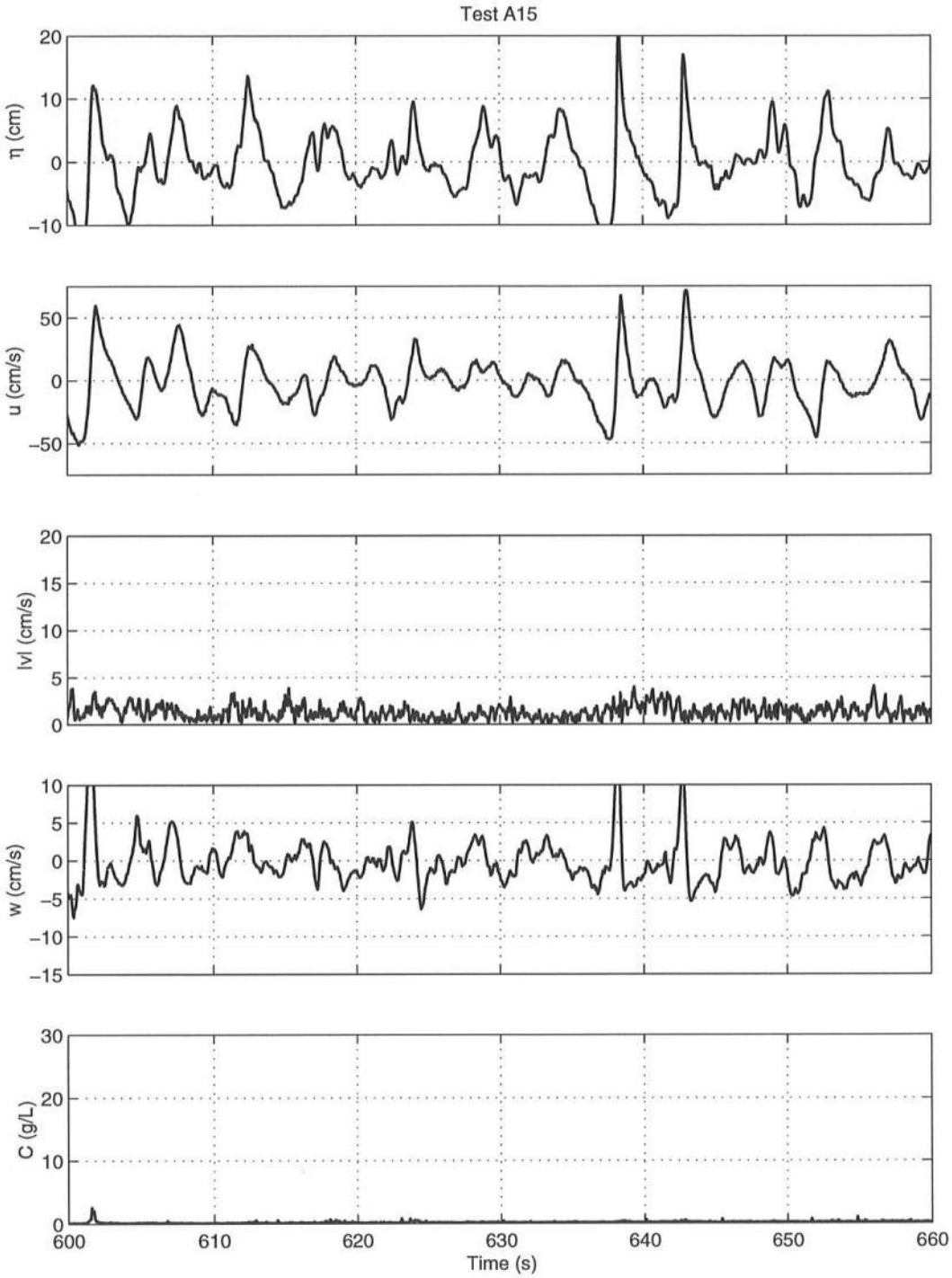

Figure 2.26: Continued

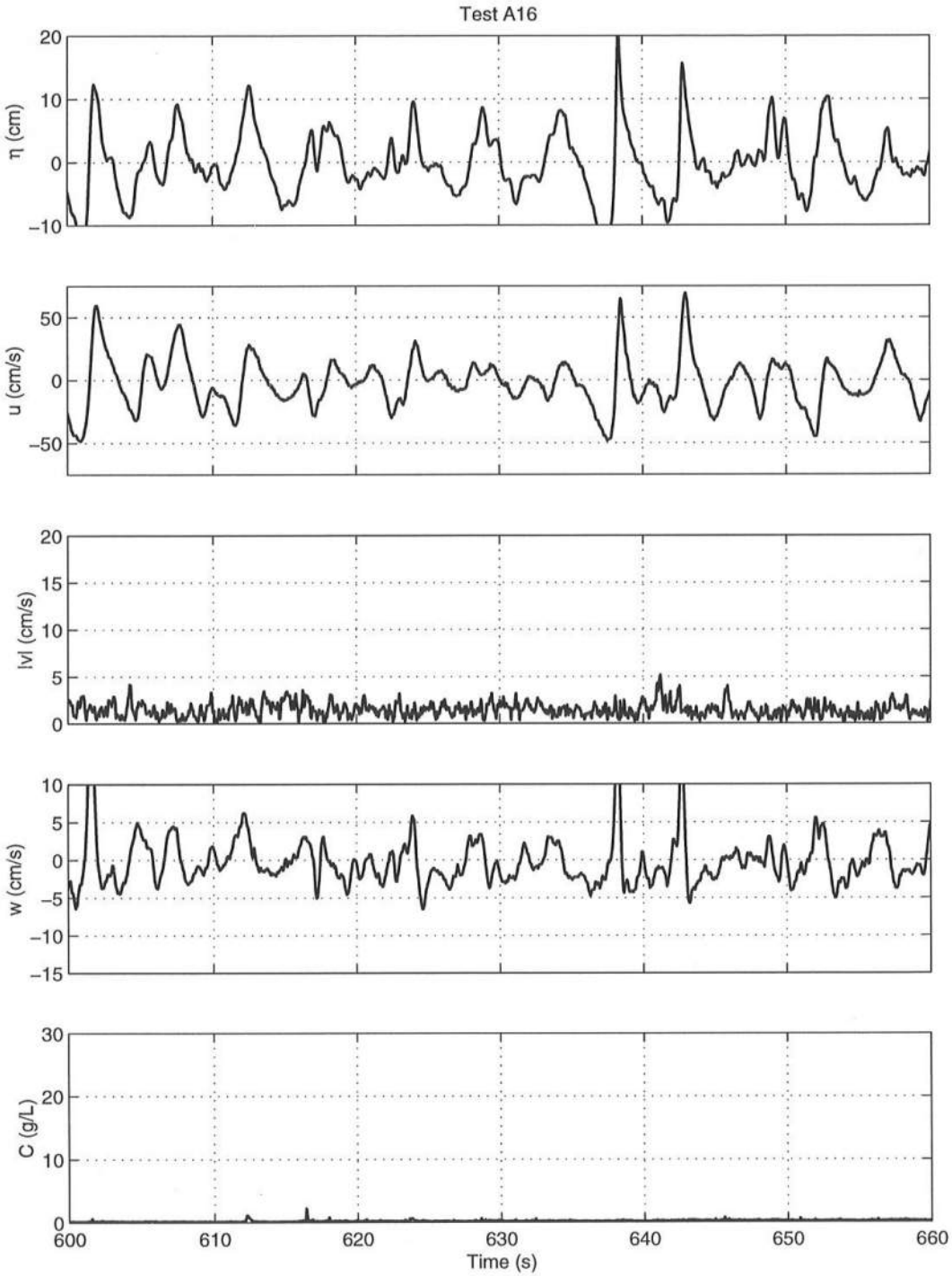

Figure 2.26: Continued

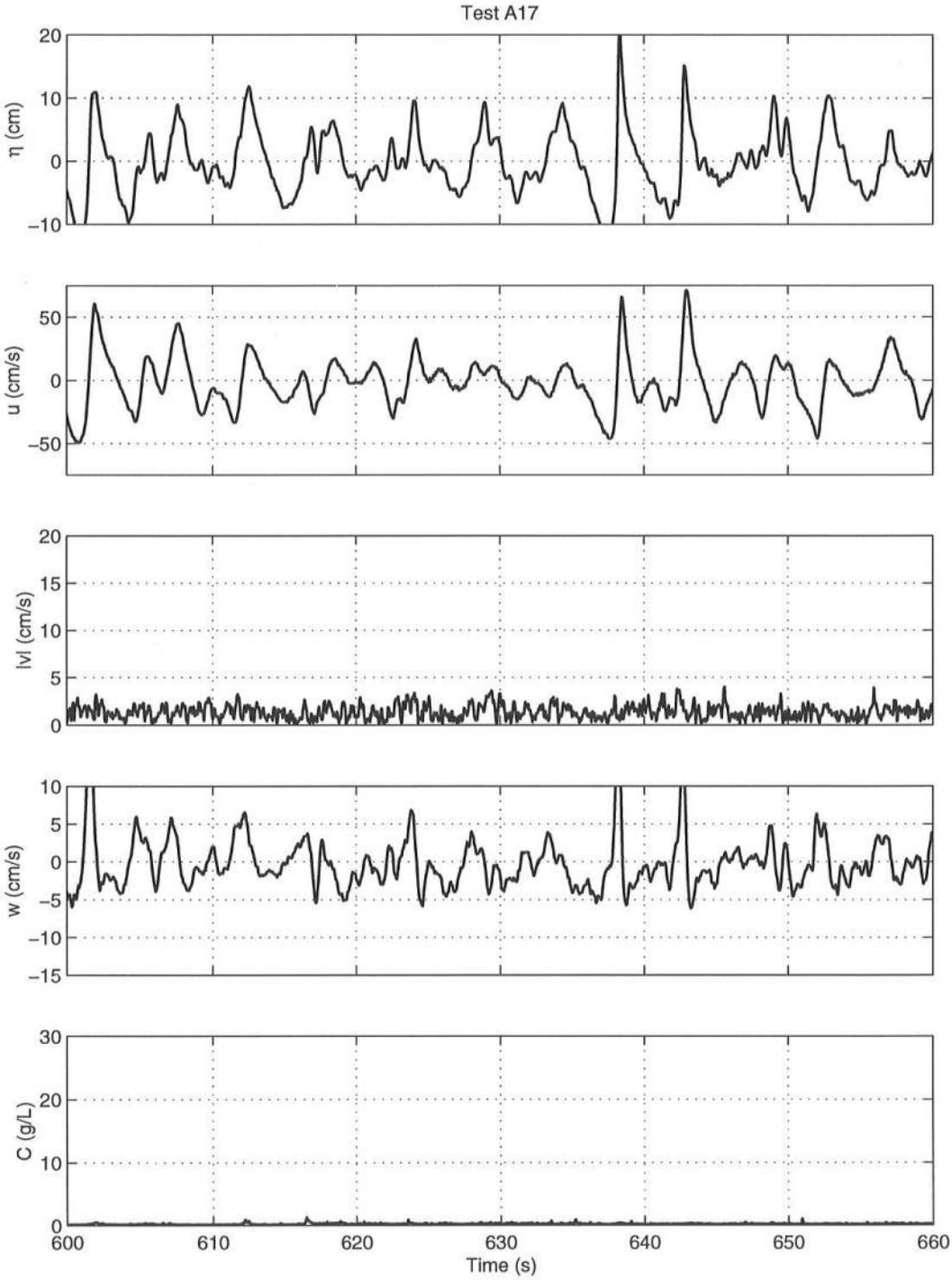

Figure 2.26: Continued

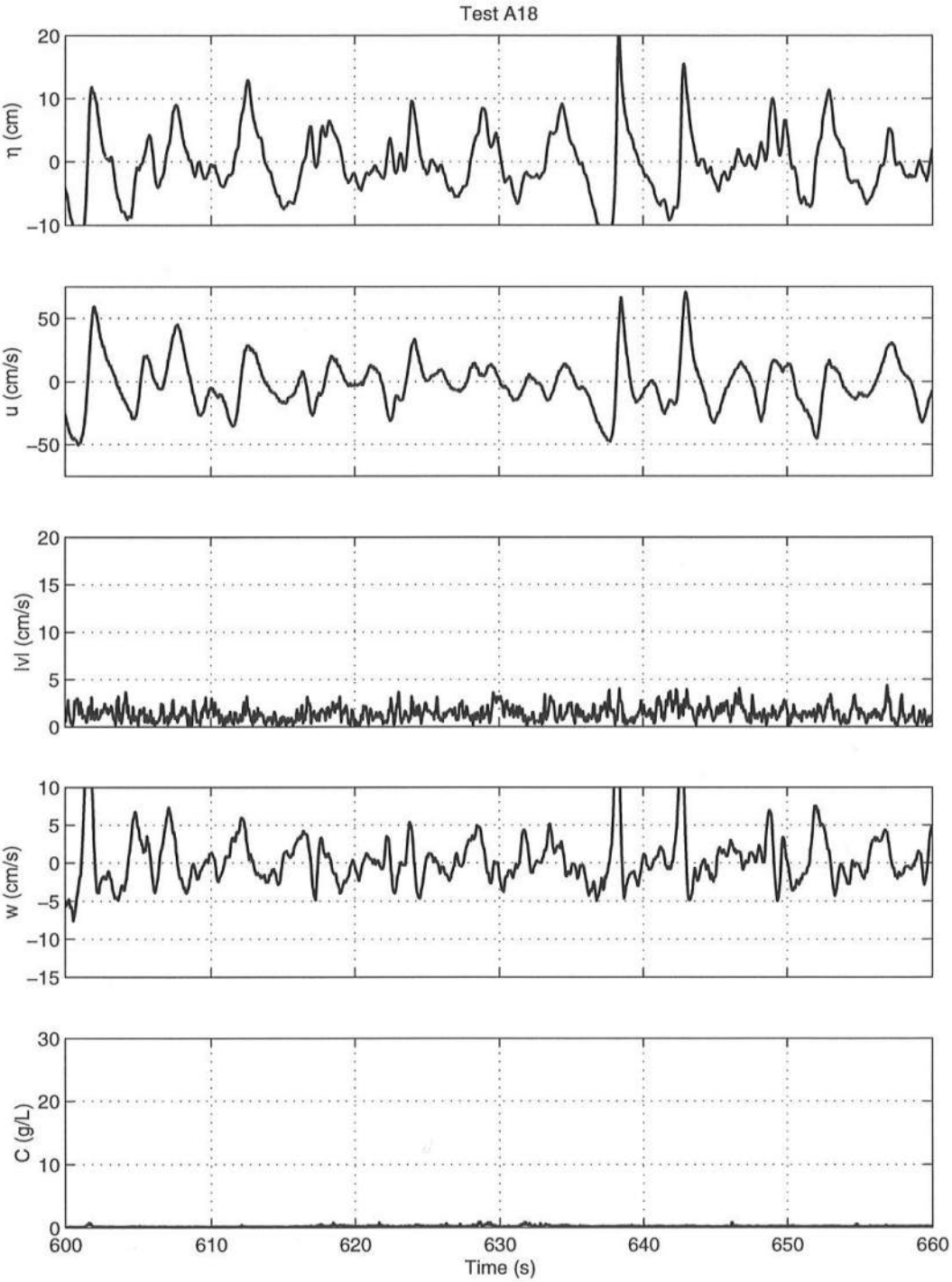

Figure 2.26: Continued

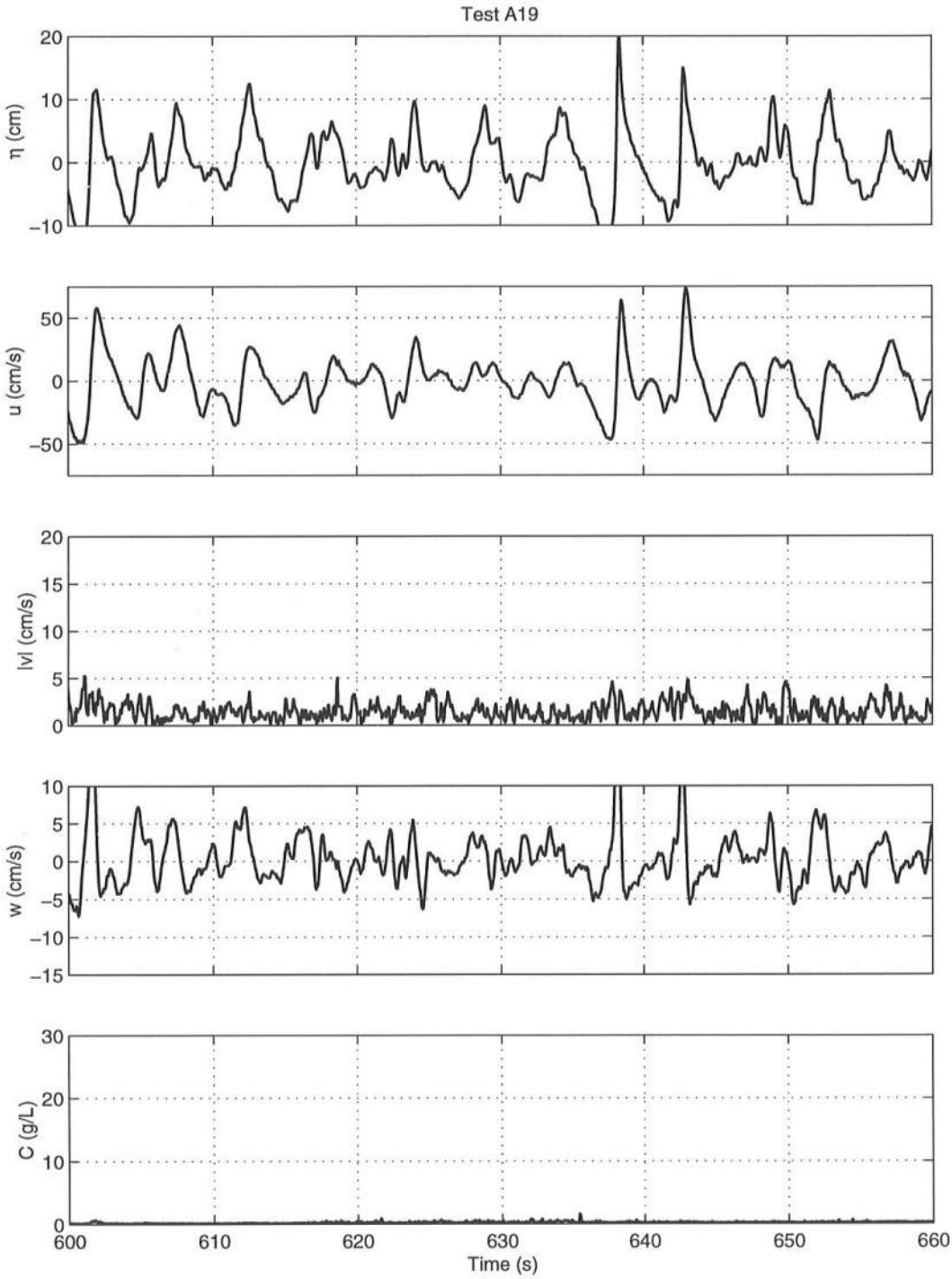

Figure 2.26: Continued

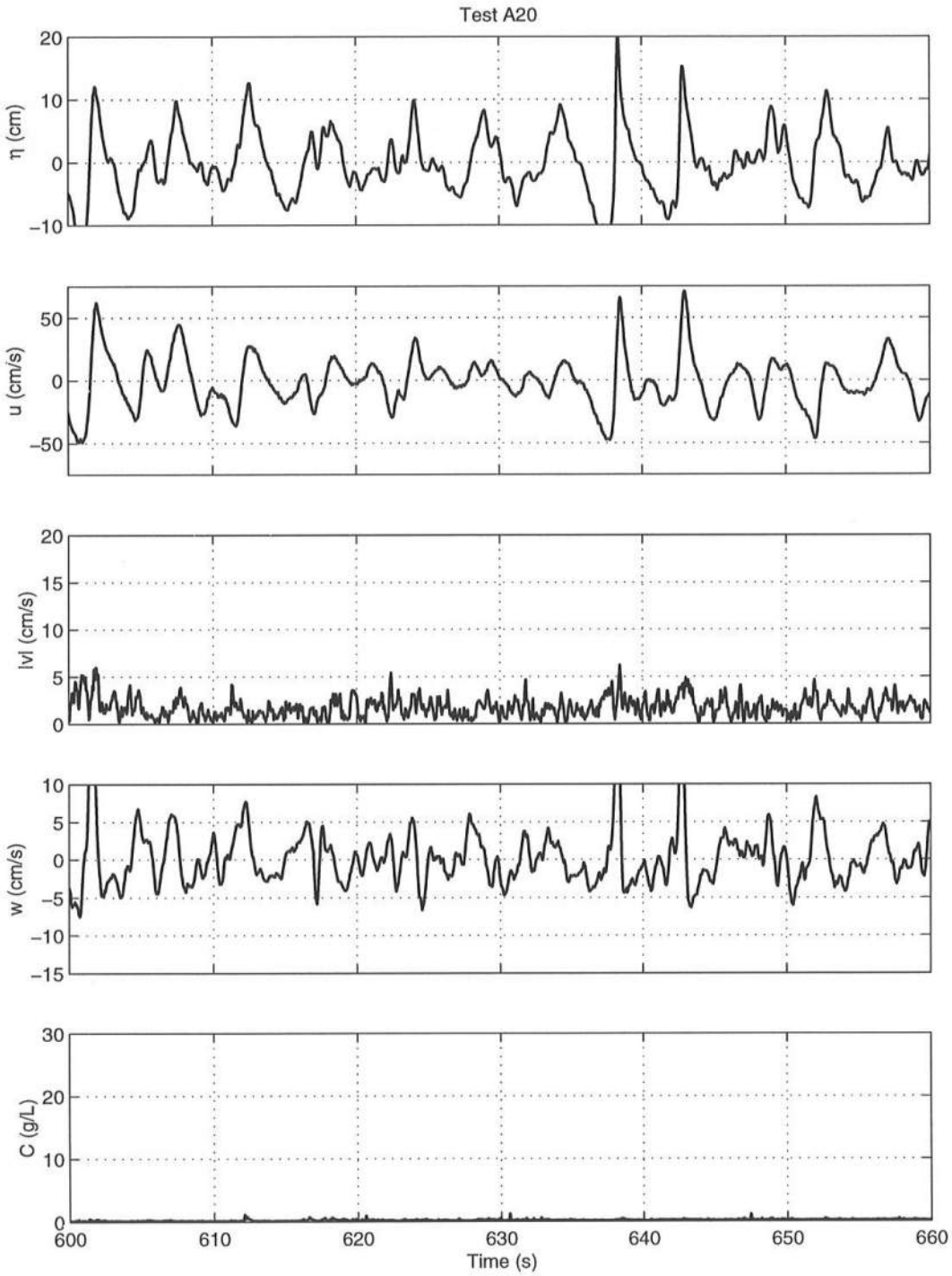

Figure 2.26: Continued

2.4.2 Line B

Figure 2.27 for tests B1–B7 shows approximately ten suspension events under breaking and near-breaking waves. The horizontal velocity u does not indicate any clear correlation with C except that the high frequency oscillations associated with turbulence are detectable during some of the suspension events. The vertical velocity w is very large under some of the steep fronts where η increases rapidly with time. Some of the suspension events occur under the large vertical velocity. Suspension events tend to occur during turbulent events with $|v|$ exceeding approximately 5 cm/s for about 1 s. However, the correlations of w and $|v|$ with C are absent for suspension events that may be caused by the advection and settling of sand particles suspended from the bottom away from the point of the concentration measurement.

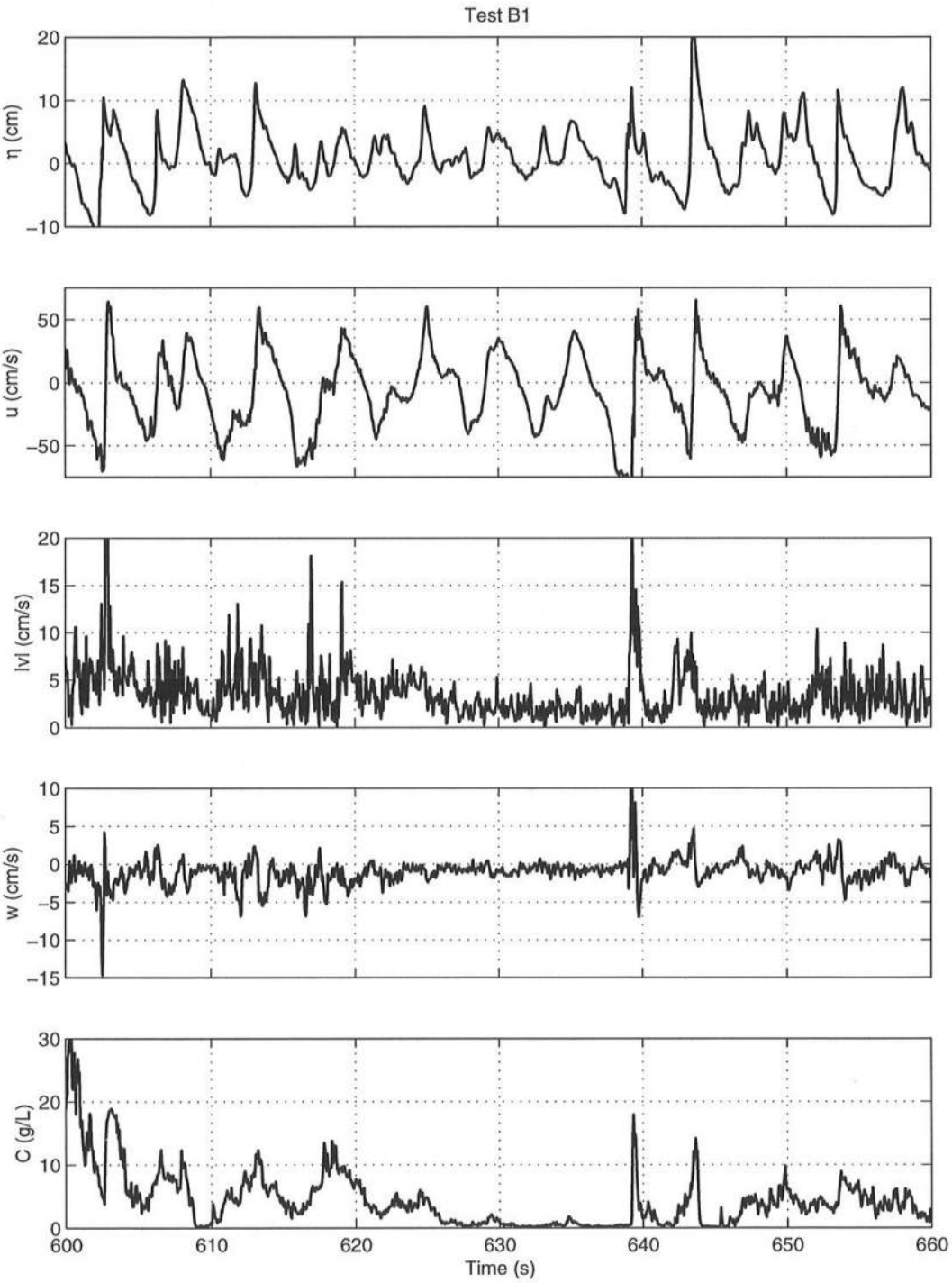

Figure 2.27: Measured Time Series of η, u, $|v|$, w and C for Tests B1–B7

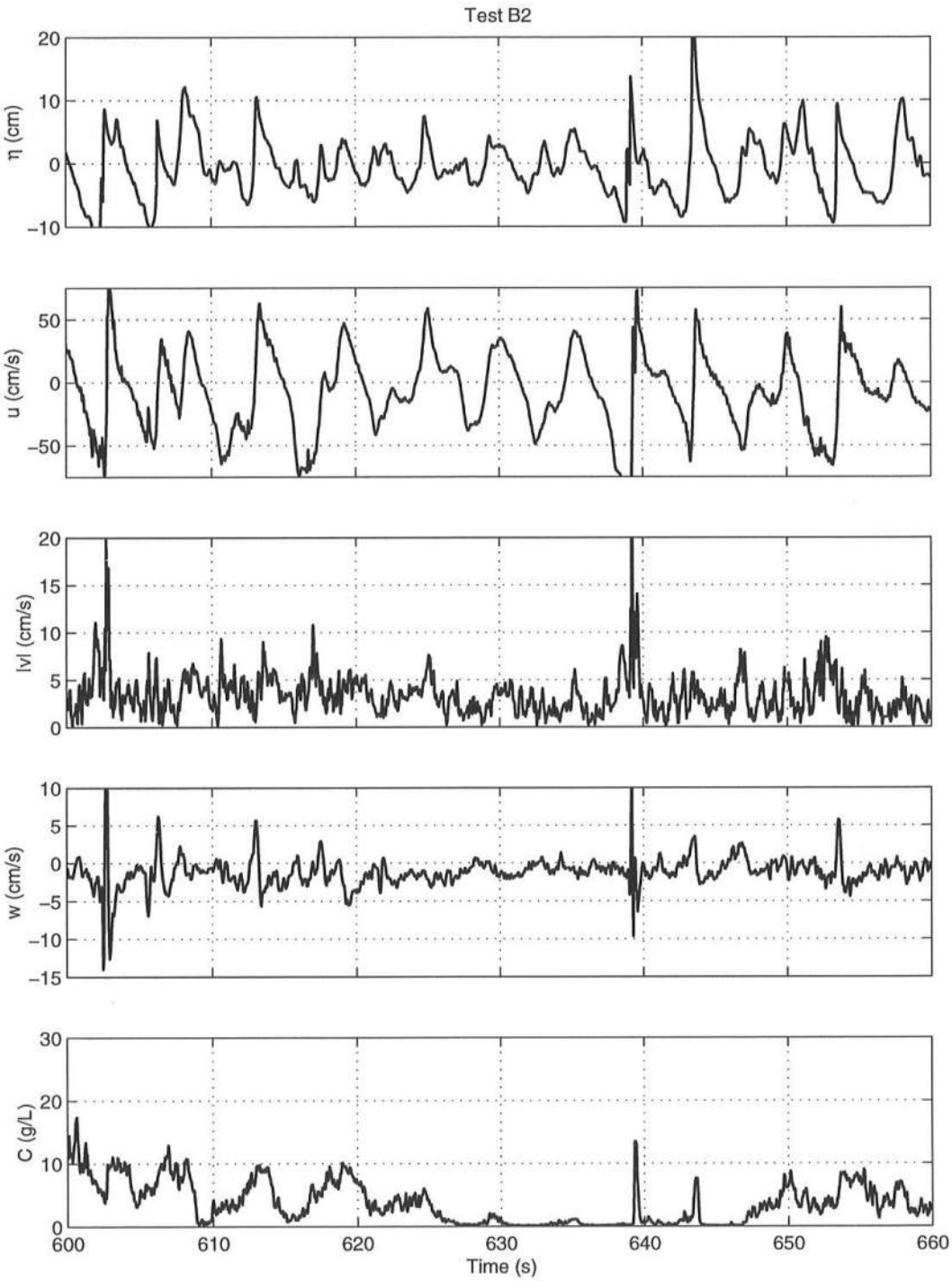

Figure 2.27: Continued

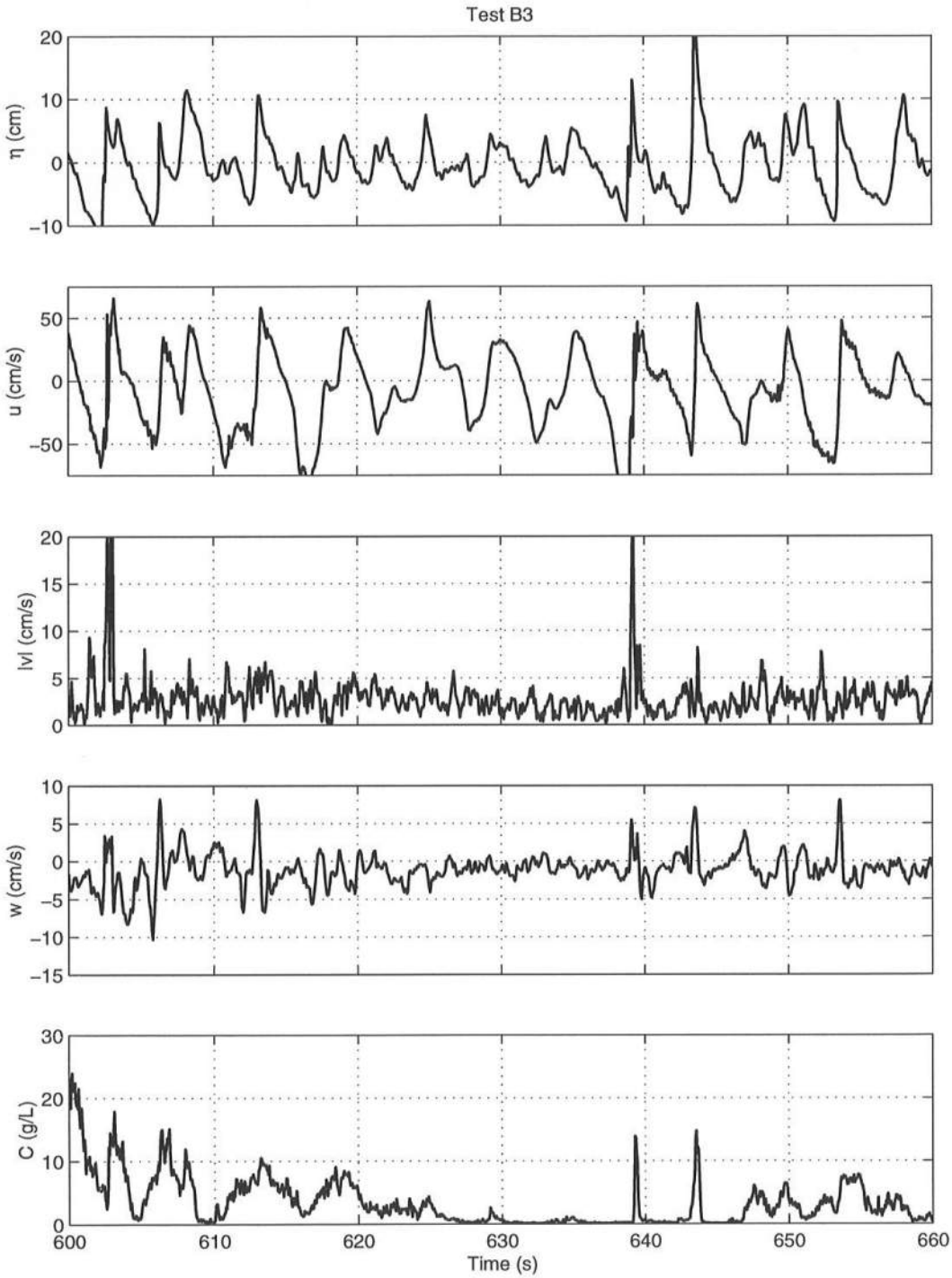

Figure 2.27: Continued

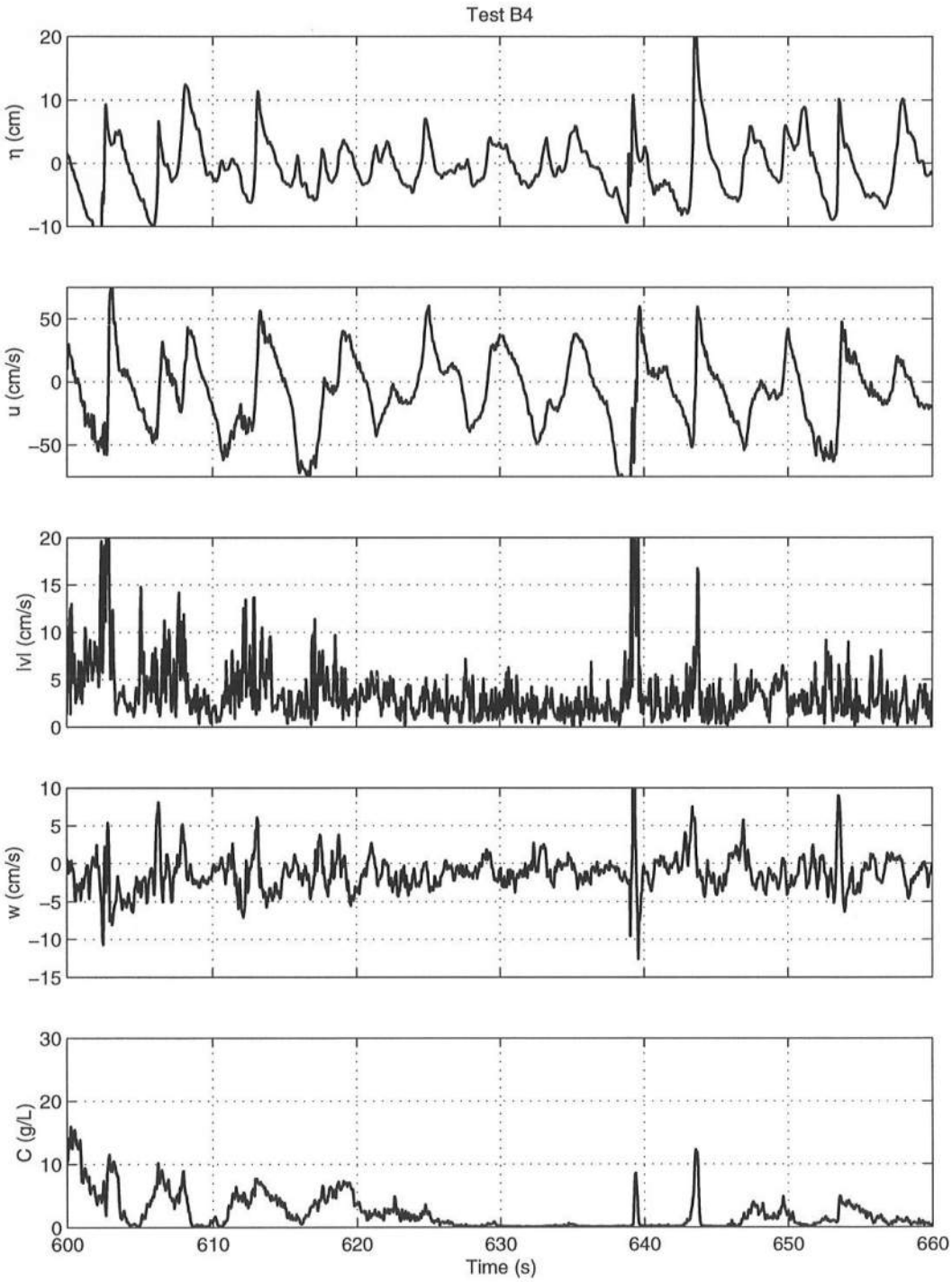

Figure 2.27: Continued

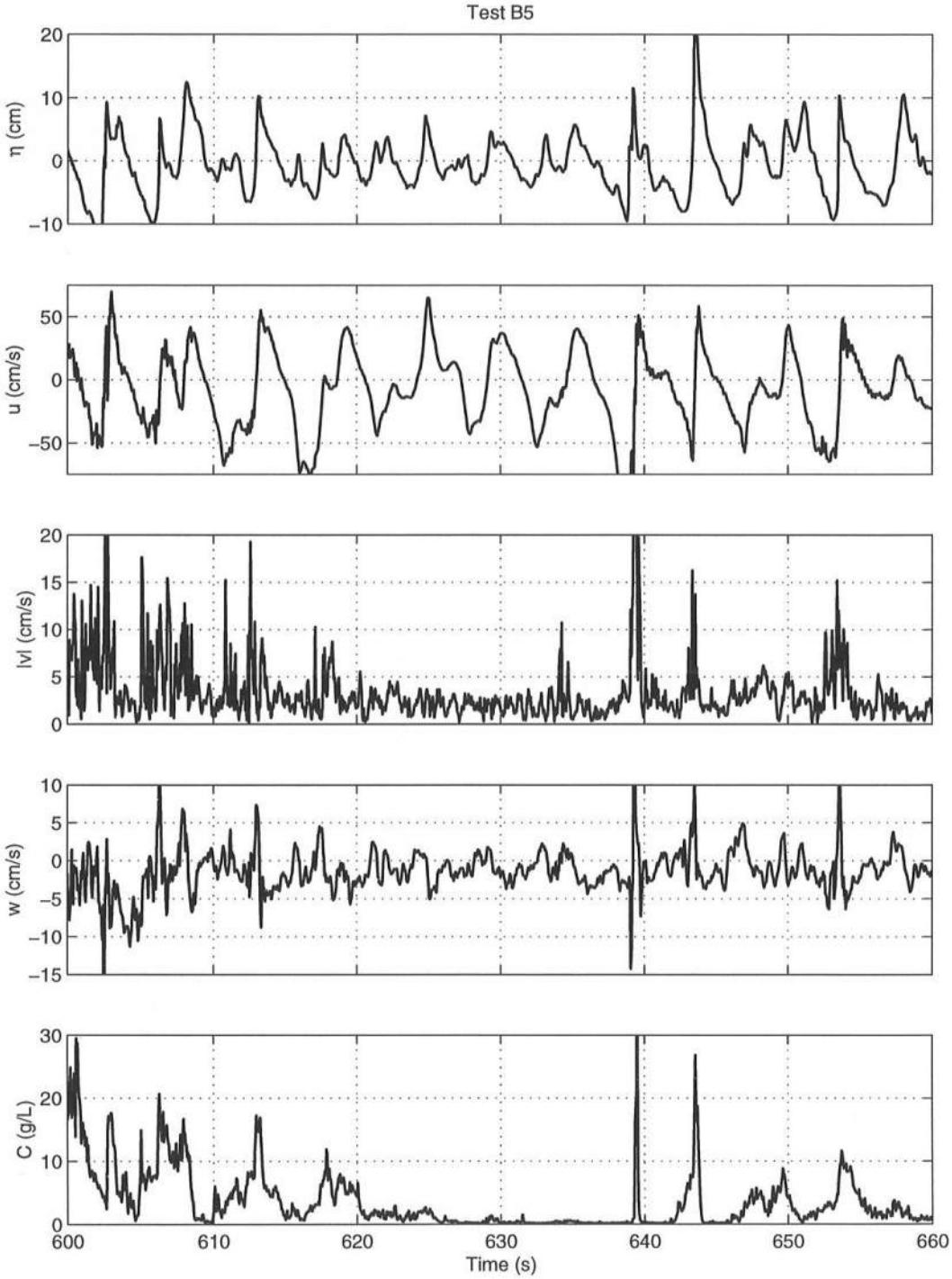

Figure 2.27: Continued

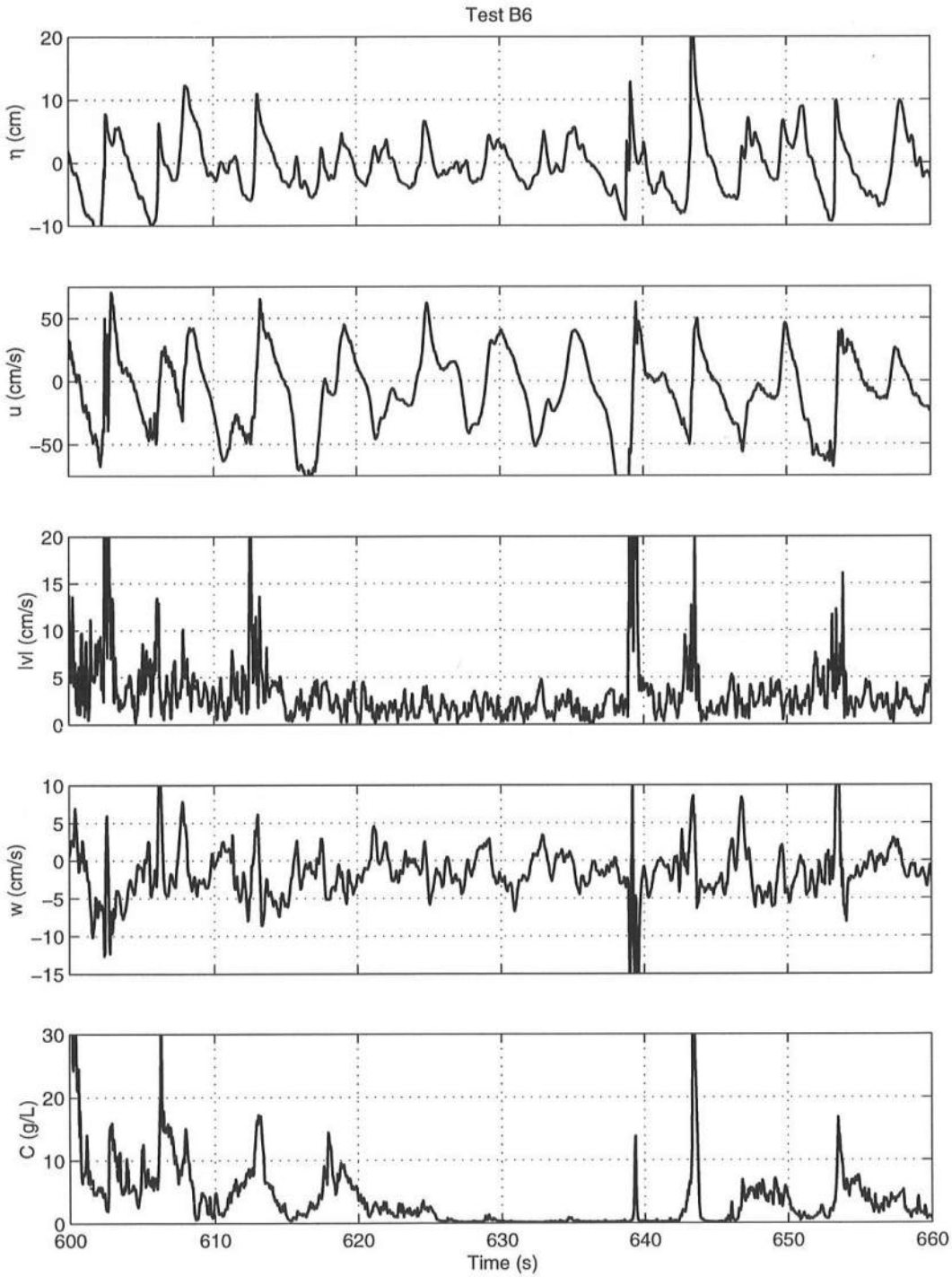

Figure 2.27: Continued

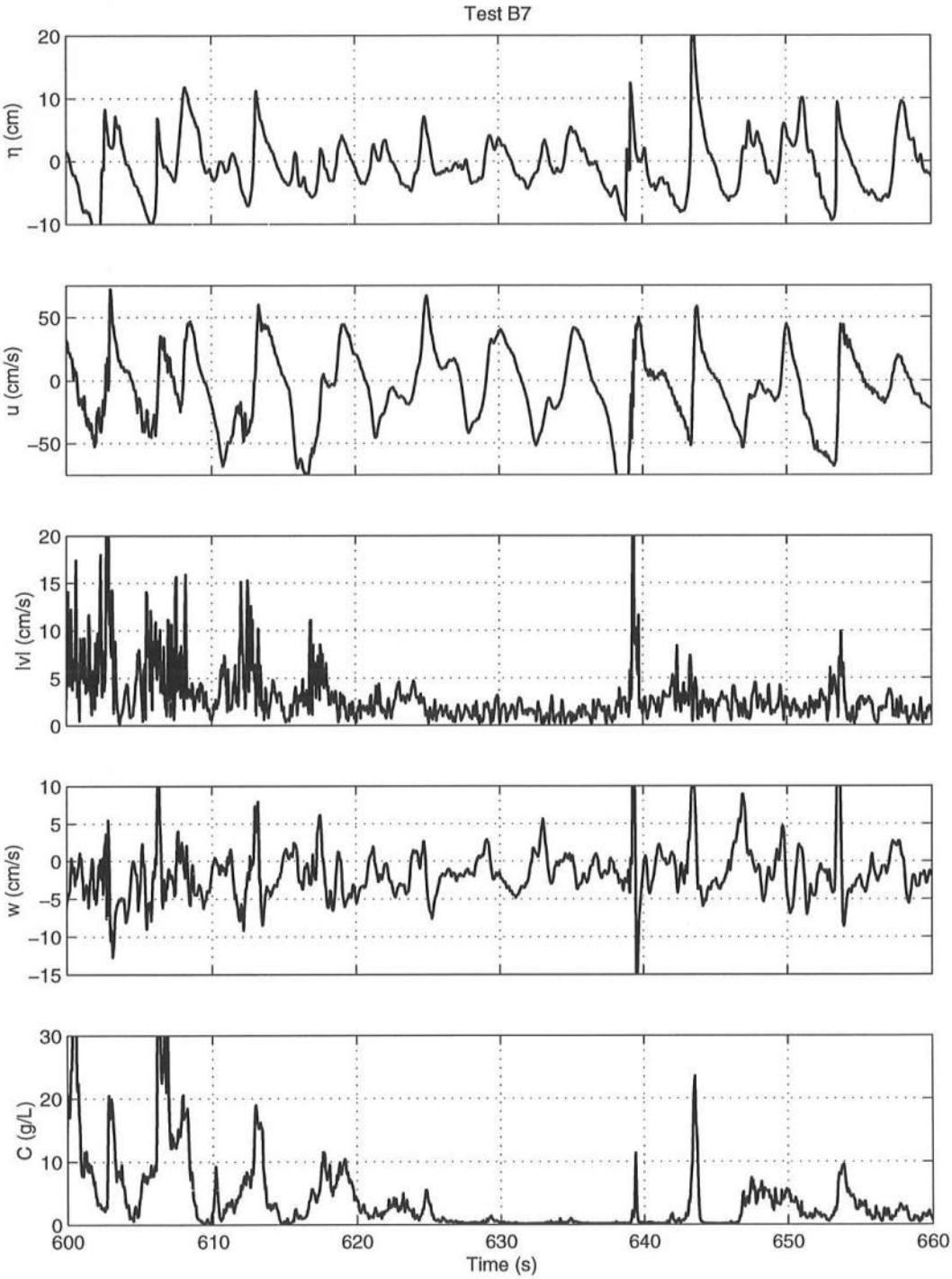

Figure 2.27: Continued

2.4.3 Line C

Figure 2.28 for tests C1–C4 shows a few very intense suspension events lasting for several seconds or longer. These events were observed visually to occur under strong plunging breakers that hit the bottom and lifted a large amount of sand very high in the water column. The sand cloud was visible from above the free surface under such an intense event. The high frequency oscillations in the time series of η and u are detectable during the very intense suspension events but are still secondary to the irregular wave motion. The time series of $|v|$ captures these events more clearly but the timing between $|v|$ and C does not always match. The vertical velocity w shows large fluctuations during the intense suspension events but also includes the wave-induced component which is not related to vortices and turbulence.

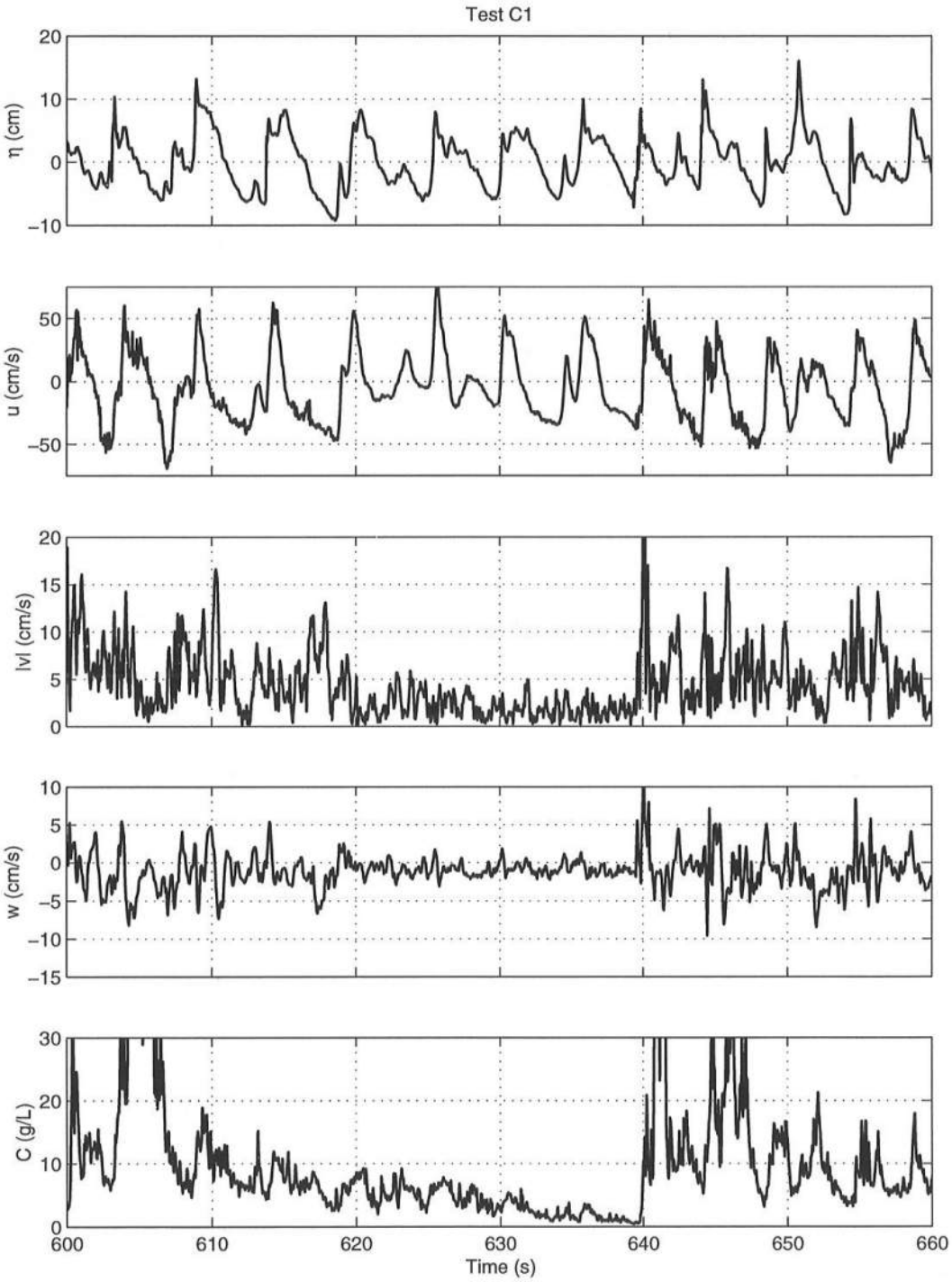

Figure 2.28: Measured Time Series of η, u, $|v|$, w and C for Tests C1–C4

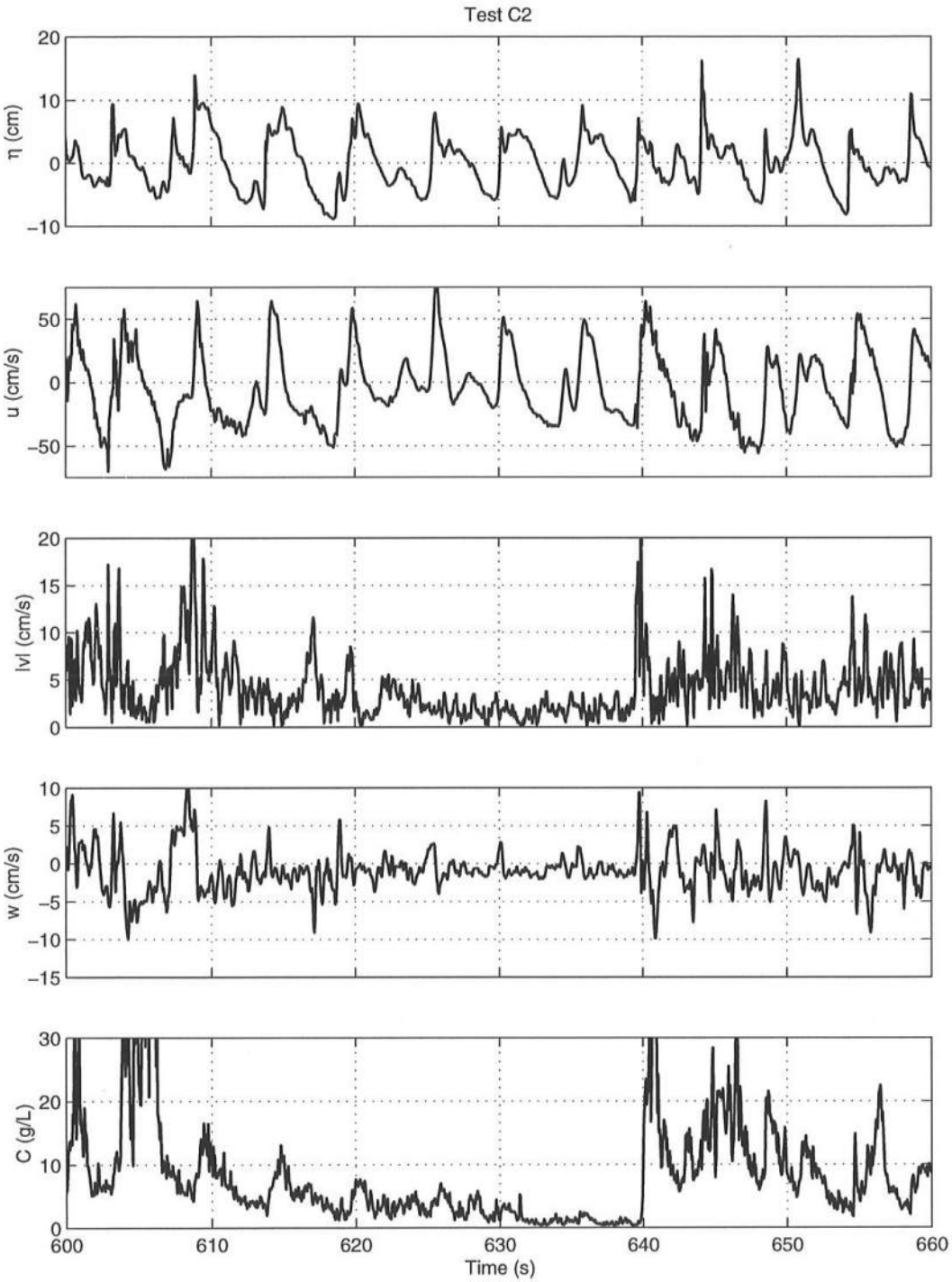

Figure 2.28: Continued

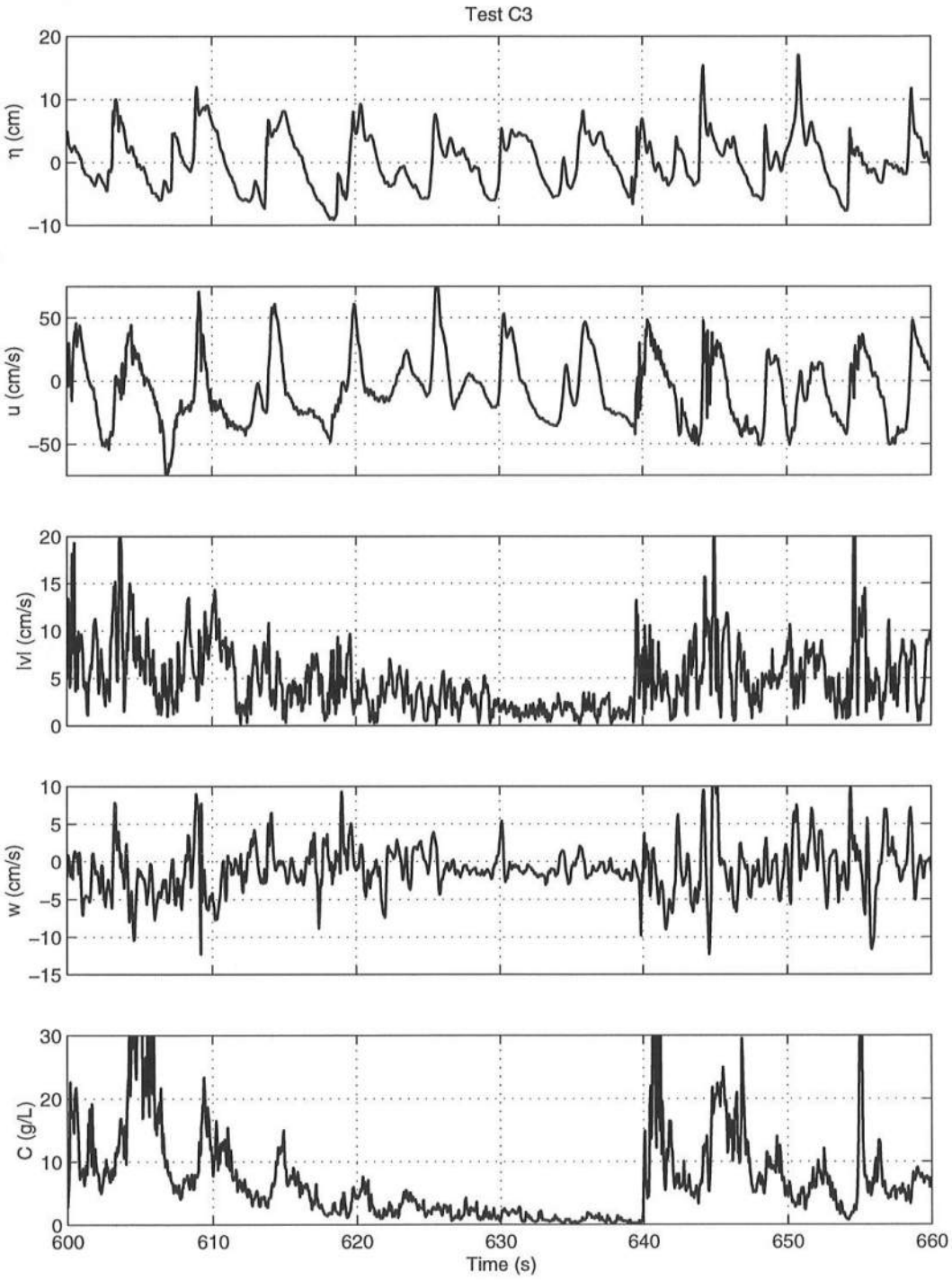

Figure 2.28: Continued

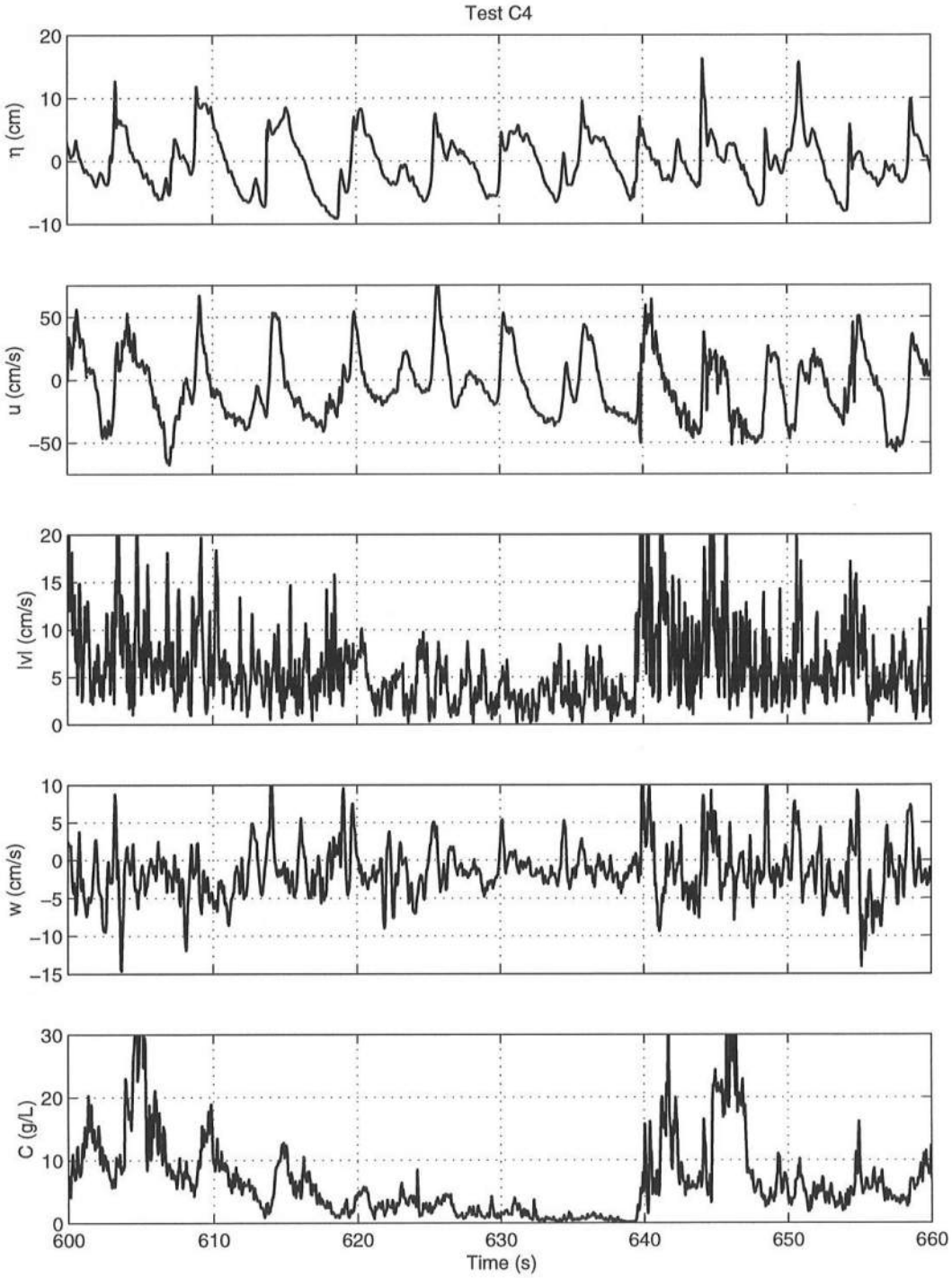

Figure 2.28: Continued

2.4.4 Line D

Figure 2.29 for tests D1–D3 shows several suspension events under the transitional waves from breaking waves to bores. The time series of η do not indicate any major change from η for tests C1–C4 in Figure 2.28 but the time series of u change significantly from line C to line D. A strong offshore velocity occurs under some of the wave troughs for all three elevations for line D (tests D1, D2 and D3). The cause of this strong offshore velocity is not clear but may be related to strong horizontal eddies observed at line D. The horizontal and vertical velocities do not indicate any clear correlation with the concentration. The alongshore velocity $|v|$ fluctuates extensively even during no suspension events. This implies that suspension events do not occur under some turbulent bores.

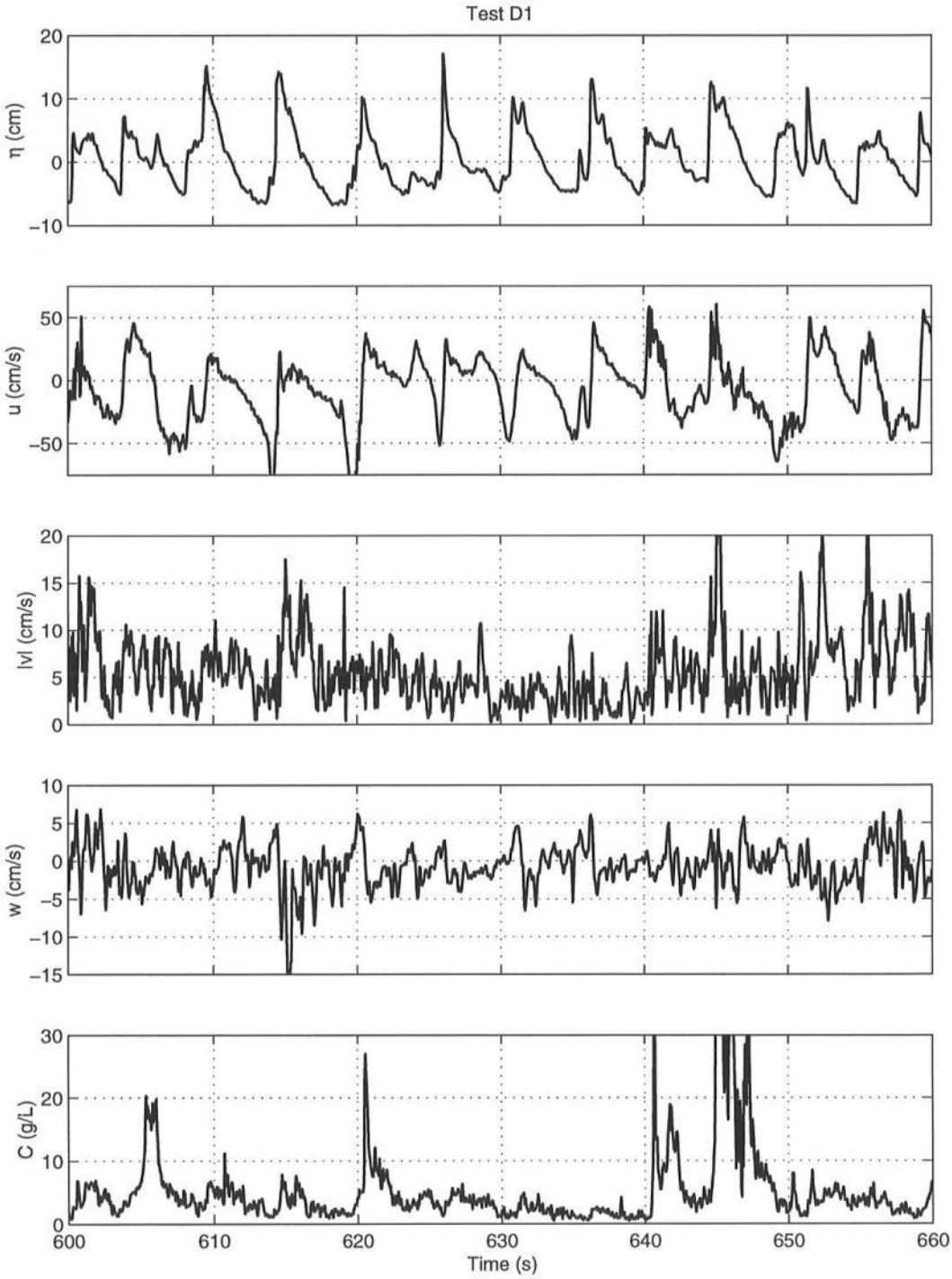

Figure 2.29: Measured Time Series of η, u, $|v|$, w and C for Tests D1–D3

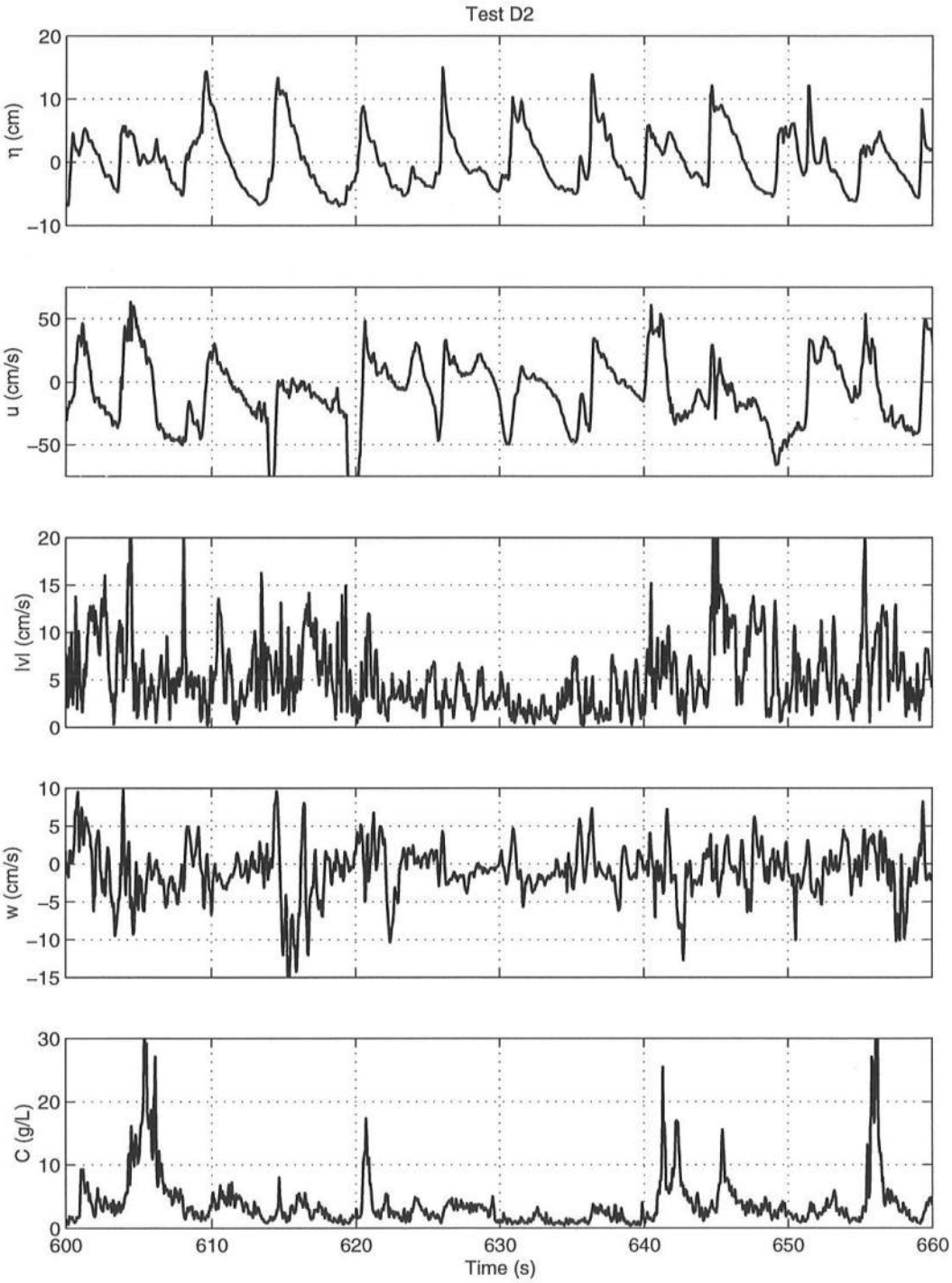

Figure 2.29: Continued

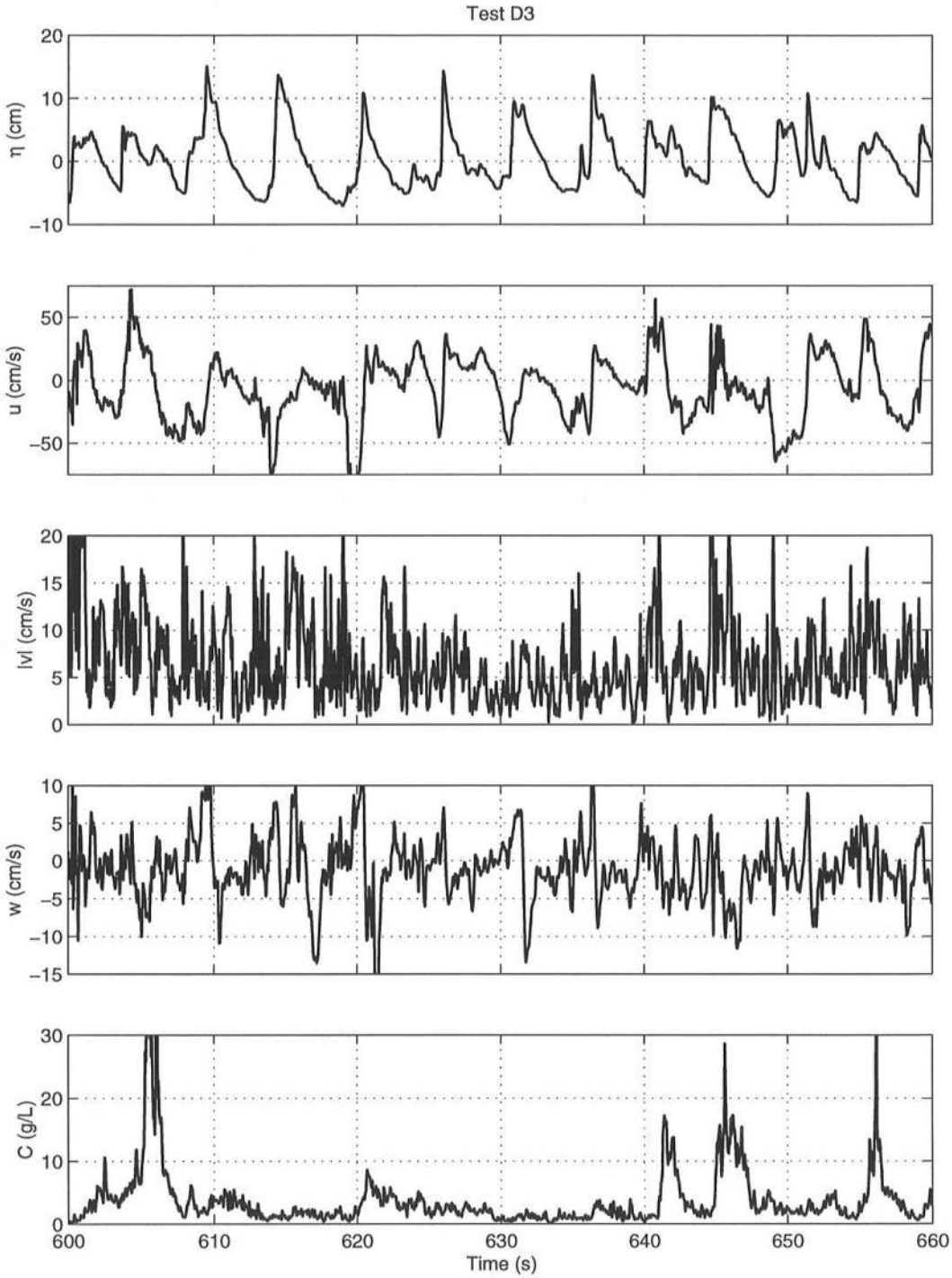

Figure 2.29: Continued

2.4.5 Line E

Figure 2.30 for tests E1–E3 shows two major suspension events and several smaller events under bores. The time series of η indicates the presence of low frequency oscillations where the spectra S_η at line E are presented in Figure 2.19. The cross-shore velocity u is skewed offshore due to the effect of down-rush from the swash zone on the steep foreshore. The comparison of the time series of u and C indicates sand suspension under uprushing bores as was observed on a natural beach by Puleo *et al.* (2000). The time series of $|v|$ shows the presence of fairly intense turbulence under most of the bores. The vertical velocity w tends to be large upward at the time of u increasing rapidly with time as implied by (2.2). The vertical velocity tends to become negative downward immediately after the large upward velocity possible because of the settlement of suspended sand. Bores did not suspend sand particles up to the free surface.

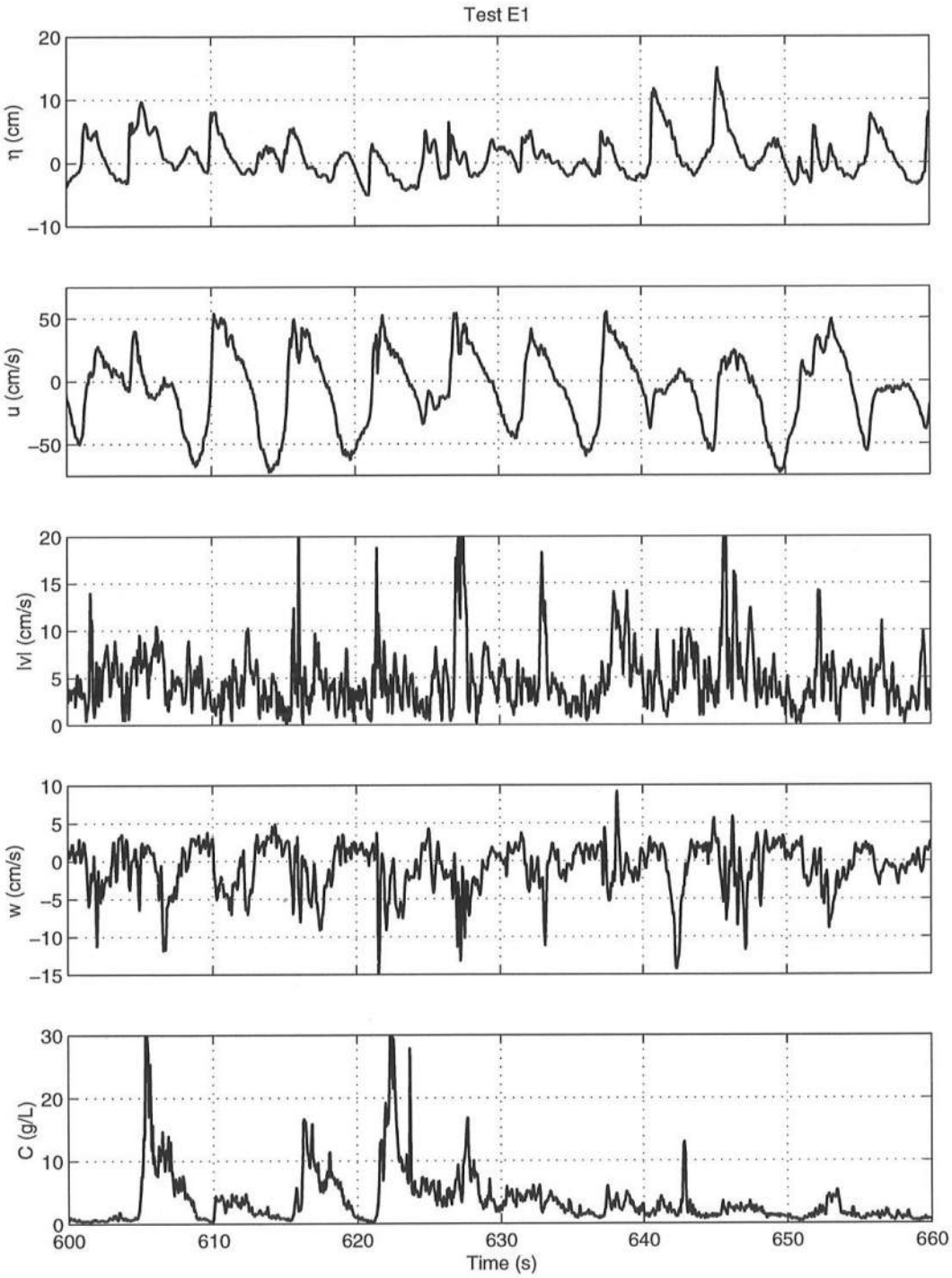

Figure 2.30: Measured Time Series of η, u, $|v|$, w and C for Tests E1–E3

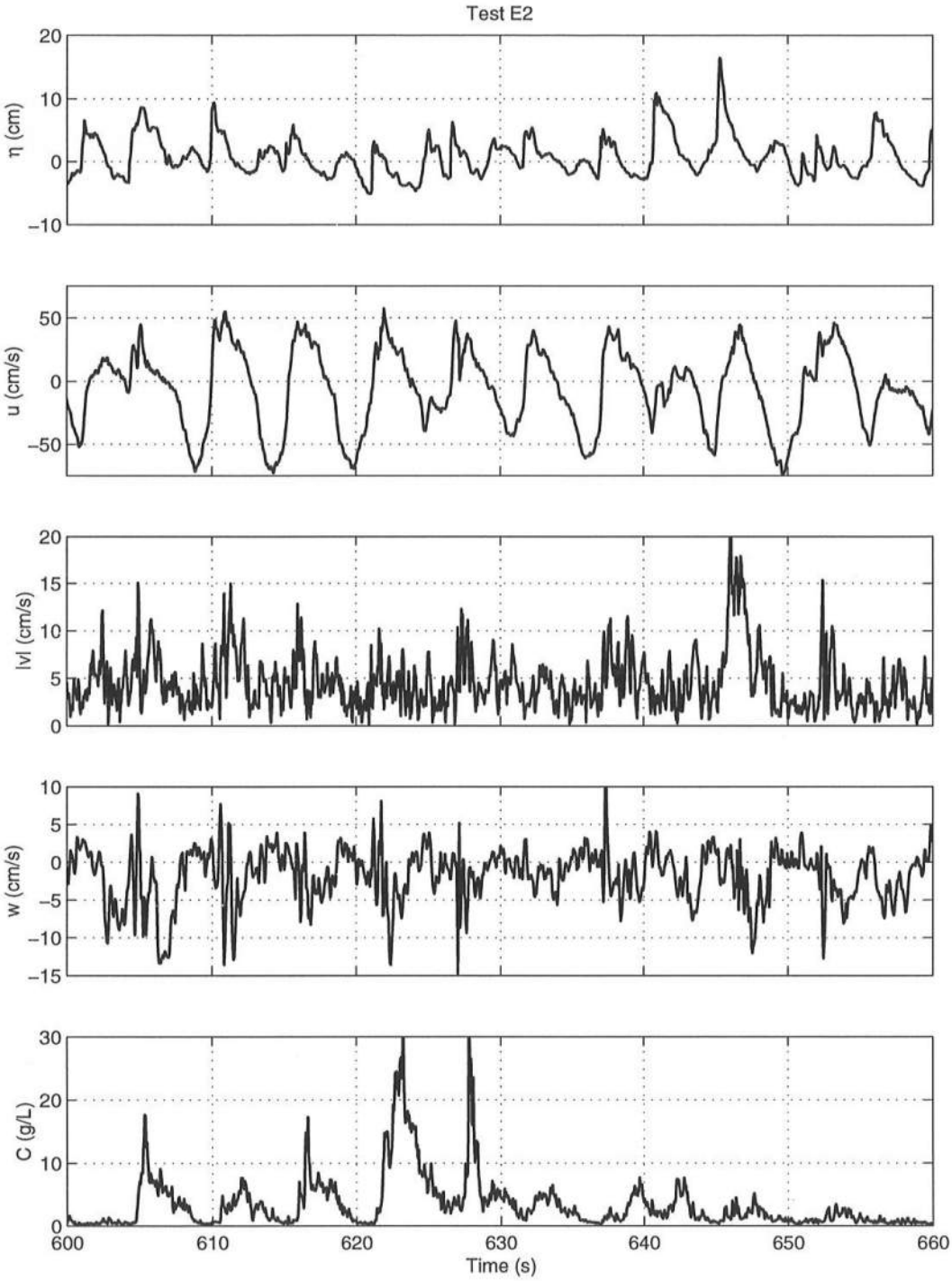

Figure 2.30: Continued

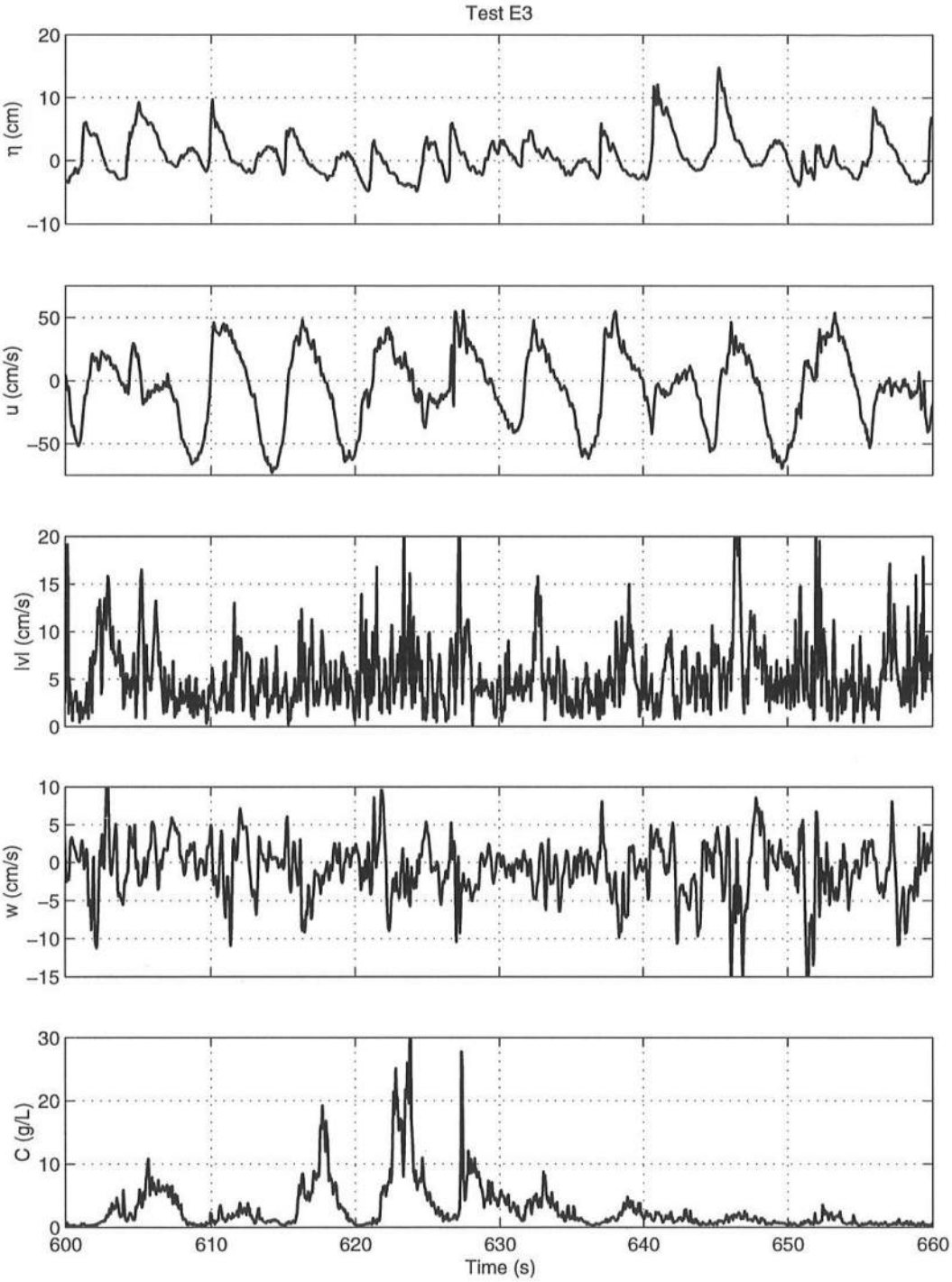

Figure 2.30: Continued

2.5 Time-Averaged Sand Fluxes

The time series of u, w and C presented in the previous section are used to calculate the time-averaged cross-shore and vertical sediment fluxes:

$$\begin{aligned} \overline{uC} &= \overline{u}\,\overline{C} + \overline{u_t C_t}, \\ \overline{wC} &= \overline{w}\,\overline{C} + \overline{w_t C_t} \end{aligned} \tag{2.3}$$

where $C_t = (C - \overline{C})$ is the time-varying concentration with zero mean. The concentration C in grams per liter is converted to the dimensionless volumetric sand concentration defined as the sand volume per unit volume of the mixture where the specific gravity of the sand was 2.6. The time-averaged fluxes are relatively small and expressed in the units of cm/hr in comparison with the rate of the bottom elevation change during the 37 test which was less than 0.1 cm/hr. The time-varying components u_t, w_t and C_t could be separated into high and low frequency components [e.g., Grasmeijer and van Rijn (1999)] but it would be difficult to interpret such results because the low frequency components are related to intermittent irregular wave breaking and turbulence as well as low frequency waves.

Table 2.14 lists the vertically averaged values of the six flux components in (2.3) and $w_f\overline{C}$ where the sand fall velocity in quiet water was $w_f = 2.0$ cm/s. At line A, the local fluxes decreased upward and approached zero. Consequently, the average value for the region of 1-20 cm above the local bottom was smaller than the absolute values of the fluxes in the region of 1-4 cm above the bottom. The fluxes in this region were affected by vortices ejected from the rippled bed and may depend on the locations of the sensors relative to the three-dimensional ripples during the tests. These measurements were not made in this experiment. The fluxes at lines B–E inside the surf zone, listed in Table 2.14, did not vary much in the region of 1-n cm above the bottom with n = 7,4,3 and 3 for B, C, D and E, respectively.

Table 2.14: Time-Averaged Sediment Fluxes

	Cross-Shore			Vertical			
Line	$\overline{u}\,\overline{C}$ (cm/hr)	$\overline{u_t\,C_t}$ (cm/hr)	$\overline{u\,C}$ (cm/hr)	$\overline{w}\,\overline{C}$ (cm/hr)	$\overline{w_t\,C_t}$ (cm/hr)	$\overline{w\,C}$ (cm/hr)	$w_f\,\overline{C}$ (cm/hr)
A	-1.9	6.1	4.2	-0.4	0.4	0.0	2.3
B	-25.2	20.4	-4.8	-3.5	0.1	-3.4	7.8
C	-43.7	36.6	-7.1	-6.1	-1.1	-7.2	12.9
D	-32.3	26.7	-5.6	-3.6	0.0	-3.6	9.0
E	-10.6	18.3	7.7	-1.7	-1.3	-3.0	4.1

2.5.1 Cross-Shore Fluxes

The offshore flux $\overline{u}\overline{C}$ due to the undertow $\overline{u} < 0$ is the maximum at line C where intense breaking occurs. The onshore flux $\overline{u_tC_t}$ due to the correlated time-varying components is also the maximum at line C. The net cross-shore flux $\overline{uC}$ is very small and probably inaccurate in light of the errors of the measured u and C. Is is noted that the depth-integrated values of $\overline{uC}$ must be zero for the equilibrium profile. No measurements were made in the large area near the free surface as shown in Figure 2.2 and in the sheet-flow layer of very high sand concentrations on the bed [e.g., McLean *et al.* (2001)]. Sand particles on the bed in the surf zone did not appear to move in layers due to frequent vortices and turbulence. In any case, it is very difficult to measure the net cross-shore flux $\overline{uC}$ accurately as is the case with the numerical prediction of the net cross-shore flux [Kobayashi and Johnson (2001)].

2.5.2 Vertical Fluxes

The vertical fluxes are smaller than the cross-shore fluxes. At line A, the values of $\overline{w}\overline{C}$, $\overline{w_tC_t}$ and $\overline{wC}$ are very small except at 1 cm above the bed. At lines B–E, $\overline{w}\overline{C}$ and $\overline{wC}$ do not vary much vertically and $\overline{w_tC_t}$ is fairly small. As a result, the net vertical flux $\overline{wC}$ is caused mostly by the downward flux $\overline{w}\overline{C}$ due

to the mean $\overline{w} < 0$ listed in Table 2.11. If the measured vertical velocity w were the same as the fluid velocity, $\overline{wC}$ should be the net suspension rate which must be positive and equal to the settling rate $w_f\overline{C}$ for the equilibrium profile [Kobayashi and Johnson (2001)]. If the measured mean vertical velocity $\overline{w}$ corresponds to the sand fall velocity, $\overline{w} = -w_f$ and $\overline{w}\overline{C} = -w_f\overline{C}$. The measured vertical fluxes listed in Table 2.14 suggest that the measured w is an intermediate velocity between the fluid and sand velocities. Admittedly, the measurements may not be accurate enough to estimate these small vertical fluxes. In conclusion, it is not possible to explain the measured bottom elevation change less than 0.1 cm/hr using the measured vertical fluxes.

2.6 Conclusions

A laboratory experiment was conducted in a wave flume to observe and measure sand suspension events under shoaling waves on a rippled bed and under breaking waves and bores on an equilibrium terraced beach consisting of fine sand. The same incident irregular waves were generated for 37 tests to measure the three-dimensional velocities and concentrations at the 37 locations shown in Figure 2.2. The measured intermittent suspension events were repeatable and not random. The measured free surface elevations and cross-shore velocities were dominated by irregular wave motions and did not allow the easy detection of vortices and turbulence that cause sand suspension. The measured vertical velocity included both wave and turbulent motions that were difficult to distinguish. The measured alongshore velocity was shown to be an effective proxy for detecting three-dimensional vortices and turbulence near the rippled bed and inside the surf zone. The spectra of the alongshore velocities inside the surf zone were dominated by low frequency components associated with intermittent irregular wave breaking.

The measured sand concentrations were dominated by intermittent suspension events as observed previously on natural sand beached by many researchers.

Large shoaling waves in a wave group caused intermittently high sand concentrations above the rippled bed under the large onshore velocity accompanied by the large alongshore velocity fluctuation. Intermittent suspension events were also measured under the steep fronts of breaking waves with large fluid accelerations which were also shown to be the locations of large vertical velocities and large alongshore velocity fluctuations. Strong plunging breakers occurring intermittently caused very intense suspension events lasting for at least several seconds accompanied by the fluctuations of the alongshore and vertical velocities. Moderate suspension events were also observed under uprushing bores with large fluctuating alongshore and vertical velocities. In summary, all the observed intermittent suspension events occurred with large fluctuating alongshore velocities. However, large alongshore velocities did not always result in sand suspension. These large alongshore velocities were about 20% of the cross-shore velocities and may be detectable even on natural beaches if the alongshore wave motions are absent.

The time-averaged sand fluxes on the equilibrium beach were calculated from the measured time series. The offshore sand flux due to the undertow was approximately balanced by the onshore sand flux due to the correlated time-varying components of the cross-shore velocity and sand concentration. The vertical sand fluxes were difficult to interpret because of the uncertainty of the measured vertical velocity which appeared to be an intermediate velocity between the fluid and sand velocities. It will be very difficult to predict the beach profile changes using the measured sand fluxes unless the velocity and concentration measurements are improved in their accuracy and extended to the free surface and bottom.

Chapter 3

NUMERICAL MODEL FOR SAND SUSPENSION IN SURF ZONES

3.1 Introduction

Linear time-averaged models [e.g., Battjes and Stive (1985)] based on the time-averaged momentum and energy equations have been applied successfully to predict the cross-shore variations of the wave setup and root-mean-square wave height in surf zones on beaches. Kobayashi and Johnson (1998) developed the nonlinear time-averaged model CSHORE based on the momentum, energy and continuity equations to predict the cross-shore variations of the wave setup, root-mean-square wave height and return current from outside the surf zone to the swash zone on natural beaches. The numerical model CSHORE was calibrated and compared with data from three laboratory tests on a 1:16 slope and two tests with equilibrium profiles [Johnson and Kobayashi (1998)]. CSHORE was verified using additional five tests on a 1:30 slope and field data collected at Duck, North Carolina [Johnson and Kobayashi (2000)]. Since CSHORE is relatively simple and efficient computationally, an attempt is made here to extend CSHORE to predict the cross-shore variations of the time-averaged sediment suspension rate, cross-shore sediment transport rate and bottom elevation change on the basis of the time-averaged, depth-integrated continuity equation for suspended sediment proposed by Kobayashi *et al.* (2000).

3.2 Time-Averaged Sediment Model

The time-averaged, depth-integrated continuity equation for suspended sediment in surf zones may be expressed as [Kobayashi *et al.* (2000)]

$$\frac{\partial q_s}{\partial x} = S - w_f\, C \quad , \qquad S = \frac{e_B\, D_B}{\rho g (s-1) h} \quad , \tag{3.1}$$

where x is the cross-shore coordinate taken to be positive onshore, q_s is the cross-shore sediment transport rate (positive onshore), S is the upward sediment suspension rate from the bottom per unit horizontal area, w_f is the sediment fall velocity, C is the depth-averaged volumetric sediment concentration, e_B is the suspension efficiency on the order of 0.01 for the turbulence induced by wave breaking, ρ is the fluid density, g is the gravitational acceleration, s is the specific gravity of the sediment and h is the mean water depth including wave setup. The overbar denoting time-averaging is omitted in (3.1) and q_s, S, C, D_B and h are the time-averaged quantities. The effect of the bottom friction on the suspension rate S may not be negligible in the swash zone but maybe neglected in the surf zone [Kobayashi and Johnson (2001)]. No measurement was made in the swash zone in this study.

The continuity equation of bottom sediment is expressed as [Kobayashi and Johnson (2001)]

$$(1 - n_p)\, \frac{\partial Z_b}{\partial t} = -\frac{\partial q_s}{\partial x} = w_f\, C - S \,, \tag{3.2}$$

where Z_b is the bottom elevation taken to be positive upward with $Z_b = 0$ at the still water level (SWL), t is the morphological time for the beach profile evolution and n_p is the porosity of the bottom sediment. The temporal rate of the bottom elevation change is normally related to the cross-shore gradient of the sediment transport rate in (3.2) but is expressed here as the difference between the sediment settling rate $w_f C$ and the sediment suspension rate S by use of (3.1).

To predict the temporal and cross-shore variations of Z_b using (3.2), it is necessary to estimate C and S as a function of t and x for the specified incident irregular waves and water level. The cross-shore variation of S at a given morphological time is estimated using the relationship in (3.1) where D_B and h are estimated using CSHORE for Z_b at this given time. This assumption is appropriate if the beach profile changes very little during the estimation of D_B, h and S. An additional relationship for C is required to obtain Z_b and q_s using (3.2). Kobayashi *et al.* (2000) expressed C in terms of S and S_e with S_e being the value of S for an equilibrium profile and obtained a semi-analytical solution for beach profile evolution. The analytical solution predicted both shoreline accretion and erosion but was not accurate enough to predict detailed features. An experiment was conducted in this study to examine the temporal and cross-shore variations of S and C.

3.3 Profile Evolution Tests

The profile evolution tests preceded the equilibrium profile tests in Chapter 2. The same experimental setup was used as in the equilibrium profile tests in Chapter 2. However, only the free surface elevations were measured. Velocities and sand concentration measurements were not made in this series of tests. Similar irregular waves were also used in both tests.

Figure 3.1 shows the beach profiles measured at time t = 0 (initial), 1, 7, 11.5, 18 and 50.5 hr where this time t is the duration of the wave action generated in bursts. Erosion occurred near the shoreline below SWL. The profile at t = 50.5 hr was quasi-equilibrium with the bottom profile changes less than 1 cm/hr. The horizontal distance in this figure and other figures in this section is the onshore distance from the entrance of the 115-cm wide flume in Figure 2.1.

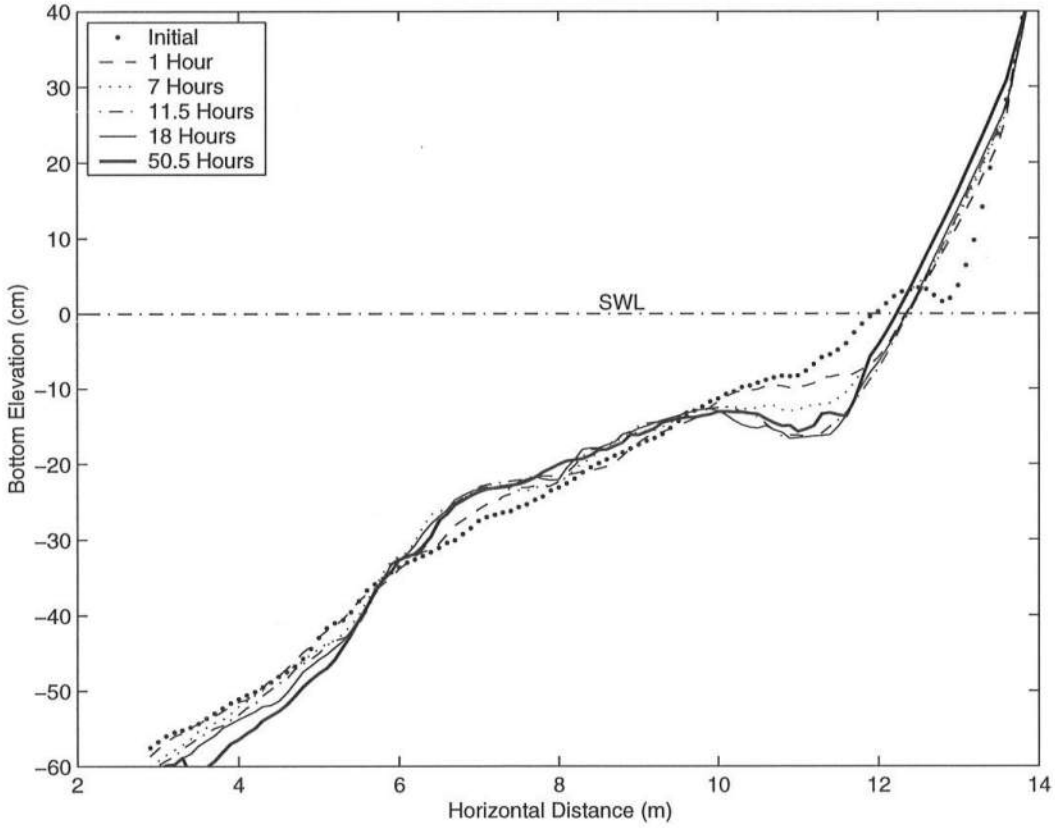

Figure 3.1: Measure Beach Profiles

Eight capacitance wave gauges as shown in Figure 2.1 were used to measure the free surface elevations at a sampling rate of 20 hz at eight cross-shore locations immediately after each of the six profile measurements. The eight gauges were moved somewhat as the profiles evolved. These six sets of the wave and profile data are simply called tests P1–P6 in this section. The free surface measurements were made in a single burst lasting for 900 s. The initial transitional waves of 60 s were removed from the measured time series. The free surface data at wave gauges 1-3 in Figure 2.1 were used to obtain the incident and reflected wave spectra. The spectral peak period, T_p, was approximately 4.8 s. The wave reflection coefficient, R, based on the zero-moments of the incident and reflected wave spectra increased from 0.24 for test P1 to 0.36 for test P6 with the increase of the foreshore slope caused by the erosion below SWL as shown in Figure 3.1. The mean $\overline{\eta}$, standard deviation, σ_η and skewness $skew$, of the free surface elevation η were also calculated for each time series of 840 s sampled at 20 Hz. The root-mean-square wave height H_{rms} is defined as $H_{rms} = \sqrt{8}\sigma_\eta$. Table 3.1 lists the still water depth d and the measured values of T_p, R, $\overline{\eta}$ and H_{rms} for the six tests conducted at the given time t. The wave conditions varied somewhat partly because of the profile evolution and partly because of the repair of the wave paddle during this experiment.

Table 3.1: Wave Statistics at Wave Gauge 1 for Six Tests

Test	t (hr)	d (cm)	T_p (s)	R	$\overline{\eta}$ (cm)	H_{rms} (cm)
P1	0	88.5	4.7	0.24	-0.3	12.4
P2	1	88.5	4.8	0.29	-0.2	13.9
P3	7	88.5	4.8	0.34	-0.1	14.2
P4	11.5	88.5	4.8	0.35	-0.1	14.2
P5	18	88.5	4.8	0.34	-0.3	12.8
P6	50.5	68.5	4.4	0.36	-0.2	12.2

To assess the accuracy of CSHORE in predicting the measured irregular wave transformation, comparisons were made of the measured and computed cross-shore variations of $\overline{\eta}$, H_{rms} and *skew* for each test. The values of T_p, $\overline{\eta}$ and H_{rms} at wave gauge 1 listed in Table 3.1 were specified as input to CSHORE. Figures 3.2 through 3.7 show the measured and computed cross-shore variations of $\overline{\eta}$, H_{rms} and *skew* for the six tests for the six profiles shown in Figure 3.1. These wave quantities vary noticeably due to the profile changes near the shoreline. The predicted wave height H_{rms} increased landward over the scour hole for tests P3–P6 but the predicted increase may not be realistic, although no data was obtained over the scour hole.

To improve the agreement in Figures 3.2 through 3.6 the empirical formulas adopted in CSHORE are calibrated as follows. The local fraction Q of breaking waves introduced by Battjes and Stive (1985) is used to separate the outer zone with $0 \leq Q < 1$ and the inner zone with $Q = 1$ for the beach profiles without any bar as shown in Figure 3.1. In the inner zone, CSHORE employs the empirical formula for the ratio $H_* = H_{rms}/h$ which increases landward. The empirical parameter γ_s specifies the value of H_* at the still water shoreline. Use is made of $\gamma_s = 1$ instead of $\gamma_s = 2$ to reduce the landward increase of H_{rms} near the shoreline. The nonlinear model CSHORE requires the skewness *skew* in the cross-shore radiation stress and wave energy flux. The empirical relationship between *skew* and H_* is expressed by three straight lines with $skew = 1$ at $H_* = 0.5$ which is reduced to $skew = 0.5$ at $H_* = 0.5$ in order to improve the agreement for the skewness in Figures 3.2 to 3.7.

CSHORE with the calibrated parameters is used to compute the cross-shore variation of the suspension rate S for each test using the relationship between S and D_B in (3.1) where the suspension efficiency is assumed to be given by $e_B = 0.01$ without any calibration. The suspension rate for the interval from test PJ to test P(J+1) with J = 1, 2, 3, 4 and 5 is estimated as the average suspension rate at the same cross-shore location computed for the two tests. This average suspension rate

S is compared with the left hand side of (3.2) expressing the rate of the sand volume deposited on the bottom of the unit horizontal area which is approximated by the finite difference involving the measured profiles Z_b for the two tests conducted at the known morphological time as listed in Table 3.1. Figure 3.8 shows the cross-shore variations of the average suspension rate and the net deposition (positive) or erosion (negative) rate for the five intervals of the six tests. Figure 3.8 indicates that the small difference between the relatively large $w_f C$ and S in (3.2) causes the bottom elevation change and the cross-shore gradient of the sediment transport rate q_s. However, the accuracy of the computed suspension rates is uncertain because the concentration C was not measured in these profile evolution tests.

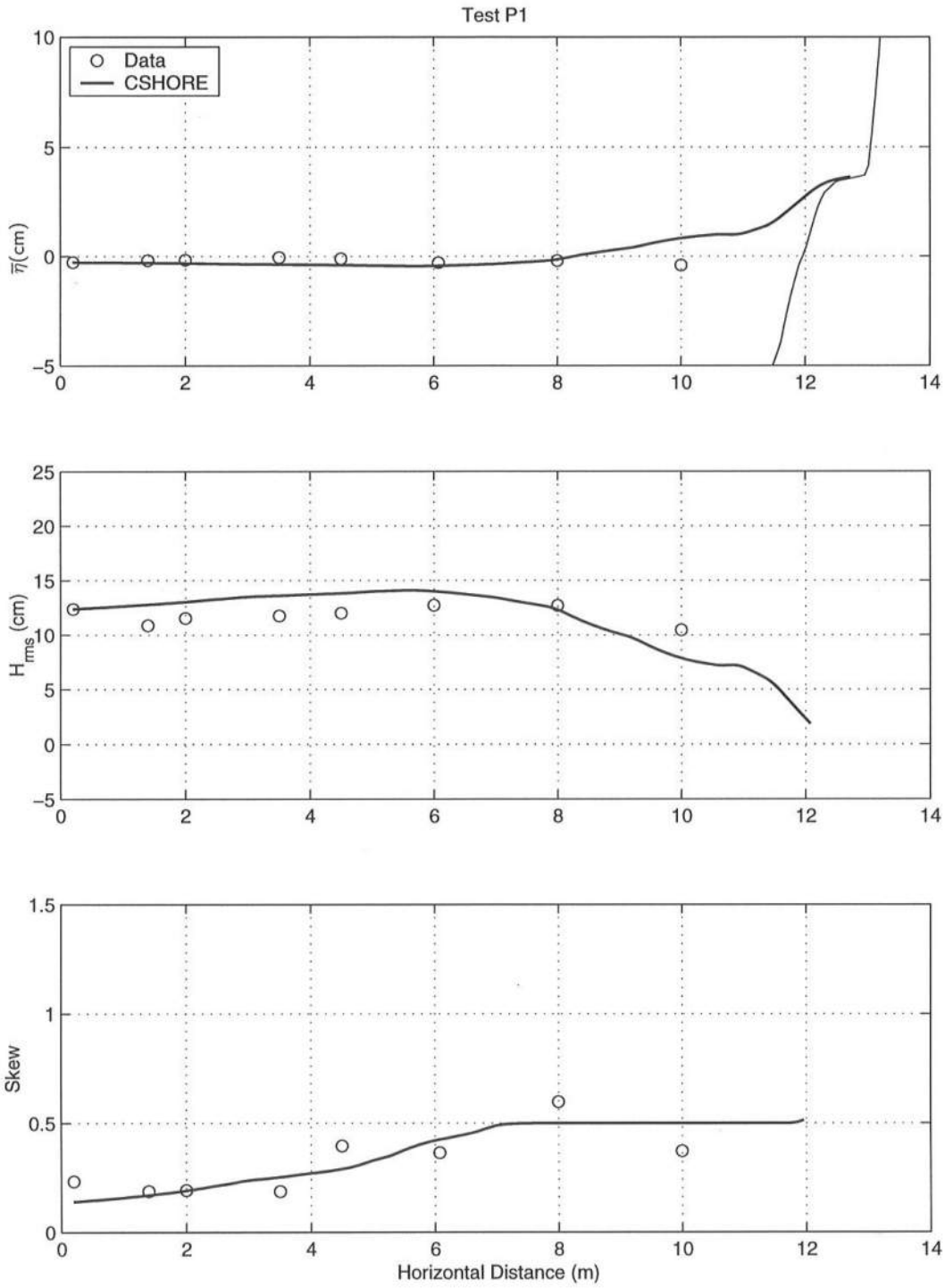

Figure 3.2: Measured and Computed $\overline{\eta}$, H_{rms}, and *skew* Test P1

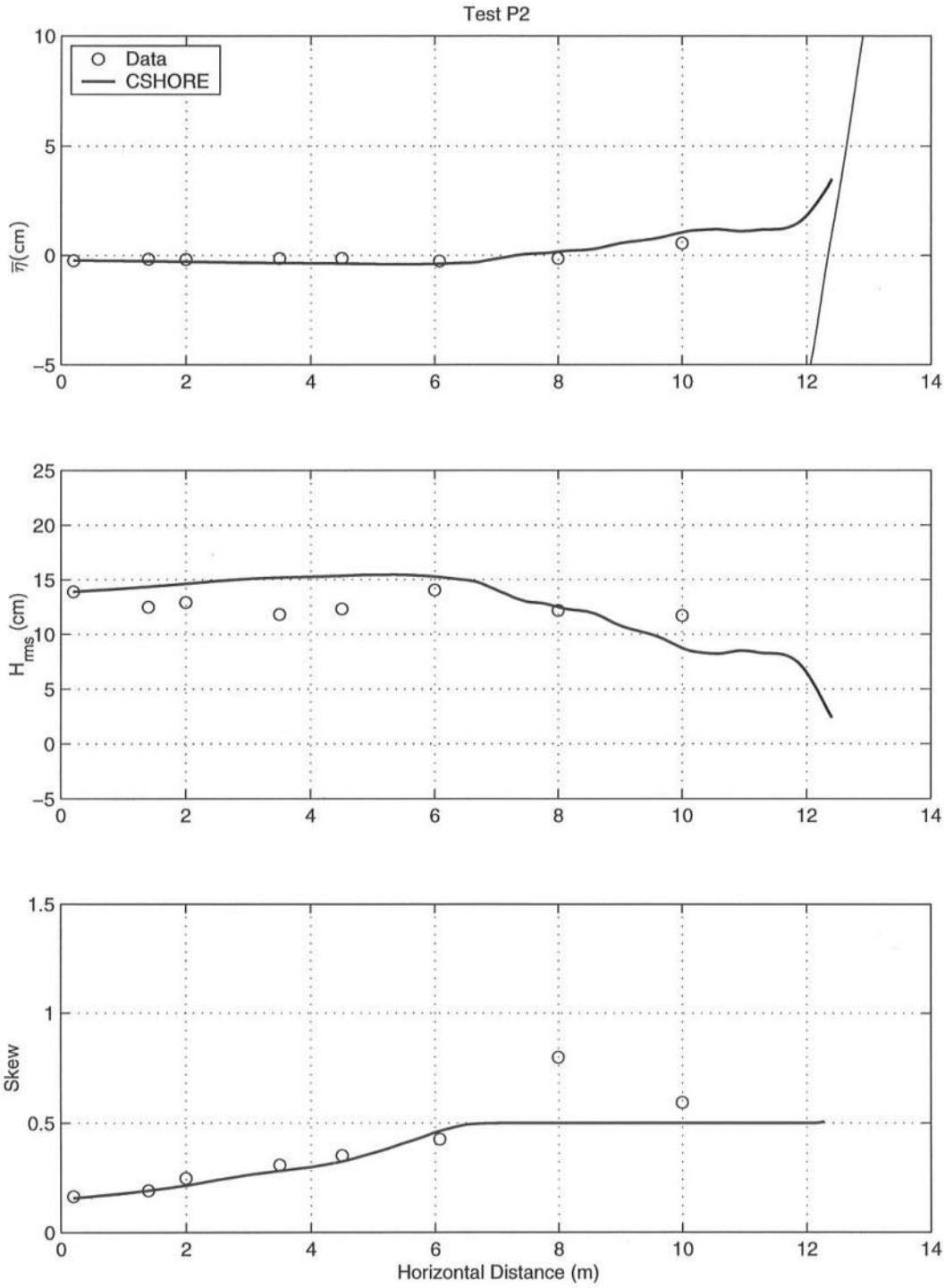

Figure 3.3: Measured and Computed $\overline{\eta}$, H_{rms}, and *skew* Test P2

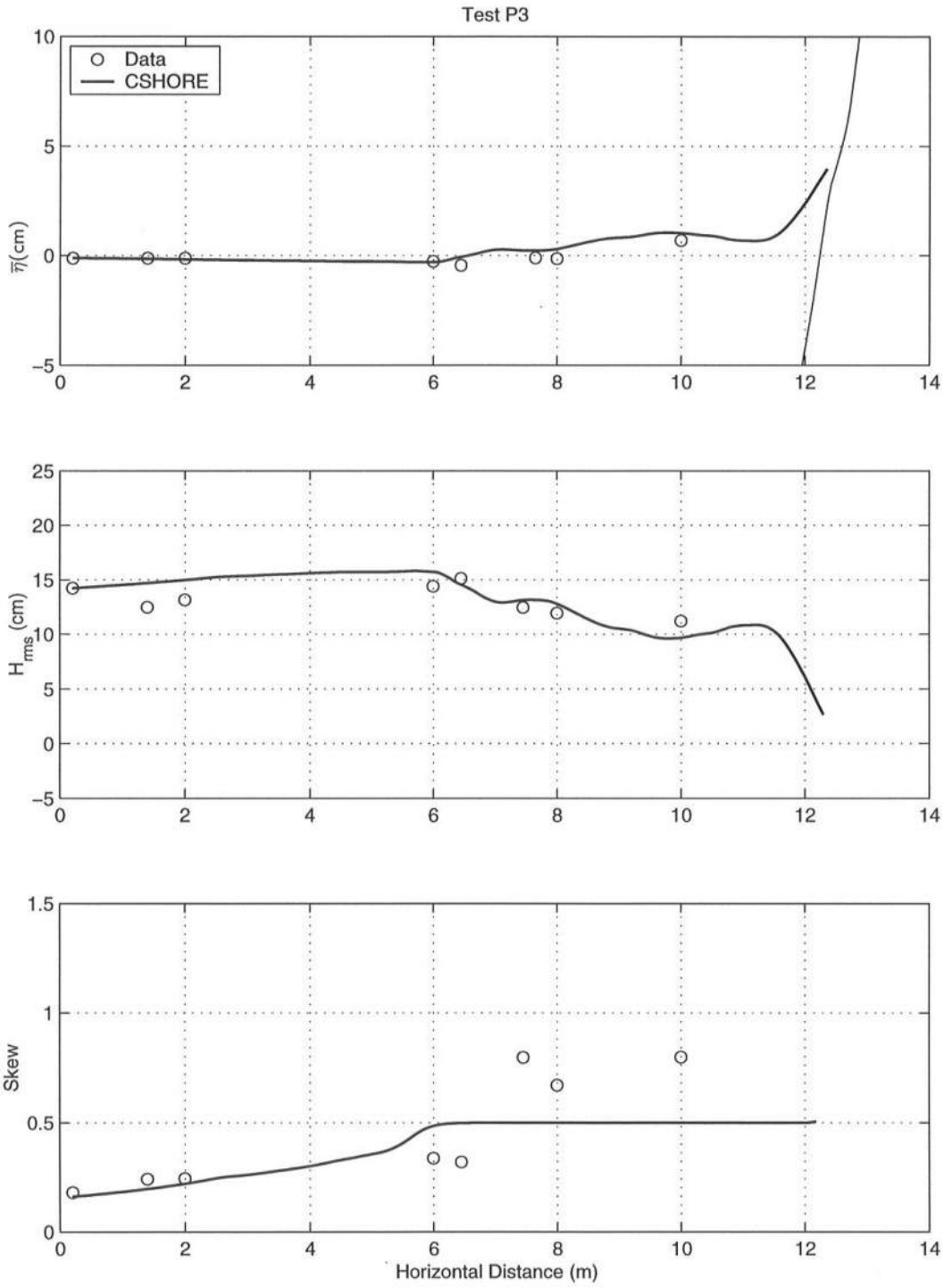

Figure 3.4: Measured and Computed $\overline{\eta}$, H_{rms}, and *skew* Test P3

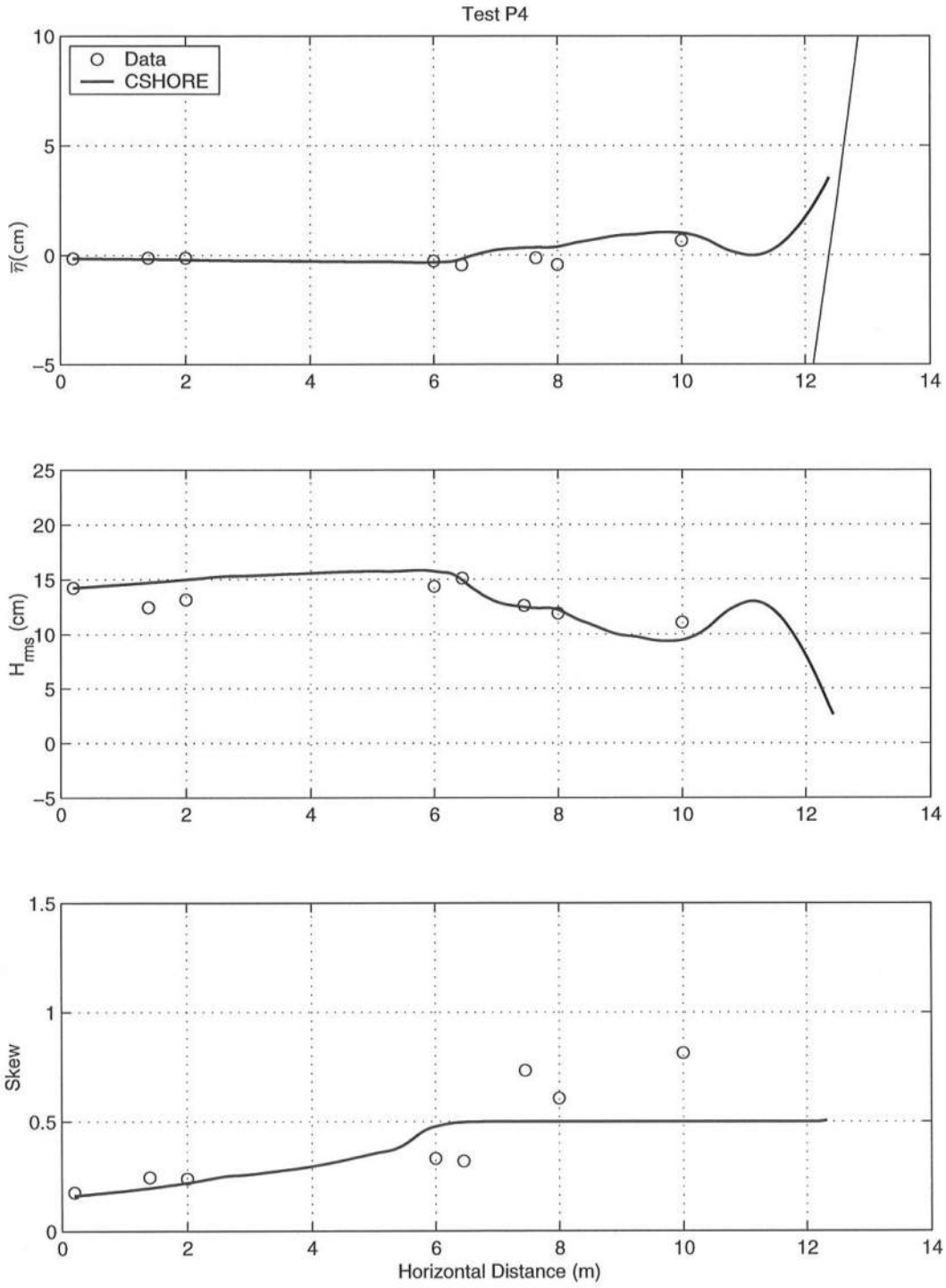

Figure 3.5: Measured and Computed $\overline{\eta}$, H_{rms}, and *skew* Test P4

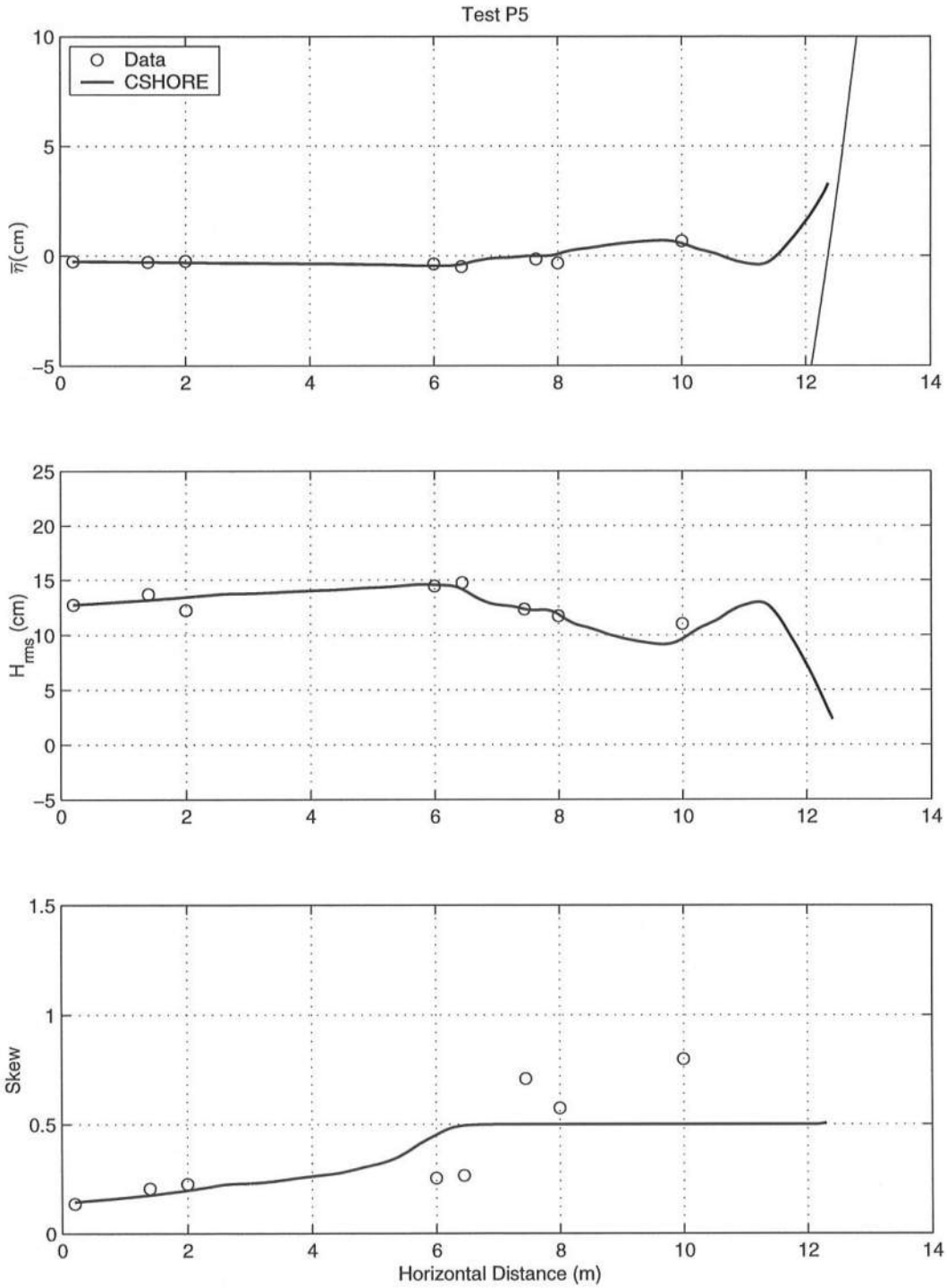

Figure 3.6: Measured and Computed $\overline{\eta}$, H_{rms}, and *skew* Test P5

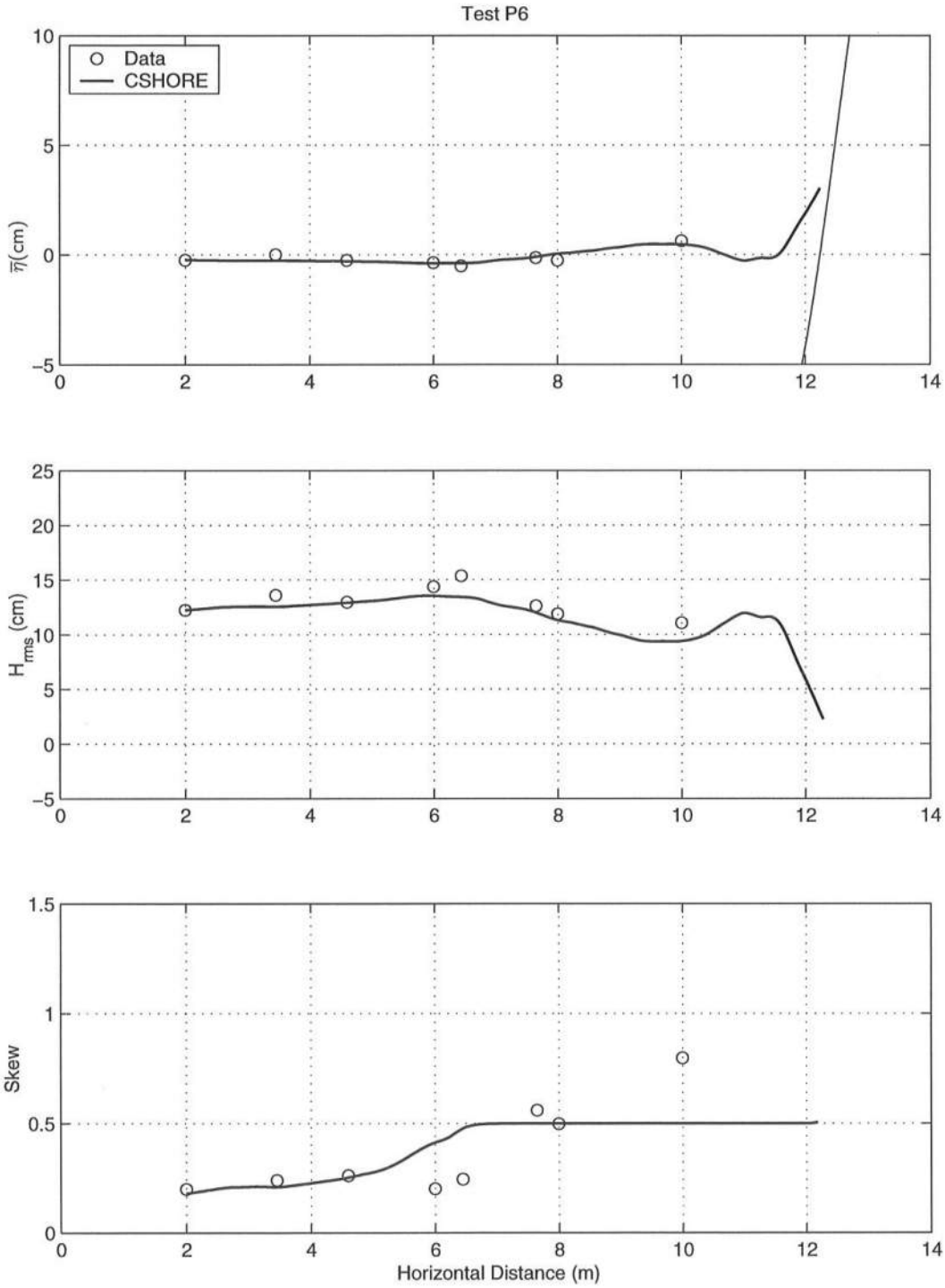

Figure 3.7: Measured and Computed $\overline{\eta}$, H_{rms}, and *skew* Test P6

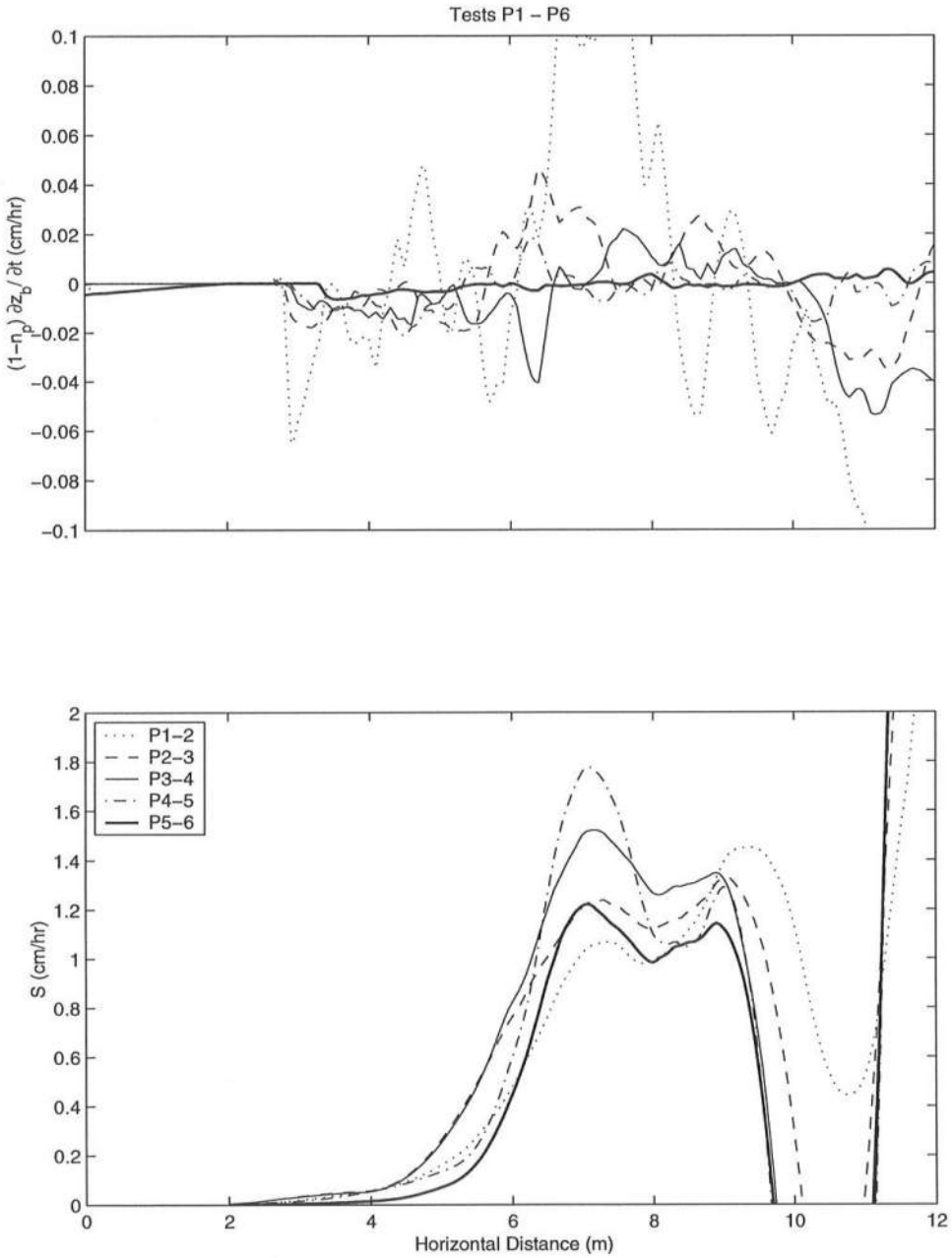

Figure 3.8: Cross-Shore Variations of Measured Net Rates and Computed Suspension Rates for Five Intervals of Six Tests

3.4 Equilibrium Profile Tests

CSHORE was used to predict the cross-shore variations of the wave setup, root-mean-square wave height and skewness for the equilibrium profile described in Chapter 2. The time-averaged, depth-integrated cross-shore velocity $\overline{u}$ and standard deviation σ_u were also estimated using CSHORE coupled with relationships derived from linear progressive long-wave theory. The concentration C was also predicted using CSHORE in conjunction with (3.1) and (3.2). The values predicted by CSHORE are then compared with the experimental values reported in Chapter 2.

Figure 3.9 shows the measured and computed cross-shore variations of $\overline{\eta}$, H_{rms} and *skew* of η where x is the onshore distance from wave gauge 1 located in the still water depth d = 80 cm. The input to CSHORE is the measured values of $\overline{\eta}$ = -0.1 cm, H_{rms} = 11.5 cm and T_p = 4.8 s at wave gauge 1. The time series of the free surface elevation η at each of the eight wave gauges were repeatable within approximately 1% differences for the 37 tests. The spectral peak period T_p = 4.8 s remained the same except that the secondary peak in the low frequency range became as large as the spectral peak at T_p = 4.8 s at gauge E. The mean $\overline{\eta}$ decreased to -0.5 cm (wave set-down) at gauge B (x = 6.05 m) and increased to 0.8 cm (wave setup) at gauge E (x = 9.30 m). The root-mean-square wave height H_{rms} increased to 13.1 cm at gauge A (x = 4.35 m), decreased to 10.6 cm at gauge C (x = 7.40 m), and increased slightly at gauge D (x = 8.30 m) before the decrease at gauge E. The incident irregular waves did not break at gauge A, were breaking frequently at gauge B, broke intensely sometimes at gauges C and D, and became bores at gauge E. Gauge D was at the transition from breaking waves to bores. On the other hand, the skewness *skew* of η increased landward except for the decrease at x = 7.40 m. CSHORE predicts the cross-shore variations of these wave statistics fairly well without any additional calibration.

The cross-shore velocities u measured by the two velocimeters varied very

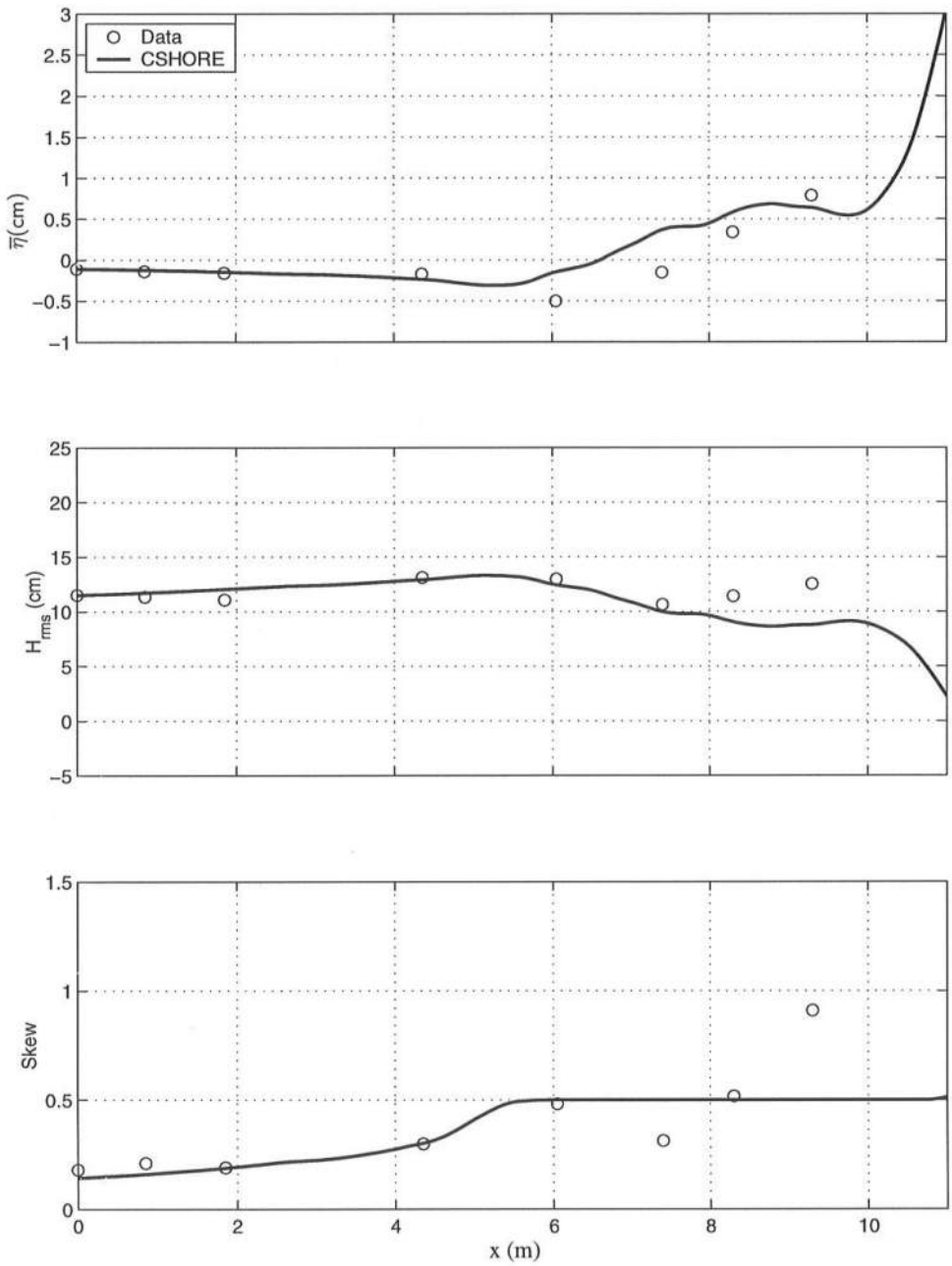

Figure 3.9: Measured and Computed $\overline{\eta}$, H_{rms} and *skew* for Equilibrium Profile Tests

little vertically at lines A–E in Figure 2.2. The waves landward of line A were essentially in shallow water. The ratio between the linear wavelength L_p based on T_p = 4.8 s and the mean water depth $h = (d+\overline{\eta})$ was 23 at line A where d = 43.1 cm and h = 42.9 cm at line A. The mean $\overline{u}$ and the standard deviation σ_u of u measured by the two velocimeters at the different elevations are averaged vertically to obtain the averaged values of $\overline{u}$ and σ_u at lines A–E. These values are plotted as a function of x in Figure 3.10. The cross-shore velocity u is taken to be positive landward and the negative mean current $\overline{u}$ is undertow. The undertow was approximately -7 cm/s at lines C and D where intense wave breaking occurred. The standard deviation σ_u related to the magnitude of the time-varying velocity components increased landward outside the surf zone and was approximately constant at lines B–E inside the surf zone. The computed cross-shore variations of $\overline{u}$ and σ_u are based on the following relationships derived from linear progressive long-wave theory [Kobayashi *et al.* (1998)]:

$$\overline{u} = -(gh)^{0.5}\left(\frac{\sigma_\eta}{h}\right)^2 , \qquad \sigma_u = \left(\frac{g}{h}\right)^{0.5} \sigma_\eta , \tag{3.3}$$

where $h = (d+\overline{\eta})$ and $\sigma_\eta = H_{rms}/\sqrt{8}$ are based on the computed $\overline{\eta}$ and H_{rms} shown in Figure 3.9. CSHORE with (3.3) predicts the measured cross-shore variations of $\overline{u}$ and σ_u well although (3.3) does not account for the additional water volume flux due to rollers.

The sand concentrations measured by the two sensors are expressed in terms of the sand mass in grams divided by the mixture volume in liters. The measured concentrations exhibited intermittent temporal variations in which the instantaneous concentration was intermittently much larger than the mean concentration. The intermittent suspension events are reported in Chapter 2 and the following analysis is limited to the mean concentration. The mean concentration decreased upward rapidly at line A outside the surf zone and slowly at lines B–E inside the surf zone. Three-dimensional ripples were present in the vicinity and seaward of line A

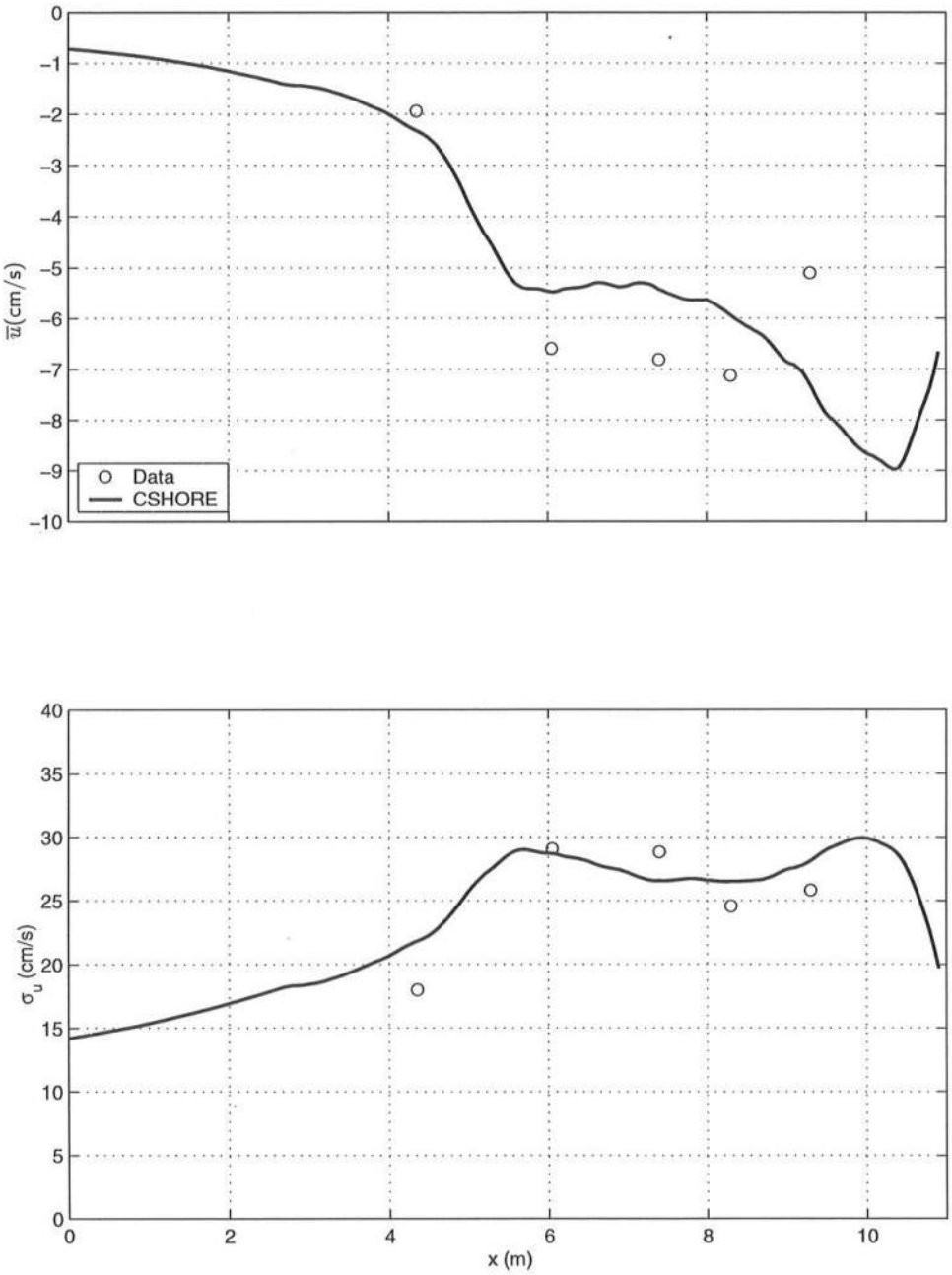

Figure 3.10: Measured and Computed $\overline{u}$ and σ_u for Equilibrium Profile Tests

in Figure 2.2. The height and cross-shore wavelength of these ripples were approximately 2 cm and 11 cm, respectively. The ripples became more two-dimensional and their heights decreased landward. No ripples were visible landward of line B. At line A, the mean concentration was about 3 g/L in the region affected by vortices ejected from the ripples, less than 1 g/L at 4 cm from the bottom and 0.2 g/L at 20 cm from the bottom. At lines B–E, the mean concentration decreased less than 40% from 1 cm to n cm above the bottom where $n = 7$, 4, 3 and 3 at lines B, C, D and E.

The mean concentrations measured by the two sensors at the different elevations above the bottom are averaged vertically to obtain the average mean concentration C at lines A–E. This concentration C is plotted as a function of x in Figure 3.11. The cross-shore variation of C is consistent with the visually observed intensity of wave breaking which was the maximum at line C and reduced noticeably under bores at line E. The measured average concentration C is not the same as the depth-averaged concentration C used in (3.1) and (3.2) because no concentration measurements were made in the large area near the free surface as shown in Figure 2.2 and the sheet-flow layer of high sand concentrations on the bed. Nevertheless, these concentrations are compared in Figure 3.11. The computed concentration C is based on $C = S/w_f$ obtained from (3.2) for the equilibrium profile with $\partial Z_b/\partial t = 0$ where the corresponding suspension rate S is computed using CSHORE for the equilibrium profile. The computed volumetric concentration is converted to the concentration in grams per liter where the density of the sand was 2.6 g/cm.^{3} The measured cross-shore variation of the sand concentration is predicted at least qualitatively by the linear relationship between S and D_B/h in (3.1) with D_B and h computed by CSHORE. This indicates that the suspended sand concentration is closely related to the wave energy dissipation rate per unit volume of water due to wave breaking as discussed by Kobayashi *et al.* (2000).

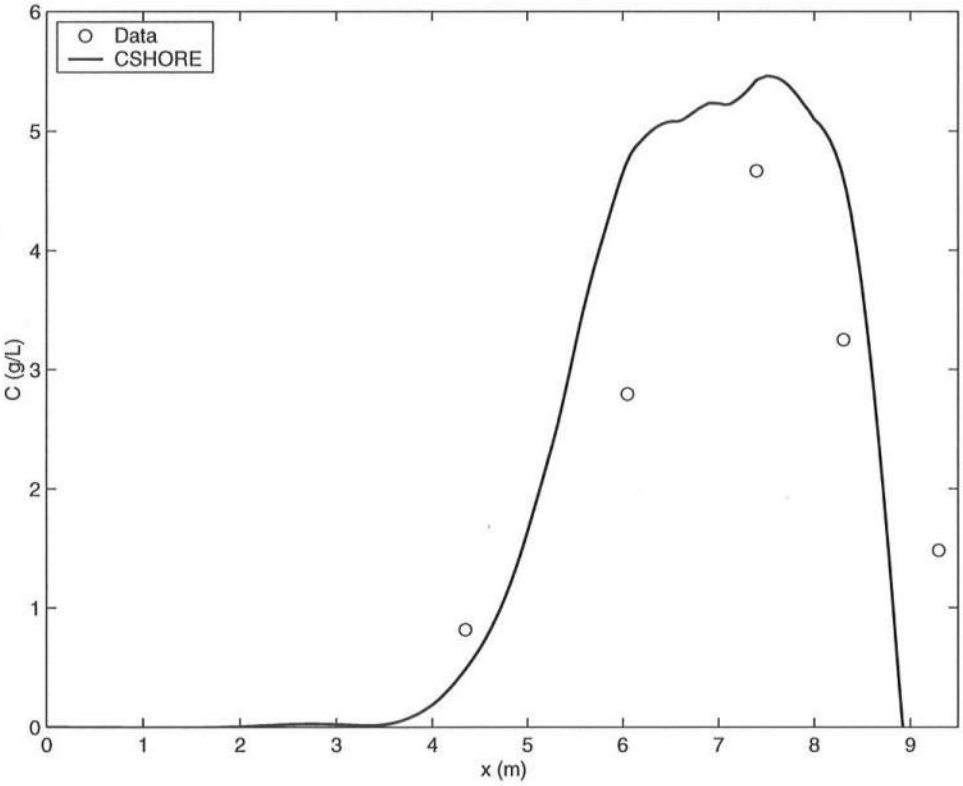

Figure 3.11: Measured and Computed Sand Concentrations above Equilibrium Profile

3.5 Conclusions

The time-averaged, depth-integrated model for suspended sediment proposed by Kobayashi *et al.* (2000) is combined with the nonlinear time-averaged wave model CSHORE developed by Kobayashi and Johnson (1998). In this relatively simple sediment model, the temporal change of the bottom elevation change is expressed as the difference between the sediment suspension and settling rates where the suspension rate is proportional to the wave energy dissipation rate per unit volume of water. Profile evolution tests were conducted to estimate the sediment suspension rates in comparison to the rates of bottom elevation change. CSHORE is calibrated using the measured cross-shore variations of the waves statistics. The sediment suspension rates are found to be much larger than the rates of bottom elevation change. As a result, it will be necessary to accurately predict the relatively small difference of the sediment suspension and settling rates in order to predict the beach profile evolution accurately.

Furthermore, equilibrium profile tests were conducted to verify the calibrated CSHORE and assess the capability of the sediment model in predicting the cross-shore variation of the suspended sediment concentration. The measured cross-shore variations of the wave statistics are predicted fairly well by CSHORE without any additional calibrations. CSHORE combined with the simple relationships based on linear long-wave theory is also shown to predict the cross-shore variations of the mean and standard deviation of the measured cross-shore velocity. The cross-shore variation of the measured suspended sediment concentration above the equilibrium profile can be explained, at least qualitatively, by the sediment model combined with CSHORE probably because of the importance of the sediment suspension in the surf zone. However, an additional relationship for C is still required to predict the beach profile evolution using (3.1) and (3.2). Future efforts are needed to solve this closure problem.

Chapter 4

GENERAL CONCLUSIONS

Two irregular wave experiments were conducted on a fine sand beach in a wave flume. An evolving profile experiment was conducted to calibrate the time-averaged irregular wave model CSHORE. Then an equilibrium profile test was conducted to observe and measure sediment suspension events in the nearshore environment and to asses the model's capabilities of predicting the cross-shore variations of sediment suspension rate, cross-shore sediment transport rate and bottom elevation change.

In Chapter 3 the nonlinear time-averaged wave model CSHORE was coupled with a time-averaged, depth-integrated model for suspended sediment. In this relatively simple sediment model, the temporal rate of change of the bottom elevation is assumed to be equal to the difference between the sediment suspension rate and the settling rate where the suspension rate is proportional to the wave energy dissipation rate per unit volume of water. Profile evolution tests were conducted to calibrate the wave model and to estimate sediment suspension rates in comparison to the rates of bottom elevation change. The sediment suspension rates were found to be much larger than the rates of bottom elevation change. Thus, it will be necessary to accurately predict the relatively small difference between the sediment suspension and settling rates in order to predict the beach profile evolution accurately.

In the equilibrium profile test described in Chapter 2, sand suspension events were examined under shoaling waves on a rippled bed and under breaking waves and

bores on an equilibrium terraced beach consisting of fine sand. The measured sand suspension events were found to be repeatable and non-random. The measured free surface elevations and cross-shore velocities were found to be dominated by irregular wave motions and did not allow the easy detection of vortices and turbulence that cause sand suspension events. The measured vertical velocity exhibited both wave and turbulent motions that were difficult to separate. The measured alongshore horizontal velocities were used to estimate the intensity and duration of the three-dimensional vortices and turbulence associated with wave breaking. The observed suspension mechanisms included sand suspension from the rippled bed under large shoaling waves in a wave group, intense suspension events under strong plunging breakers that occurred intermittently and moderate suspension events under bores. The sand suspension events tended to occur during the intervals of large alongshore velocity fluctuations. Also, the spectra of the measured alongshore velocities and concentrations were all dominated by low frequency components.

The time-averaged sand fluxes were also examined in Chapter 2. The offshore flux due to the undertow was approximately balanced by the onshore sand flux due to the correlated time-varying components of the cross-shore velocity and sand concentration. However, the vertical sand fluxes were difficult to interpret because of the uncertainty of the measurements of the vertical velocity which seemed to be an intermediate velocity between the fluid and sand velocities. Therefore, the accuracy of the velocity and concentration measurements will need to be improved and extended to the free surface and bottom in order to accurately predict beach profile changes.

The results of the equilibrium profile test described in Chapter 2 were also used to verify the calibrated CSHORE and to assess the capability of the sediment model in predicting the cross-shore variation of the suspended sediment concentration. CSHORE predicted the cross-shore variations of the wave statistics fairly

well without additional calibrations. The cross-shore variations of the mean and standard deviation of the cross-shore velocity were also predicted by combining CSHORE with simple relationships based on linear long-wave theory. The sediment model combined with CSHORE could qualitatively predict the cross-shore variation of the suspended sediment concentration above the equilibrium profile. However, in order to predict beach profile evolution an additional relationship for C will need to be developed. Thus, futures efforts are needed to solve this closure problem experimentally and analytically.

Bibliography

Battjes, J. A. and Stive, M. J. F. (1985). Calibration and verification of a dissipation model for random breaking waves. *J. Geophys. Res.*, **90**, 9159–9167.

Beach, R. A. and Sternberg, R. W. (1988). Suspended sediment transport in the surf zone: Response to cross-shore infragravity motion. *Mar. Geol.*, **80**, 61–79.

Beach, R. A. and Sternberg, R. W. (1992). Suspended sediment transport in the surf zone: Response to incident wave and longshore current interaction. *Mar. Geol.*, **103**, 513–520.

Conley, D. C. and Inman, D. L. (1992). Field observations of the fluid-granular boundary layer under near-breaking waves. *J. Geophys. Res.*, **97**, 9631–9643.

Cox, D. T. and Kobayashi, N. (2000). Identification of intense, intermittent coherent motions under shoaling and breaking waves. *J. Geophys. Res.*, **105**(C6), 14223–14236.

Crawford, A. M. and Hay, A. E. (2001). Linear transition ripple migration and wave orbital velocity skewness: Observations. *J. Geophys. Res.*, **106**, 14113–14128.

Dean, R. G. and Dalrymple, R. A. (1984). *Water Wave Mechanics for Engineers and Scientists*. Prentice-Hall, Englewoods Cliffs, New Jersey. 353 pp.

Downing, J. P., Sternberg, R. W., and Lister, C. R. B. (1981). New instrumentation for the investigation of sediment suspension processes in the shallow marine environment. *Mar. Geol.*, **42**, 19–34.

Foster, D. L., Bowen, A. J., Beach, R. A., and Holland, R. A. (1996). A comparison of field observations and quasi-steady linear shear instabilities of the wave bottom boundary layer. paper presented at *25th Coastal Engineering Conference*. Orlando, Fla.

Gallagher, E. L., Elgar, S., and Guza, R. T. (1998). Observations of sand bar evolution on a natural beach. *J. Geophys. Res.*, **103**, 3203–3215.

Giovannozzi, M. A., Kobayashi, N., and Johnson, B. D. (2001). Wave breaking and sediment suspension in surf zones. paper presented at *Waves 2001 Conference*. San Francisco, CA.

Grasmeijer, B. T. and van Rijn, L. C. (1999). Transport of fine sands by currents and waves.III: Breaking waves over barred profile with ripples. *J. Waterw. Port Coastal Ocean Eng.*, **125**, 71–79.

Guza, R. T. and Thornton, E. B. (1980). Local and shoaled comparisons of sea surface elevations, pressures, and velocities. *J. Geophys. Res.*, **85**, 1524–1530.

Hanes, D. M. (1991). Suspension of sand due to wave groups. *J. Geophys. Res.*, **96**, 891–895.

Hanes, D. M. and Huntley, D. A. (1986). Continuous measurements of suspended sand concentration in a wave dominated nearshore environment. *Cont. Shelf Res.*, **6**, 585–596.

Hay, A. E. and Bowen, A. J. (1994). Coherence scales of wave-induced suspended sand concentration fluctuations. *J. Geophys. Res.*, **99**, 12749–12765.

Jaffe, B. E. and Rubin, D. M. (1996). Using nonlinear forcasting to learn the magnitude and phasing of time-varying sediment suspension in the surf zone. *J. Geophys. Res.*, **101**, 14282–14296.

Jaffe, B. E. and Sallenger, A. H. (1992). The contribution of suspension events to sediment transport in the surf zone. *paper presented at 23rd Coastal Engineering Conference*. Venice, Italy.

Johnson, B. D. and Kobayashi, N. (1998). Nonlinear time-averaged model in surf and swash zones. paper presented at *26th Coastal Engineering Conference*. Copenhagen, Denmark.

Johnson, B. D. and Kobayashi, N. (2000). Free surface statistics and probablities in surf zones on beaches. paper presented at *27th Coastal Engineering Conference*. Sydney, Australia.

Kobayashi, N. and Johnson, B. D. (1998). Computer program CSHORE for predicting cross-shore transformation of irregular breaking waves. *Res. Rep.*, **CACR-98-04**. Ctr. Appl. Coast. Res., Univ. of Del., Newark.

Kobayashi, N. and Johnson, B. D. (2001). Sand supension, storage, advection, and settling in surf and swash zones. *J. Geophys. Res.*, **106**, 9363–9376.

Kobayashi, N. and Seo, S. N. (1985). Fluid and sediment interaction over a plane bed. *J. Hydraul. Eng.*, **111**, 903–921.

Kobayashi, N., Herrman, M. N., Johnson, B. D., and Orzech, M. D. (1998). Probability distribution of surface elevation in surf and swash zones. *J. Waterw. Port Coastal Ocean Eng.*, **124**, 99–107.

Kobayashi, N., Karjadi, E. A., and Johnson, B. D. (2000). Cross-shore sand transport on beaches. paper presented at *27th Coastal Engineering Conference*. Sydney, Australia.

Kobayashi, N., Giovannozzi, M. A., and Johnson, B. D. (2001). Intermittent intense sand suspension events under irregular shoaling and breaking waves. paper submitted to *J. Geophys. Res.*.

McLean, S. R., Ribberink, J. S., Dohmen-Janssen, C. M., and Hassen, W. N. (2001). Sand transport in oscillatory sheet flow with mean current. *J. Waterw. Port Coastal Ocean Eng.*, **127**, 141–151.

Nadaoka, K., Ueno, S., and Igarashi, T. (1988). Sediment suspension due to large scale eddies in the surf zone. paper presented at *21st Coastal Engineering Conference*. Malaga, Spain.

Orzech, M. D. and Kobayashi, N. (1998). Equilibrium terraced and barred beaches. paper presented *at 26th Coastal Engineering Conference*. Copenhagen, Denmark.

Puleo, J. A., Beach, R. A., Holman, R. A., and Allen, J. S. (2000). Swash zone sediment suspension and transport and the importance of bore-generated turbulence. *J. Geophys. Res.*, **105**, 17021–17044.

Ribberink, J. S. and Al-Salem, A. A. (1994). Sediment transport in oscillatory boundary layers in cases of rippled beds and sheet flow. *J. Geophys. Res.*, **99**, 12707–12727.

Thornton, E. B., Humiston, R. T., and Birkemeier, W. (1996). Bar/trough generation on a natural beach. *J. Geophys. Res.*, **101**, 12097–12110.

Zhang, D. P. and Sunamura, T. (1994). Multiple bar formation by breaker-induced vortices: A laboratory approach. paper presented at *24th Coastal Engineering Conference*. Kobe, Japan.